Martin Schnedlitz, BSc

A study of thermally induced surface diffusion processes of monometallic nanowires

MASTER THESIS

For obtaining the academic degree
Diplomingenieur

Master Programme of
Technical Physics

Graz University of Technology

Supervisor:
Univ.-Prof. Mag. Dr.rer.nat Wolfgang E. Ernst
Institute of Experimental Physics

Graz, 2017

blank

Deutsche Fassung:
Beschluss der Curricula-Kommission für Bachelor-, Master- und Diplomstudien vom 10.11.2008
Genehmigung des Senates am 1.12.2008

EIDESSTATTLICHE ERKLÄRUNG

Ich erkläre an Eides statt, dass ich die vorliegende Arbeit selbstständig verfasst, andere als die angegebenen Quellen/Hilfsmittel nicht benutzt, und die den benutzten Quellen wörtlich und inhaltlich entnommenen Stellen als solche kenntlich gemacht habe.

Graz, am ……. ……..
(Unterschrift)

Englische Fassung:

STATUTORY DECLARATION

I declare that I have authored this thesis independently, that I have not used other than the declared sources / resources, and that I have explicitly marked all material which has been quoted either literally or by content from the used sources.

……. ……..
date (signature)

Abstract

Nanoparticles span the gap between atoms and bulk materials and are therefore an interesting and challenging field of research as their properties differ significantly from the corresponding bulk properties. Especially wire-shaped nanostructures have potential usages in a large variety of fields, such as catalysis, optic or nanoeletronics. One goal of investigating the properties of nanostructures is to replace expensive materials such as palladium with cheaper ones like copper. As a consequence the characterisation and investigation of thermally induced surface diffusion processes and the mobility on substrates are of major interest.

A new and novel approach to the synthesis of nanoparticles is the helium droplet technique. This method uses superfluid helium droplets, which are used as completely inert and interactionless environments for the synthesis of nanoparticles.

Within this thesis the surface diffusion and the corresponding thermal stability of metallic nanowires is investigated. A large variety of metals such as palladium, gold, copper, etc. is studied in order to make general statements about structure and stability. The thesis can be divided into three major parts: The synthesis of nanowires with the helium droplet technique, the analysis of thermally induced surface diffusion processes by using of a FEI Titan transmission electron microscope, and the prediction of the observed processes via a new algorithm, based on a cellular automaton. It is important to mention that as a result of the high resolution of the FEI Titan *in-situ* observations of surface diffusion processes of metallic nanowires were made for the first time.

Kurzfassung

Nanopartikel bilden die Brücke zwischen Atomen und Festkörpern und sind dahingehend ein spannendes und herausforderndes Forschungsgebiet, da sich ihre Eigenschaften deutlich von jenen des Festkörpers unterscheiden. Insbesondere elongierte/drahtförmige Nanostrukturen haben ein großes Potential in diversen Forschungsgebieten wie der Katalyse, Optik oder der Nanoelektronik. Ziel der Untersuchung der Eigenschaften von Nanostrukturen ist mitunter auch, teurere Materialen wie Palladium durch deutlich günstigere Materialien wie Kupfer zu ersetzen. Dahingehend sind elementspezifische Untersuchungen der thermischen Stabilität, der Mobilität auf Substraten und der katalytischen Eigenschaften von besonders großem Interesse.

Ein neuartiger und innovativer Ansatz zur Erstellung von Nanopartikeln stellt die Heliumtropfentechnik dar. Diese Methode nutzt superfluide Heliumtröpfchen, welche als hochreine und interaktionsfreie Träger des Syntheseprozesses von Nanopartikeln dienen.

Im Zuge dieser Arbeit wird die Oberflächendiffusion und die damit einhergehende Stabilität von metallischen Nanodrähten untersucht. Eine besonders große Auswahl an Metallen wie Palladium, Gold, Kupfer, etc. wurde untersucht um allgemeine Aussagen über Struktur und Stabilität treffen zu können. Die Arbeit gliedert sich im Wesentlichen in drei Bereiche: Der Erstellung von Nanowires mithilfe der Heliumtropfen Technik, der Analyse der thermisch induzierten Oberflächendiffusion mithilfe eines FEI Titan Transmission Elektronen Mikroskop und der Vorhersage dieser Prozesse durch einen, während dieser Arbeit entstandenen, zellulären Automaten. Dazu sei zu erwähnen, dass aufgrund des besonders leistungsstarken hochauflösenden Elektronen Mikroskop FEI Titan allererste in-situ Beobachtungen von Diffusionsprozessen von metallischen Nanodrähten beobachten werden konnten.

Articles Related to this Work

1. Martin Schnedlitz, Maximilian Lasserus, Daniel Knez, Andreas W. Hauser, Ferdinand Hofer and Wolfgang E. Ernst. Thermally induced breakup of metallic nanowires: Experiment and theory. *Phys. Chem. Chem. Phys.*, 2017.

2. Andreas W. Hauser, Martin Schnedlitz, and Wolfgang E. Ernst. A coarse grain Monte Carlo approach to diffusion processes in metallic nanoparticles. *EPJ*, accepted.

Contents

List of Figures

Chapter 1

Introduction

Over million years, nature has improved and perfected biological devices at the nanoscale, for example DNA strands. Mankind have utilized the unique properties of nano particles for centuries, i.e. ancient Romans have used gold nanoparticles to create glittering effects on vases. However, only within the last few decades and years scientists have started to investigate and understand these unique properties. The ongoing interest can be measured by the amount of publications with nano-prefixed terms in their title. In fact, the amount of papers related to nano technology has more than quadrupled during the last twenty years[8].

Nanoparticles, especially wire-shaped nanostructures have attracted recent attention due to their potential usage in circuits and nanodevices[28, 54], biosensors[1, 7, 69], waveguides[73], membranes[33], transparent electrodes[49] or antennae for photochemistry applications[52]. For diameters in the range of a few nanometres a whole series of unusual properties emerges: Ferromagnetism[74], negative magnetoresistance[3] or quantum conductance have been reported[11], making smallest nanowires potential components particularly interesting for miniature electronic circuits.[39]

The first studies related to this work have been carried out by the Ernst group, starting with the Rayleigh breakup of Ag nanowires[65], exploiting superfluid He nanodroplets (He_N) as nanolabs for the production of one-dimensional metallic structures[37, 56]. The dotation of He_N with particles is well established in spectroscopy[6, 59, 60], and has recently been adapted for the controlled production and structure preserving soft deposition of metal clusters[9, 40, 43, 57, 67]. For the creation of metallic nanowires we take advantage of a vortex formation, a quantum effect[14, 47] occurring for larger droplets with diameters of a few μm. As was originally observed in bulk superfluid helium (He II)[4, 70, 72], these vortices attract dopants immersed in the helium due to a pressure gradient around the vortex core, causing a preference for one-dimensional growth, which leads to the formation of nanowires.

The experimentally challenging technique offers the benefit of complete inertness during wire production, deposition and measurement. Typically, nanowires in the sub 10 nm diameter range are stabilized by templates[12, 25, 41], which introduce a large bias in stability measurements.

This thesis aims to deepen the understanding of thermally induced surface diffusion processes with regard to material-specific constants. In order to do this, a combined approach involving theory and experiment is performed.

Chapter 2

Theoretical Background

In this first section, the basic concepts and the theoretical background of cluster synthesis inside a liquid helium droplet environment is presented. This chapter describes the physical concepts behind clusters and why a liquid helium droplet with a temperature of ~ 0.4 K provides an ideal and unique environment for the formation process of clusters.

2.1 Clusters

Clusters have attracted recent attention due to their potential usage in numerous fields (i.e. circuits and nanodevices [28, 54]), because they fill the gap between single atoms or molecules and bulk material. A cluster is per definition a package of atoms or molecules with a number of 3 to $\approx 10^5$ atoms. For diameters in the range of a few nanometers a whole series of unusual properties emerges: Ferromagnetism[74], negative magnetoresistance[3] or quantum conductance have been reported[11], making smallest nanowires potential components particularly interesting for miniature electronic circuits[39].

Their properties show unusual behaviour, as surface size effects become present in this regime. A possible classification of clusters can be taken as

- Small clusters: 3 to 12 atoms. The concepts of atomic- and molecular physics are still valid for low enough temperatures and all atoms are located on the surface of the cluster.
- Medium clusters: 12 to 10^2 atoms. Molecular concepts are no longer capable of predicting the properties. Rapid changes in properties occur with increasing cluster size.
- Large clusters: 10^2 to 10^3 atoms. A gradual change from atomic properties to solid properties occur, e.g. the change of the lattice structure from fcc Cr to bcc Cr.
- Microcrystal: 10^3 to 10^5 atoms: Surface size effects gradual decrease. However, small deviations from bulk properties are still observable.

2.2 Helium and Helium Droplets

Helium is an outstanding element due to its unique properties in comparison with other elements. For example, He has no triple point (point where solid, liquid and gaseous phase coexists) and can never reach its solid phase at normal pressure and it has the highest ionisation energy at 24.6 eV. However, the most prominent feature is its super fluid phase, that occurs at temperatures below 2.17 K (see Figure 2.1).

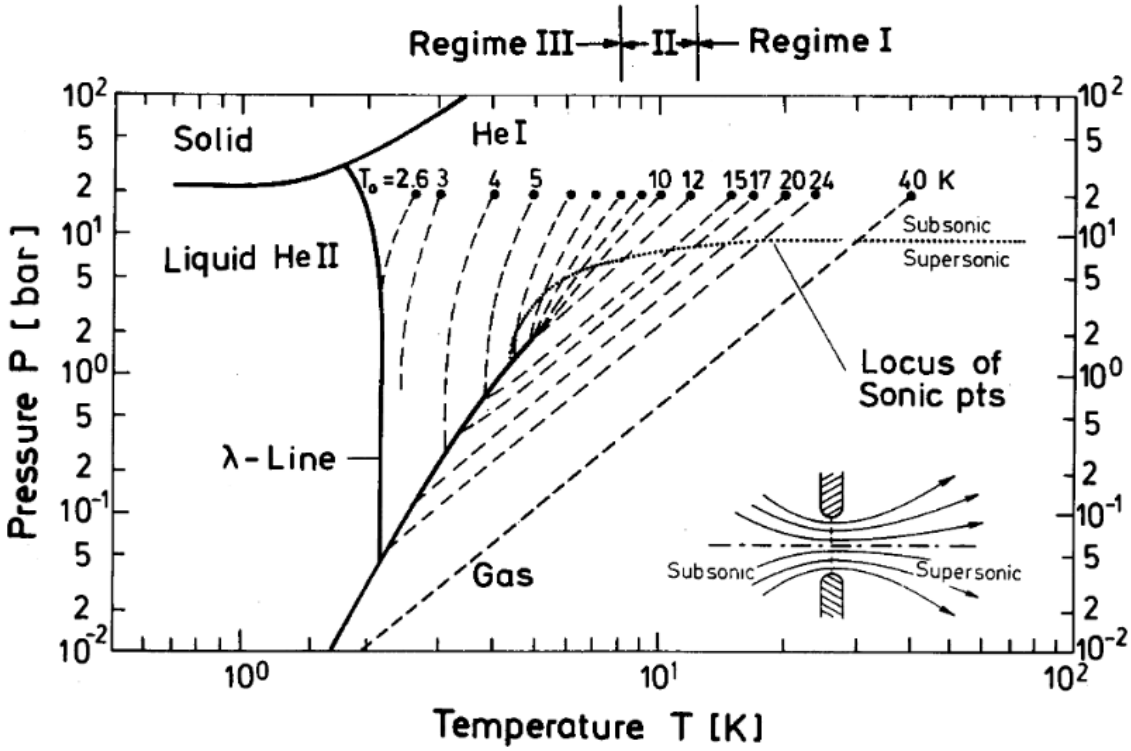

Figure 2.1: Phase diagram of liquid ^{4}He. The two phases He I and He II indicate the liquid phase (He I) and the super fluid phase (He II). Isentropes (dashed lines) for the subsonic and supersonic nozzle expansion can be seen (Taken from [46].)

Superfluidity is due to the thermal de Broglie wavelength of He II, which becomes larger than the interatomic distance between the single He atoms:

$$\lambda_{thermal} = \frac{h}{\sqrt{2\pi k_B m T}} \geq d_{He} \approx 5\text{Å} \tag{2.1}$$

As a result the He atoms lose their particle character and can be treated as a collective via a macroscopic wave function. In this wave like state, He II becomes an ideal thermal conductor, and the inner friction diminish.

Those properties of He II are used to create nearly ideal environments for cluster synthesis, as metal atoms can form clusters in an almost frictionless, ultracold He matrix. The standard method for creating He droplets is via an adiabatic supersonic expansion of highly purified He (usually grade 6 He = 99.9999 % He) under a stagnation temperature ($T_{CH} = 4...20$ K) and pressure ($p_{He} = 5...60$ bar) into vacuum ($p_{SC} \approx 10^{-6}$ mbar). Due to the adiabatic expansion process, the droplet cools down even further and can reach final temperatures of $T_{droplet} \approx 0.4$ K.

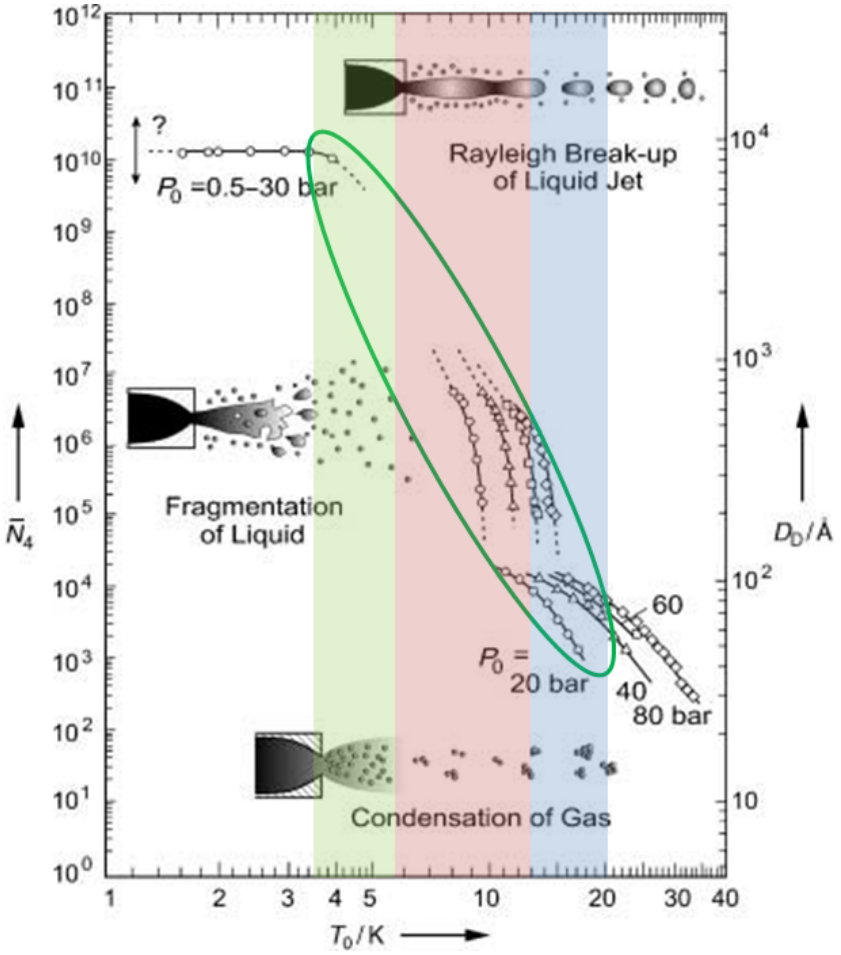

Figure 2.2: Mean number of He atoms $\bar{N}$ of one He droplet, respectively its diameter D_D as a function of the nozzle temperature T_0 and the stagnition pressure p_0 for a 5 μm nozzle. Three different droplet regimes are highlighted (Green: large droplets ($\bar{N} \approx 10^{10}$) synthesized via Rayleigh break-up of the liquid jet. Red: average sized droplets ($\bar{N} \approx 10^4...10^{10}$) which result from the fragmentation of a liquid jet. Blue: small droplets ($\bar{N} \approx 10^1...10^4$)). Reprinted from [60]

The droplet size distribution depends on the stagnation temperature (also referred as the cold head temperature T_{CH}), which determines the droplet formation regime. Three

different regimes have been found so far (see also Figure 2.2)

- Sub-critical regime [59](blue region in Figure 2.2): The size distribution is described by a log-normal distribution with $\bar{N} \approx 10^1...10^4$ atoms. The formation of droplets are due to the condensation out of the gas phase.
- Supercritical regime [32] (red region in Fig.2.2): The droplet size is exponentially distributed with $\bar{N} \approx 10^4...10^{10}$ atoms. Droplets are fragmented out of a liquid He jet.
- Rayleigh breakup regime [23] (green region in Fig.2.2): Droplets are bimodal distributed with $\bar{N} \approx 10^{10}$ atoms. In this region, the so called Rayleigh break-up of the liquid jet occurs.

2.3 Doping of He Droplets

In addition of being superfluid, the droplets are capable of picking up atoms of foreign species within the droplets cross section during their flight time. Inside the nearly viscous-less environment the foreign atoms can move (almost) freely (see next chapter), collide and also coagulate inside the droplet [22]. When such a coagulation process happens the binding energy of the foreign atoms is released and as a consequence this energy is dissipated by the droplet which results in an evaporation of He atoms that overcome their binding energy $E_{He,bond}$. As the binding energy of He ($E_{He,bond} = 0.62$ meV [51]) is much smaller than the binding energy released by metal atoms (i.e. $E_{Au,bond} = 3.81$ eV), one bond of i.e. Au atoms results in the dissipation of roughly 6000 He atoms. This gives an upper limit for the possible cluster size.

Additionally, quantised vortices are formed within the droplet at sufficiently low stagnation temperatures ($T_{CH} \leq 6$ K [60]) as a result of the manifestation of angular momentum which has to be conserved even in He II. The angular momentum in this regime is due to the contact of the droplets with the nozzle wall during expansion which induces an angular momentum. After He undergoes a phase transition due to the adiabatic supersonic expansion, this angular momentum is transferred into quantised vortices. Gomez *et al.* [18] have shown that impurities inside the droplet will, migrate to the quantised center of rotation and form elongated clusters, so-called nanowires, at these spots. This is a result of a pressure gradient pointing towards the vortices.

Chapter 3

Experimental Setup

In this chapter, the basic principles and mechanism of the apparatus, required for nanoparticle synthesis in helium droplets (short: HelENA - Helium Environment for Nanoparticle Assembly), will be presented. The apparatus stems from Prof. Christof Wöll department at the Universität Bochum and was transformed and extended at the Technische Universität Graz by Philipp Thaler, Johannes Steurer and Alexander Volk during their diploma and doctoral thesis (PT: doctoral thesis [55], JS: master thesis [51], AV: doctoral thesis [64]) starting with the construction phase in 2011. During the construction phase(s), several crucial features for the apparatus, such as a time-of-flight mass spectrometer (TOF-MS) for *in-situ* observation of metal clusters, and a manipulator for the deposition of nano particles on electron microscopy grids for *ex-situ* observations were added. In order to avoid rewriting a complete description with all details the author decided to keep the description in a nutshell and refers the reader to use [55],[64],[51] if further reading is required.

3.1 General Apparatus Structure

The whole setup consists of three separable vacuum chambers:

1. Source chamber: Production of liquid He droplets.
2. Pickup chamber: Doping of He droplets with metal atoms, which arrange themselves to clusters inside the droplet.
3. Main chamber: Diagnostic chamber to characterise the droplets either *ex-situ* or *in-situ* with external devices after deposition on i.e. an electron microscopy grid.

An illustration of the whole setup is shown in Figure 3.1 below.

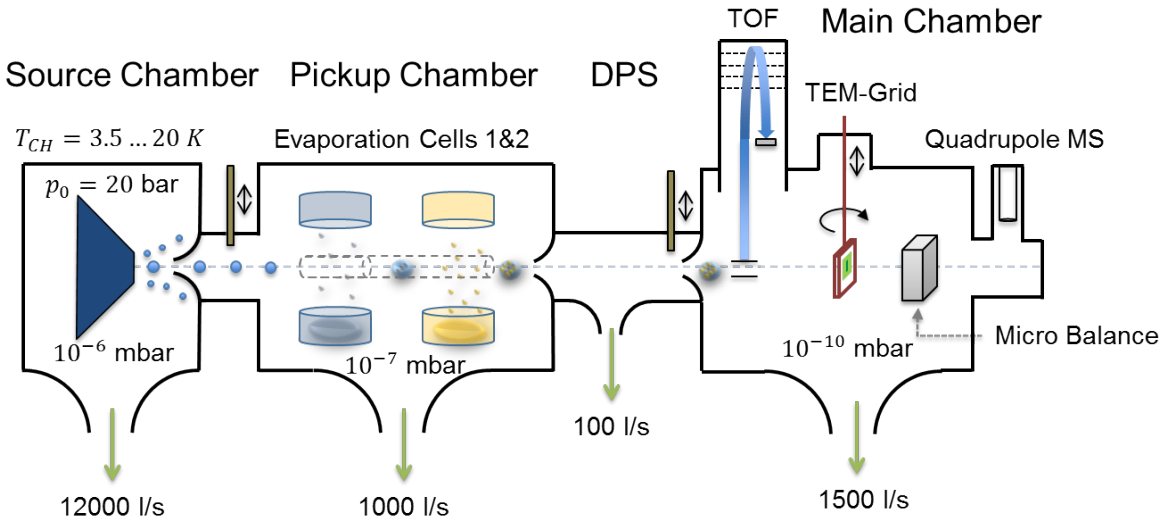

Figure 3.1: Schematic image of the experimental apparatus used for the production of metal clusters inside liquid He droplets. The setup consists of three separable chambers (source- (SC), pickup- (PC) and main chamber (MC)). In the SC, the liquid He droplet beam is produced by the cooled nozzle of the cold head (usually with temperatures between 3.5 and 20 K and at He pressures of mostly 20 bar) and tailored when passing through the skimmer. The droplet is then doped inside the PC with up to two metal species, that form clusters during their time of flight from the PC through a differential pumping stage (DPS) to the MC. Inside the MC, a TOF-MS is used for the *in-situ* analysis of the cluster size either by electron impact ionisation (implemented) or via laser induced photo-ionisation. A quartz-crystal micro balance scale is used for the determination of the total transferred metal cluster mass and a quadrupole mass spectrometer is essential for the determination of the remaining residual gas, mainly to determine the amount/size of He droplets. Finally, a manipulator for the deposition on mounted electron microscopy grids is implemented.

3.2 Source Chamber

In the first chamber, liquid He II droplets of high purity He (grade 6 He = 99.9999% pure He) are produced by a closed-cycle refrigerator (Sumitomo, RDK-408D2). The He enters the nozzle-setup at high pressures of $p_{He} = 20\,bar$ and is then cooled via a Gifford McMahon process [51]. After the second cooling stage, He can reach temperatures even below 4 K, He enters the nozzle, in which it expands through a 5 μm nozzle plate in an adiabatically supersonically way into the SC and cools down even further (≈ 0.4 K). This two staged cold head (CH) is capable of providing a cooling power of 1 W at 4 K (see[55]) which is necessary to enable the production of He droplets within the Rayleigh breakup regime.
According to adiabatic expansion the final temperature is far below the He temperature inside the cold head in the range of a few hundred mK. The colder the temperature of the cold head T_{CH} gets, the bigger the created droplets get according to Gomez *et al.*[17], who summarised the droplet size as a function of the nozzle temperature. It is essential for the later experiments to know the droplet size as a function of the nozzle temperature T_{CH} because the size of the droplet describes the pick-up cross-section for dopant's [51].

Table 3.1: He droplet size as a function of the nozzle temperature T_{CH} found by Gomez *et al.*[17] at a nozzle pressure of $p_{CH} = 20\,bar$.

Nozzle temperature T_{CH} / K	Average number of He atoms N_{He}
5.4	$1.68 \cdot 10^{10}$
5.7	$1.43 \cdot 10^{9}$
6.0	$3.08 \cdot 10^{8}$
6.5	$3.50 \cdot 10^{7}$
7.0	$2.20 \cdot 10^{7}$
8.0	$5.60 \cdot 10^{6}$
9.0	$1.82 \cdot 10^{6}$
9.5	$3.25 \cdot 10^{5}$
10.0	$6.39 \cdot 10^{4}$
11.0	$1.50 \cdot 10^{4}$
12.0	$1.20 \cdot 10^{4}$
13.0	$8.00 \cdot 10^{3}$

Finally, the free jet He beam passes through a skimmer (see Figure 3.1) where the He intensity is lost to create a coherent beam of droplets. As a consequence, a huge throughoutput/pumping rate of an oil diffusion pump of 12000 l/s is necessary to keep the pressure inside the chamber as low as $p_{SC} \approx 10^{-5} mbar$.

3.3 Pickup Chamber

After passing the skimmer, the coherent He droplet beam enters the pickup chamber (PC), where the droplets are doped with metal atoms of the desired species (within this thesis a large variety of metals such as Pd, Au, Ni, Cu, Ag, Bi, Al and Cr are investigated). For the pickup event to take place the desired species have to be heated up to their corresponding vapour pressures. An exemplary metallic vapour pressure graph can be seen in the figure below:

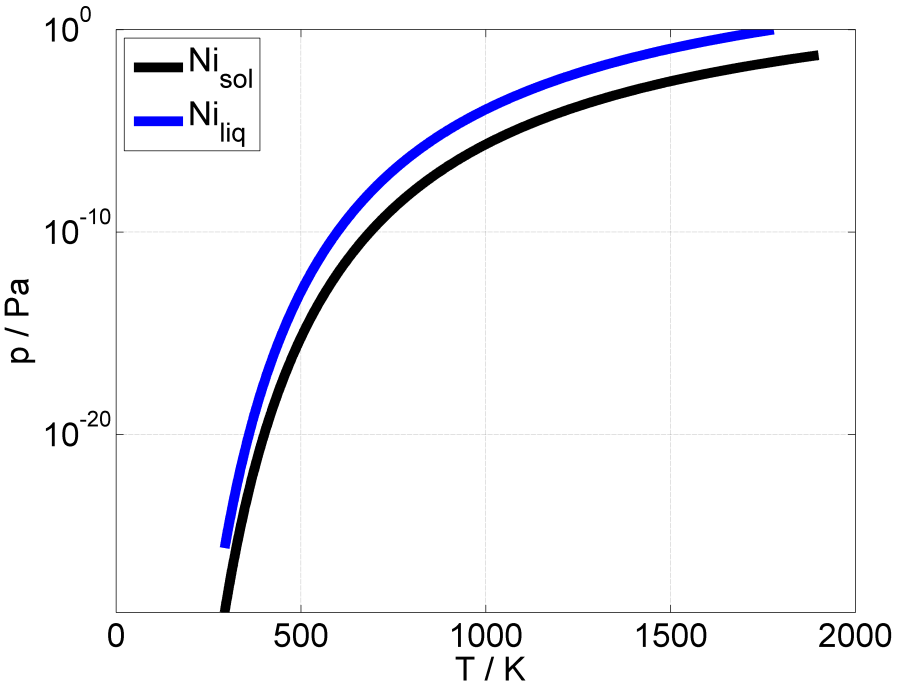

Figure 3.2: Vapour pressure curve for nickel as a function of its temperature. The metal temperature has to be increased till a sufficiently high vapour pressure is reached to start evaporating metal particles. They are then picked up by bypassing He droplets and form clusters inside the droplet. In addition, it should be considered that the vapour pressure curves for metals in liquid and solid phase may have a rather large deviation (material specific parameters taken from [24]).

The chamber consists of two separate evaporation cells. Both of them consist of two crucibles, where the first is located at the bottom below the beam and the second one is placed above the beam to keep the gaseous metal atoms in the desired region between the two crucibles and thereby the loss of metal particles is reduced. In addition, the crucibles are covered with a water cooled heat shield to protect other components inside the chamber. The droplets enter the crucibles at a 90° angle and picked up particles which are inside the droplet cross section. Optionally, a liquid nitrogen cooled cooling trap is used to condense residual gas, mainly water molecules, at its surface in order to

reduce the pressure in He pickup chamber. However, it is only necessary to use the cooling trap in cases where only small intensities are measured by the diagnostic apparatus.

As illustrated in Figure 3.2 the evaporation cell temperature has to be raised to increase the amount of metal atoms inside the He droplets cross section. It is highly important to find the appropriate relation between droplet size and the amount of picked up cluster atoms. Along the droplet's flight path He evaporates when flying through the chamber and picking up metal atoms. This is a result of the cluster formation process inside the droplet during the flight time, during which the binding energy from metal atoms is released when two atoms 'find' each other inside the droplet (see also chapter 1).

In addition, the cluster aggregation processes change inside big droplets ($N > 10^6$ atoms) from single- to multi-center growth (see also [51],[55],[64]). This phenomenon is called multi-center aggregation. Therefore the main goal of the cluster production process is to create clusters with a desired average size by varying the droplet size (via variation of T_{CH}) and the temperature of crucibles (via variation of T_{EC}).

To guarantee a stable, reproduceable temperature of the evaporation cell(s) an electric resistance method is used to measure and determine the temperature via measuring the electrical resistance of the heating wire of the crucible, which is temperature dependent. [55]

$$R_T = R_{20°C}\left[1 + \alpha\left(T[°C] - 20°C\right)\right] \tag{3.1}$$

with $\alpha = 0.0044$ K for tungsten and $R_{20°C}$ being the resistance of the heating wire determined at $20°C$.

In addition, the temperature can be measured via a thermocouple Type C, which is placed inside the chamber, preferably directly inside the crucible. However, differences between the determined and measured temperature of more than 100 $°C$ are observed (see also [48]), which is due to the impossibility of measuring exact temperatures inside the metal species and due to heat losses resulting from the thermal contact between the the covering husk and the watercooled shield. On the other hand, the temperature measurement via the resistance of the crucible is not exact either, because not only the voltage drop across the crucible but also the entire setup is measured. As a result, temperature values have to be treated with caution, taking into account that both temperature measurements have significant sources of possible errors.

3.4 Differential Pumping Stage

After the doping process is finished, the droplets pass through another skimmer, with a diameter of 3 mm and enter the differential pumping stage (DPS). The main purpose of this chamber is to decrease the pressure gradient between the PC ($p_{PC} \sim 10^{-7}$ mbar) and the MC ($p_{MC} \sim 10^{-10}$ mbar). As the volume of this chamber is rather small, pressures

in the range of $p_{DPS} \sim 10^{-9}$ mbar can be reached, which guarantee a collisionless flight of the droplets till they reach the MC.

3.5 Main Chamber

The last chamber consists of the main diagnostic tools to measure the properties, such as mass, size, reactivity and composition of the generated clusters. Therefore a very good and oil free ultra high vacuum (UHV) is crucial to avoid contamination of the droplets/clusters. However, oil steaming from the SC can reach the MC, in which oil peaks are visible in the mass spectrum ($m = 203$ u,$m = 276$ u and $m = 390$ u). As illustrated in Figure 3.1 the MC contains several diagnostic features such as:

- Time-of-flight mass spectrometer (TOF-MS) for the determination of the cluster and droplet size distribution and their composition.
- Moveable sample holder with mounted TEM grids for the preparation of TEM grids for electron microscopy.
- UHV-Transfer-System for the deposition of clusters at substrates like glass plates and for the transport of higher reactive clusters to avoid contact with ambient air.
- Quartz crystal microbalance to determine the mass deposition rate.
- Quadrupole mass spectrometer to monitor the residual gas inside the chamber.

In the following subsections these tools are described in more detail.

Time-of-Flight Mass Spectrometer

As illustrated in Figure 3.1 the TOF-MS with a reflectron (Stefan Kaesdorf RFT50) is installed in the first section of the MC. As the name suggests the TOF-MS measures the flight time of ionized particles until they impact, and converts this time of flight into a mass spectrum, as one flight time can be directly linked to the corresponding particle/cluster mass via the relation $\dot{x} = eUt/m$. The ionisation process of particles/clusters can be either realized via implemented electron impact ionisation or via laser induced ionisation. In addition this TOF-MS is designed to detect especially heavy particles with $m \geq 20000$ amu in order to serve properly as a control instrument for the nanoparticle synthesis.

Quartz Crystal Scale/Micro Balance

For the determination of the total mass deposition rate dm/dt of clusters deposited, a quartz crystal scale (also referred as micro balance) is installed. The micro balance can measure the amount of deposited mass on a quartz crystal. The basic mechanism is simple, the quartz crystal is stimulated via an electric circuit to oscillate at its resonance

frequency f_0. According to the Sauerbrey equation this resonance frequency f_0 will decrease when mass is deposited on the crystal (similar to the phenomenon when adding mass on a vibrating spring). The change in frequency can be written as [63]:

$$\Delta f = -2f_0^2 \frac{m}{\sqrt{\rho_0 \mu_0}} \tag{3.2}$$

The change of frequency is thereby proportional to the deposited mass and dependent on device constants such as the density of the quartz ρ_0, its shear modulus μ_0 and the resonance frequency f_0.

Quadrupole Mass Spectrometer

The last detector in the MC is the quadrupole partial pressure analyser (also referred as quadrupole mass spectrometer). It is capable of detecting masses between 0 and 200 amu, which is the reason why this sensor is basically used for the detection of residual gas. The QMS is on the one hand used to determine the amount of residual gas, such as O_2, N_2, H_2O, CO, etc. to determine the vacuum quality, respectively to determine if the chamber has a leak. On the other hand it is used to measure the amount of He_1 and He_2 inside the MC, which is proportional to the He flux. From this measurements also the amount of evaporated He during the cluster formation process can be determined, as the partial pressure of He decrease, when the droplets shrink inside the PC and the DPS due to the cluster formation process.

Moveable Sample Holder

In order to deposit clusters on substrates (e.g. TEM grids), a surface deposition unit, which is mounted on a six-axis manipulator, is installed. During the experiments, after the desired settings for cluster deposition are found, the grids can easily be swung into the He beam and up to two different TEM grids can be deposited with the desired amount of the requested clusters (see Figure 3.1). The big advantage of this system is, that it takes only one to two seconds till a grid can be placed into the He_N beam and when venting the MC with dry nitrogen the exposure to ambient air can also be minimized.

One of the main advantages is, that the sample holder could either be cooled with liquid nitrogen or heated via a bulb. This allows to change the deposition temperature between $T_{deposition} \approx -150°C$ (not exactly $T_{N_2,liq}$ due to heat losses) and $T_{deposition} \approx 130°C$. The higher temperatures are used to reduce the amount of contamination on the grids before deposition and the lower temperatures are used to create clusters/nanowires which are only stable at temperatures below the room temperature.

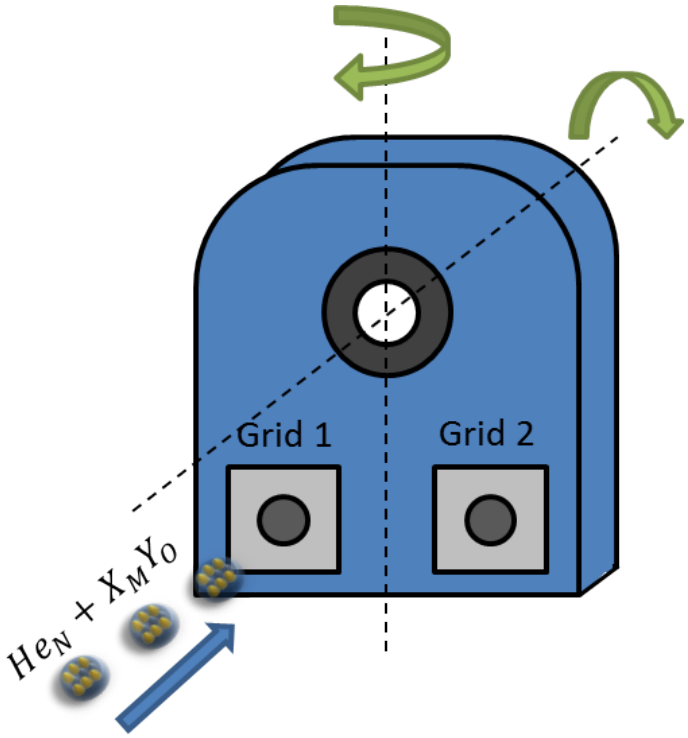

Figure 3.3: Illustration of the moveable sample holder which is capable of being equipped with up to two TEM grids. The position between the two grids can easily be changed, when rotating the holder around the manipulator axis.

3.6 Transmission Electron Microscopy Grids

For the sake of investigating structures on the nanoscale, those structures have to be deposited on ultra thin layers in order to analyse them via transmission electron microscopy (see also Figure 3.3). Within this thesis two different types of carbon grids (typical thickness of the substrate carbon layer $\sim$ 5 nm), either a heatable substrate (DENSsolutions Nano-Chip XT carbon) or an amorphous carbon grid (Ted Pella, Inc., Prod. No. 01824) are used. The big advantage of carbon in contrast to other substrate layers is its high transmissivity, additionally it provides fine grains and low contrast and it shows low interaction with the deposited structures. In addition it seems, that different substrate materials, like silicon nitride, tend to offer a much higher surface mobility for clusters, especially for lighter materials [42]. However, silicon nitride is capable of supporting higher grid temperatures (up to $1000°C$) and offers a higher chemical inertness in comparison with amorphous carbon grids (up to 800°C) [27]. The reason why a supporting bottom structure of amorphous carbon is required, is that clusters and nanowires in the range of a few nanometer mostly do not have a 'self-supporting' structure.

In order to be able to study thermally induced surface diffusion processes of clusters and nanowires, which is the main goal of this thesis, it is crucial to be able to enable

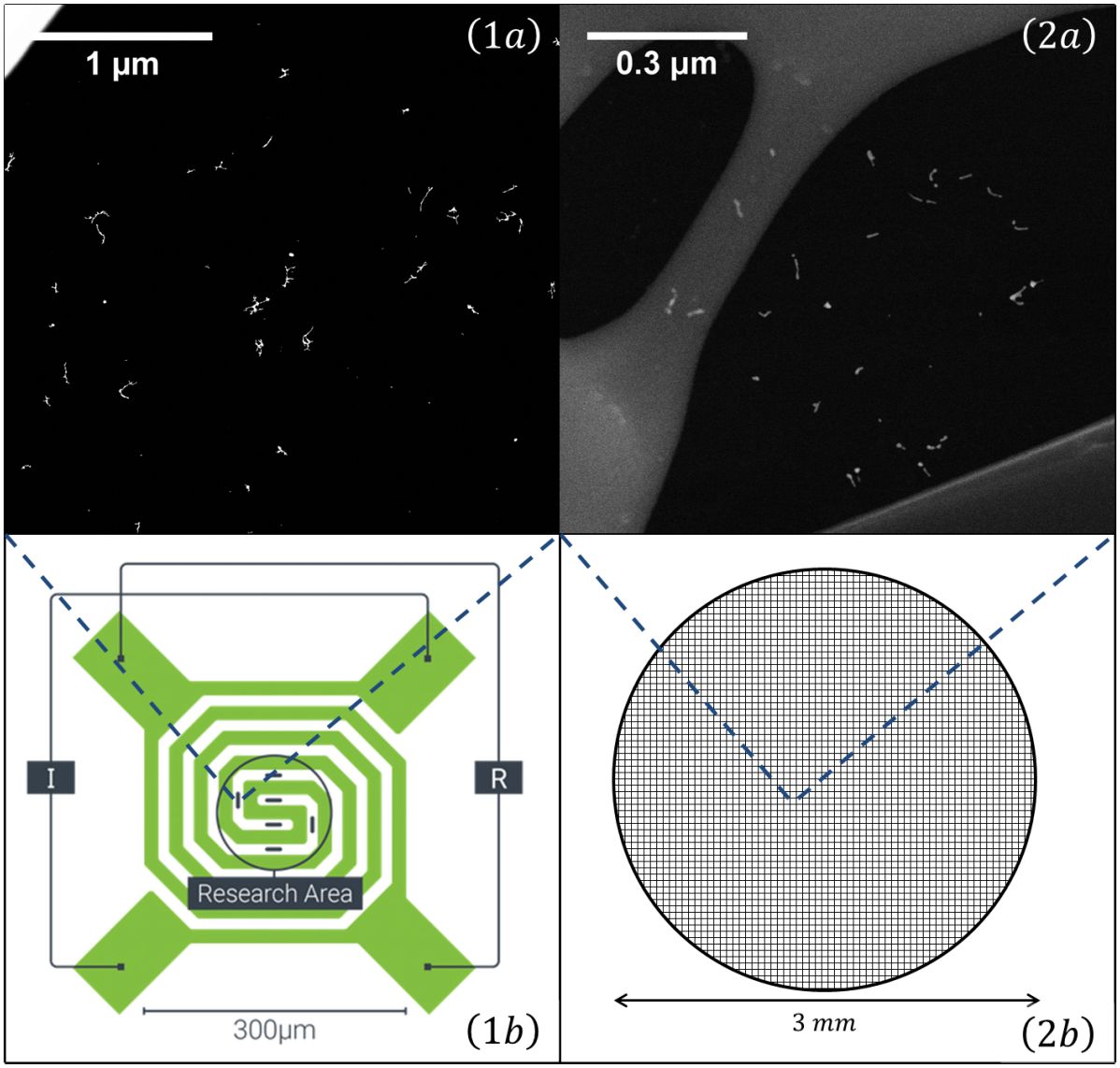

Figure 3.4: Overview of the two different transmission electron microscopy (TEM) grids used within this thesis. Two different kinds are use, on the one hand a heatable carbon TEM grid (1) (DENSsolutions Nano-Chip XT carbon) which is able to provide a temperature range between room temperature and 1300°C. The carbon windows are embedded inside a heatable filament. The second grid (2) is an amorphous carbon grid used for cryogenic experiments, ranging from $-150°C$ up to room temperature. A close up view of the two different carbon windows can be seen in the upper two figures (1a and 1b). It is easy to identify the difference between the larger, but less numerous windows of the heatable grid and the amorphous carbon grid, which consists out of several smaller windows. (Note: Figure 1b is taken from [27])

an *in-situ* measurement inside a transmission electron microscope. Both types of grids are used to cover in total a wide temperature range for *in-situ* observations. As already previously mentioned, cryogenic experiments are carried out to investigate surface diffusion processes between $-150°C$ and $20°C$. For the low temperature regime non-heatable amorphous carbon grids are used (Ted Pella) and the heat up process is a result of the heat transfer inside the electron microscopy. To investigate structures which are stable at room temperature a heatable carbon grid (DENSsolutions) is used, which is capable of inducing an electric current into the chip and as a result regulating the temperature. This four point resistive contacting method (see Figure 3.4) is able to cover a temperature range from room temperature up to $1300°C$, with an average temperature error below 5% and offering a very high maximum heating rate of $200°C/ms$ [27]. However, due to the heat up process a sample drift of roughly 1 nm per minute [27] is not avoidable. Nevertheless even with sample drifts a minimal resolution smaller than Å can be achieved.

3.7 FEI Titan Transmission Electron Microscope

For the investigation of deposited clusters and nanowires and their thermally induced surface diffusion processes, a scanning transmission electron microscope (STEM), more precisely an image corrected FEI Titan3 G2 60-300 is used. The goal is to perform *in-situ* observations with atomic resolution to investigate the very nature of these processes.

The basic principle behind a STEM is rather straight forward. It consists of an electron emission source, electromagnetic lenses and an electron detector. A very thin sample/grid is implemented in between the electron gun and the electron detector. Electrons are emitted by an electron gun, they are then accelerated, collimated by the sample lenses and then pass through the sample. As a result of the interaction processes of electrons with the sample, the beam is modified and can therefore give information about the structure of the sample. In the scanning mode (STEM) the beam is focused on one point of the sample and is then scanned over the hole region of interest in order to create a profile structure.

However, in order to increase the signal collection efficiency and to get a material contrast (Z-contrast) a high-angle annular dark-field imaging (HAADF) is used. This technique collects the scattered electrons, which are on the one hand more numerous than the small angle scattered electrons and one the other hand allows the main beam to pass through the sample to an electron-energy loss-spectrometer (EELS). HAADF is highly sensitive to changes in the specimens'thickness stacked above each other, which can give informations about the three-dimensional shape of the sample. EELS is used to analyse the loss of energy of the electron beam, caused by inelastic scattering, steaming from photon excitation, inter band transitions, plasmon excitations, etc.. This technique is used to identify specimen atoms with rather low atomic numbers, as the excitation edges tend to be rather small in this range. EELS is often combined with energy-dispersive

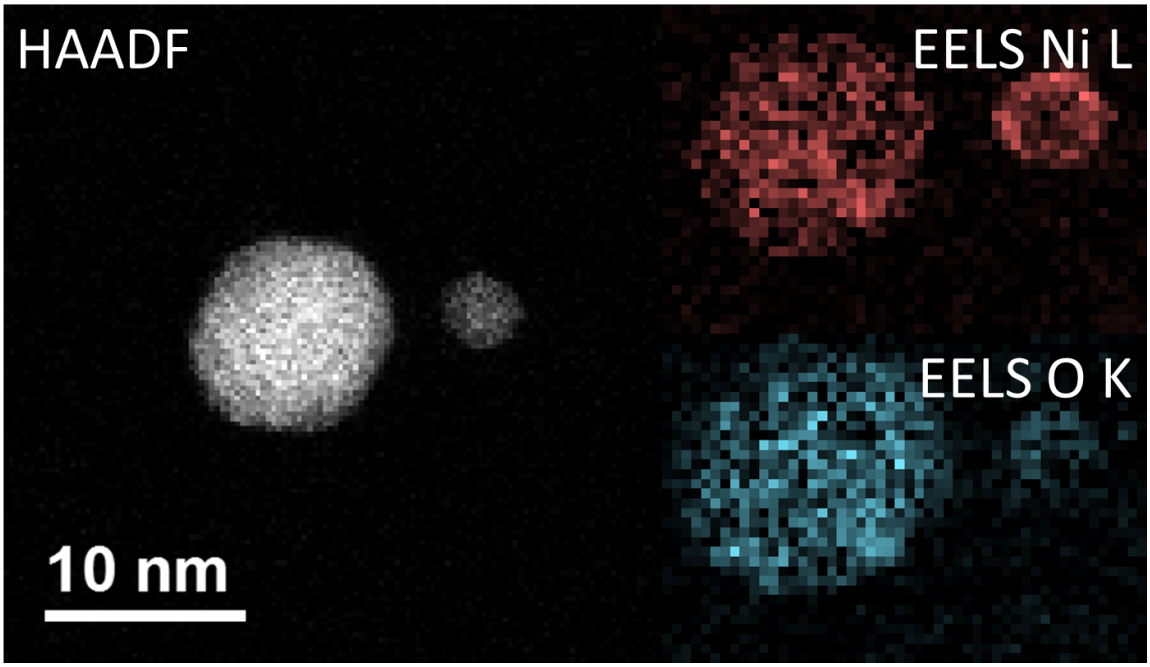

Figure 3.5: A comparison between the high-angular annular dark-field technique (HAADF) and the electron energy loss spectroscopy method (EELS). All three images are taken from the same region on a heatable carbon TEM substrate, where two nickel nanoclusters are deposited. In the left image the HAADF signal is illustrated, where a material contrast and also a Z-contrast is clearly visible. This is caused by different amounts of layers stacked above each other. When using EELS, it is possible to separate nickel and its covering oxide layer, as the energy lost by the low angle scattered electrons is highly sensitive to changes in the atomic number for small Z. As there are material specific energy bands for EELS a separation of the elements can easily be done.

x-ray spectroscopy (EDX), which uses the generated x-ray excitations of the specimen to create a chemical characterization of the sample. EDX is used to investigate materials with larger atomic numbers, complementary to EELS. In Figure 3.5 a small illustration is drawn to compare HAADF with EELS signals.

The big advantage of an image corrected FEI Titan3 G2 60-300 is its comparably large electron emission stability (changes of less than one % during one week). The system is protected with an acoustic, thermal and elctro-magnetically isolated support box, which reduces the exterior influences to a minimum [26]. With this microscope it is possible to cover a wide range of acceleration voltages ranging from 6 to 300 kV, which enables the investigation of a large amount of different materials and compounds of specimen. The resolution is limit with 70 pm and with an energy resolution of 0.15 eV. As a result the microscope can detect even single atoms [26]. The microscope is equipped with a

Gatan Quantum energy filter for electron energy loss spectroscopy and a four-quadrant energy-dispersive X-ray spectroscopy detector (FEI Super-X), for the determination of material compositions.

Chapter 4

Experimental Procedure

The aim of this chapter is to act as an introductory guide to fully understand the symbiosis of several measurement tools and the underling mechanism behind the synthesis of clusters and nanowires. Therefore, this chapter will give a guideline how to generate clusters, nanowires and core-shell particles with the desired pairing of metal species and with a desired size and shape.

4.1 Synthesis of Monometallic Nanowires

4.1.1 Creation of He Droplets

In order to synthesis monometallic clusters and nanowires, the temperature of the cold head T_{CH} has to be reduced significantly low in order to generate droplets large enough for the formation of nanostructures inside the He environment. This is realized when using temperatures between $T_{CH} = 4...20$ K (see also chapter one Figure 2.2 and chapter three Table 3.1). As already previously mentioned T_{CH} not only determines how many clusters can be picked up, but it also determines the elongation of the clusters. For small temperatures ($T_{CH} = 9...20$ K) a single center aggregation inside the droplet determines the growth process for small metal clusters. When decreasing the temperature below $T_{CH} = 9$ K more than $\bar{N}_{He} \approx 10^6$ atoms are within one droplet and therefore a multi center aggregation can occur [40]. However, when increasing the doping rate, this phenomenon can be suppressed, as the droplet shrinks as a result of the release of binding energy from the doped foreign atoms. Nevertheless, this leads to elongated clusters for $T_{CH} = 6...7$ K as in this temperature regime the initial multiple centers will form larger spherical clusters which will then attach in a short wire-like structure to each other. For temperatures below $T_{CH} = 6$ K [60] the formation of vortices leads to the agglomeration of metal particles at these quantized vortices, leading to the formation of nanowires.

4.1.2 Doping of the He Droplet

When the droplets reach the pickup chamber (PC), they can pick up metal atoms within their cross section, which are brought into gas phase via two evaporation cells. The amount of metal atoms which are in gas phase is determined via their temperature and vapour pressure. In Figure 4.1 a variety of different vapour pressure curves for different

materials used within this thesis, is drawn. The vapour pressure corresponds to the pressure of a vapour above the liquid/solid. In other words - it describes how likely particles can reach gas phase. Alcock *et.al.* have found a general relation between the temperature of metallic elements and their vapour pressure [2]

$$\log(p/\mathrm{Pa}) = 5.006 + A + \frac{B}{T} + C \cdot \log(T) + \frac{D}{T^3} \tag{4.1}$$

This equation uses four different material specific parameters (A, B, C and D) and is able to predict the vapour pressure within an accuracy of 5% [24].

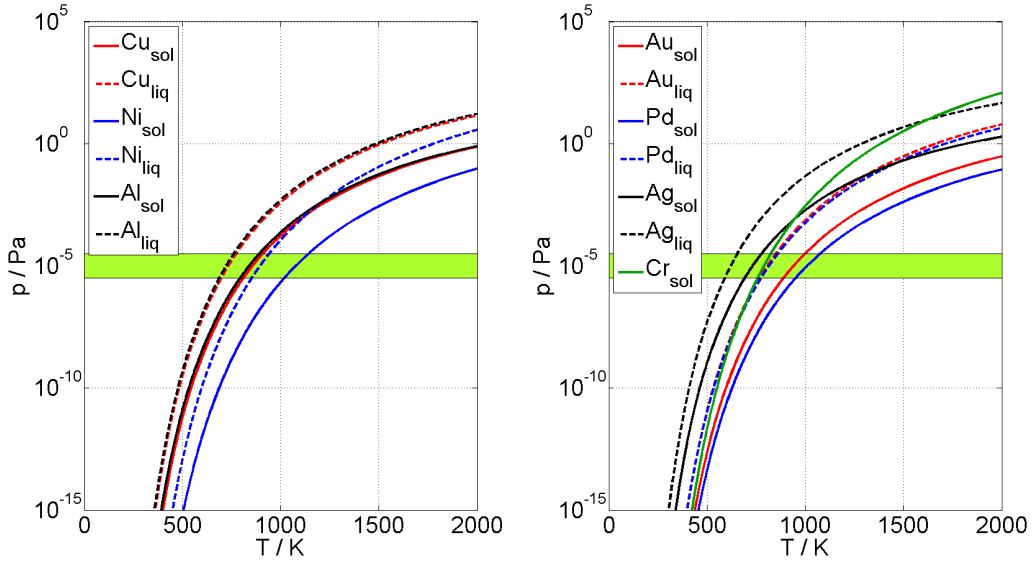

Figure 4.1: Vapour pressure curves for a nearly all materials (Cu, Ni, Al on the left hand side and Au, Pd, Ag and Cr shown on the right hand side) used within this thesis. For each meaterial (exepct Cr) vapour pressure curves for both phases, liquid (- -) and solid (-) are drawn. For all depicted materials, the liquid vapour pressure is higher than the solid vapour pressure. In green the typical pressure within the pickup chamber is indicated. The curves follow the relation described in equation 4.1. The material specific parameters are taken from [24].

The main challenge of the doping process is the liquid-solid phase transition, as the liquid vapour pressure is higher than the solid one (see Figure 4.1). As a result when trying to dope the helium droplet with a larger amount of metal atoms, it is very likely that the metal can reach the phase transition temperature and a large jump in the doping rate is visible (decrease of the He signal in the quadrupole MS, higher deposition rate at the quartz crystal micro balance and a raise of the PC chamber pressure can be observed). In order to handle this problem the material inside the evaporation cells should be first melted and then the temperature should be decreased in small steps again to undercool the liquid and reach the desired deposition rate.

One other challenge occurs when dealing with materials, which tend to oxides. This can lead for some materials (e.g. Al and Al-oxide) to a covering layer of metal-oxide which has a higher melting point than the pure metal. There will be a liquid layer with a high vapour pressure underneath a solid metal-oxide layer and the pickup rate is quasi zero. However, when melting the oxide layer a large amount of liquid material can go into gaseous phase, as the pure metal vapour pressure is drastically higher than the metal-oxide one. This makes it rather difficult to deal with oxidable materials, as it is important to drastically increase the materials temperature and immediately decrease the temperature again when the oxide layer is liquified, in order to reach the desired pickup rate.

4.1.3 TOF Mass Spectrometry

The amount of picked up metal particles, their size distribution and the composition of multi-metal species can be analysed via the TOF-MS. Before doping the helium droplet, a continuous mass spectrum of peaks, which are separated by 4 a.m.u. is visible. At first glance this seems to be counter-intuitive, as the helium droplets should be much larger, than a few tenth or hundreds of helium atoms. However, this behaviour is a result of the electron impact ionization process, where an electron with an energy of 89 eV, much larger than the helium binding energy, is used to ionize the the particles. As a result of this high electron energy a fragmentation process of the droplet occurs and only the fragmented mass becomes visible within the TOF mass spectrum (see exponentially decaying helium background signal in Figure 4.4 and Fig4.2).

When doping the droplet with metal clusters, the vapour pressure has to be increased till the probability for a pickup from the helium droplet is large enough. As the temperature of the evaporation cell, respectively of the corresponding dopant metal, becomes larger, also the amount of metal clusters which are measured increases. In addition the average cluster size becomes larger, if the evaporation cell temperature is increased, as a result of a bigger pickup (see Figure 4.2 for the effect of an increasing doping rate). With the pickup of larger structures the same problem as for larger helium droplets occur. As most metals do not only have one stable isotope, but rather a couple of different isotopes, a metal$_N$ cluster can have a large set of isotope compositions. Therefore the mass of a cluster with a given amount of metal atoms N is multinomially distributed. The goal to determine the probability $p(N,M|\vec{p},\vec{n})$ to find a cluster with a total mass M and having N atoms is discussed in more detail in the appendix section 8. With the knowledge how the cluster size $p(N = \text{const},M|\vec{p},\vec{n})$ is distributed it can be estimated up to which N_{crit} two different cluster sizes N and $N+1$ can be separated by 95% significance level, equivalent when the two maxima of N and $N+1$ are separated by four standard deviations σ_{crit}. In the following table the critical values for separability are drawn.

Table 4.1: Critical values for the separability of clusters with a number N and $N+1$ of atoms. The values for the limiting N_{crit}, M_{crit} and σ_{crit} with a significance level of 95% are drawn for five different elements used within this thesis.

Element	N_{crit}	M_{crit} / amu	σ_{crit} /amu
Ni	145	8514	14.69
Pd	202	21550	26.63
Cu	296	18862	15.90
Cr	470	24466	13.01
Ag	729	78758	26.99

It is visible in Table 4.1, that the more isotopes an element has (Ni has 6 stable abundances in comparison to two stable Ag isotopes), the smaller N_{crit} is. In addition, the closer the isotope masses are, the higher N_{crit} becomes, as the standard deviation σ stays rather small. N_{crit} should however only be seen as a maximum upper limit, as possible contaminations with water or multiple species mixing brings in additional mass peaks which overlap with the pure isotope distribution.

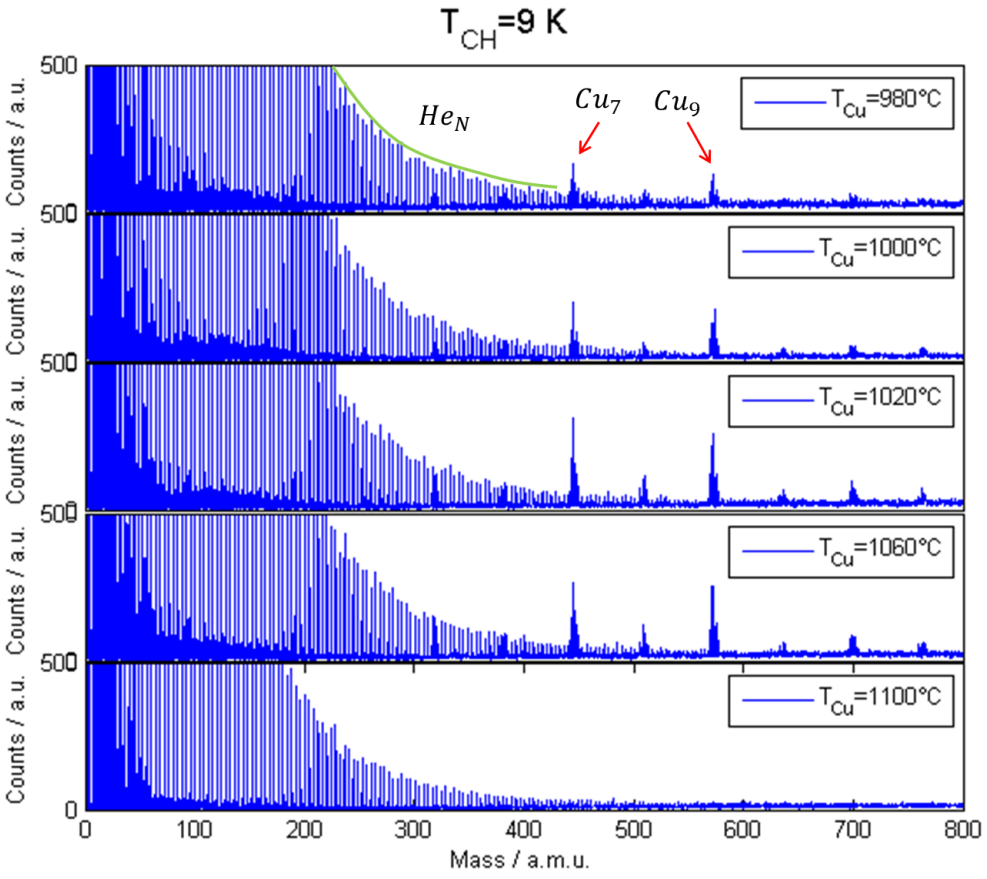

Figure 4.2: Mass spectra for copper analysed by a constant T_{CH} as a function of T_{Cu}. Two copper peaks and the helium background signal are indicated.

A typical mass spectrum for a constant droplet size (T_{CH} = const) is illustrated in the following Figure 4.2. It is visible, that with increasing evaporation cell temperature the amount of metal atoms in one helium droplet increases, which is manifested in the total amount of metal clusters detected. In addition to the increase in pickup mass also the average size of one cluster increases. So the higher the evaporation cell temperature T_{EC} becomes, the more mass is picked up, but not only the amount, also the cluster size becomes larger. However, when a certain T_{EC} is reached too many atoms are picked up by one droplet, which leads to the total evaporation of helium, resulting in no mass transfer into the MC. How the clusters with more atoms increase and decrease again is illustrated in Figure 4.3.

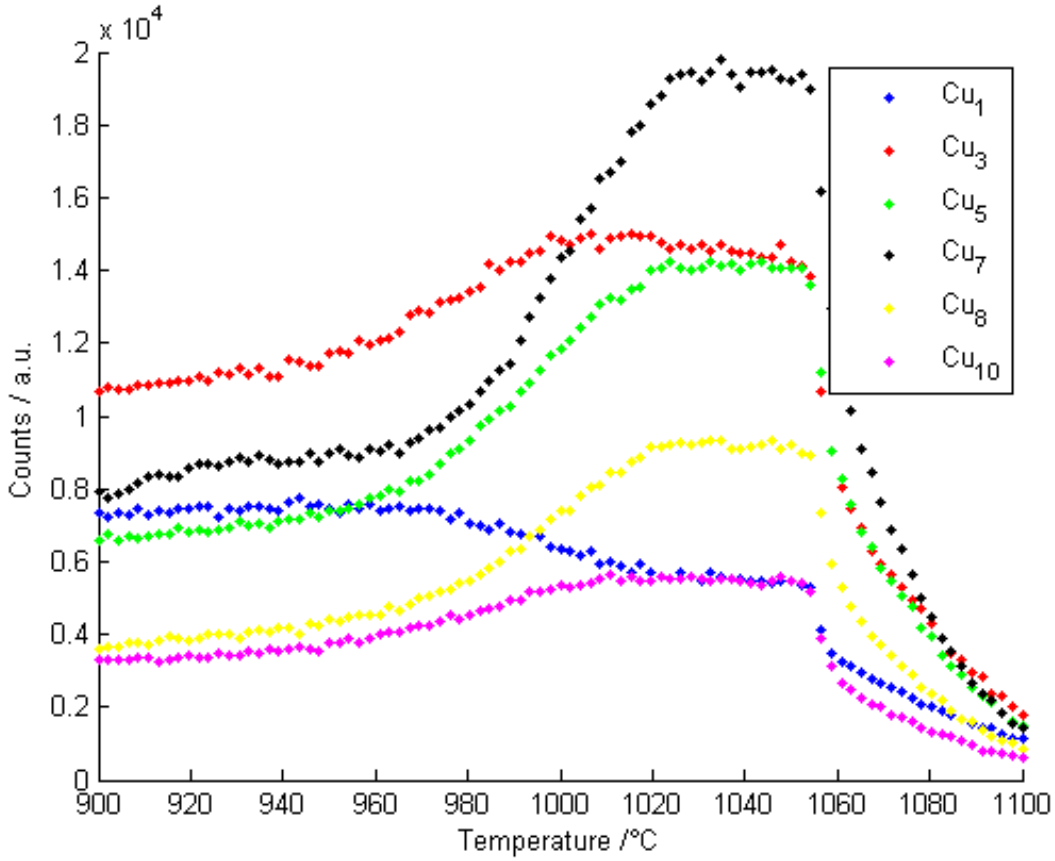

Figure 4.3: Copper N clusters abundances as a function of the evaporation cell temperature T_{Cu}. The counts in a.u. for a copper cluster with N = {1,3,5,7,8,10} are recorded at a constant helium droplet size with T_{CH} = 9 K. For high T_{Cu} the helium signal diminishes due to the large amount of evaporated helium atoms as a result of the release of the metal bond energy release.

The second parameter which affects the cluster size distribution is the helium droplet size, which is controlled via the cold head temperature T_{CH}. When performing a measurement at a constant evaporation rate, regulated via the evaporation cell temperature,

the droplets first have to become large enough in order to sustain the release of a few bond energies, so that the release does not completely evaporate the droplet. When T_{CH} becomes smaller, the droplet size increases, consequently the droplets' cross section increases and more metal atoms can be picked up. This increases then the average cluster size. Especially for large droplets $T_{CH} < 7$ K the average cluster can have even more than a few thousands of atoms, so the maximum peak height decreases, as the size has a larger standard mass deviation σ_M.

In Figure 4.4 the effect of doping the helium droplet with a constant amount of metal atoms is studied as a function of the cold head temperature T_{CH}. During this experiments a constant helium pressure of $p_{He} = 20$ bar and a constant evaporation cell (filled with copper) temperature $T_{Cu} = 1060°C$ is used, while T_{CH} is varied between 8 to 11 K.

All in all the TOF offers the possibility of a very exact characterisation of the cluster composition. However, the analysis is limited to clusters with average sizes within $N \sim 10^0...10^3$. Larger structures have very large mass deviations due to size variations of a couple of N's and additional deviations from their multiple isotopes occur, which flatten out the signal over a large bandwidth of mass channels. Nevertheless the TOF is a crucial tool to create any cluster structure, as it serves as an analysation tool, which can determine possible contaminations inside the evaporation cells and determine/proof the purity of the used metals.

4.2 Deposition on TEM Grids

In order to prepare TEM grids, the cluster/nanowire size has to be predefined and the mass deposition rate obtained via the droplet mass transfer capability be taken into account.

For the creation of nanowires, the droplet sizes have to be large, so that every droplet can pick up a few thousand up to ten thousand dopant atoms, which are required for the formation of elongated structures. In addition the droplet should be synthesized within the Rayleigh breakup regime, so that vortices inside the droplet can be formed. Alongside these vortices the metal atoms agglomerate, which results in the formation of elongated structures/nanowires. This phenomenon has been detected within the last years by Gomez *et.al.* and Gordon *et.al.*, which were the first who predicted the possible capability, that helium droplets can form metallic nanowires along their quantized vortices [18],[20].

Nearly all nanowires described within this thesis are synthesized with droplets at a cold head temperature of $T_{CH} = 5.4$ K. This temperature ensures that droplets are synthesized via the Rayleigh breakup regime, but the droplets are not too large, so that a multi center aggregation occurs, which limits the maximum length of the agglomerated nanowires. In contrast to other techniques, this method can produce ultrathin nanowires with only a few nm thickness.

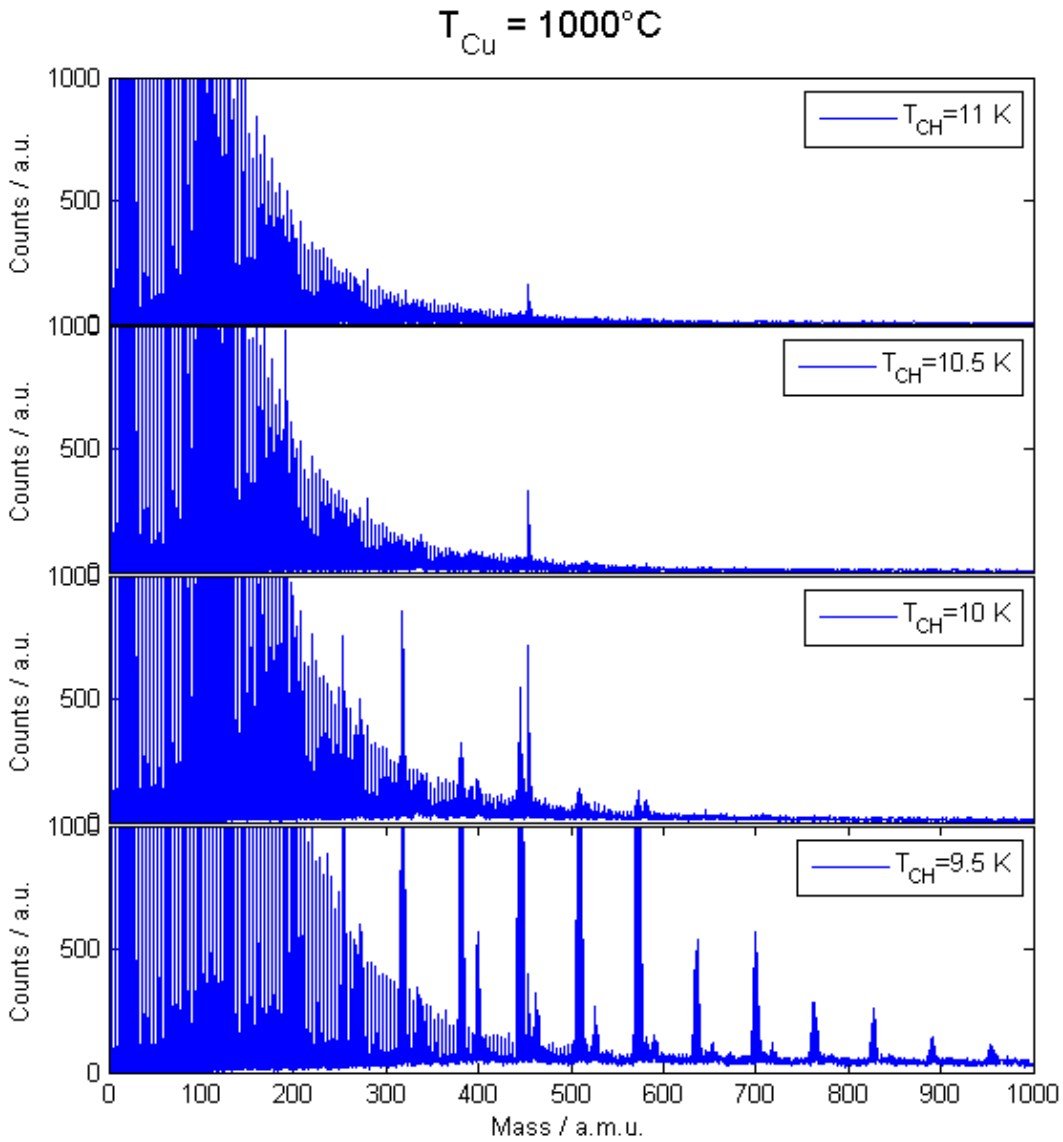

Figure 4.4: Mass spectra for copper analysed for a constant evaporation cell temperature $T_{Cu} = 1000°C$ as a function of the helium droplet size/cold head temperature T_{CH}. For small T_{CH} only very small clusters can be transported into the MC (overlapping helium and copper signal). The larger the droplets become the larger also the average cluster size N becomes, as well as the mass deviation σ_m (visible in the decaying Cu signal for small T_{CH}). As a result, there are fewer peaks at small masses, but a broad bandwidth of masses with small counts for each specific mass.

Before depositing the nanowires on a TEM grid the amount of helium droplets which reach the MC is recorded using the quadrupole mass spectrometer. The quadrupole MS records an initial helium current I^0_{He} inside the MC, which represents how large the he-

lium flux into the MC is. Afterwards the evaporation cell temperature T_{EC} is increased and the reduction of I^0_{He} to I^1_{He} is recorded ($I^1_{He} < I^0_{He}$). The extinction ($0 \leq \alpha \leq 1$) of the helium droplet is defined by the ratio between I^1_{He} and I^0_{He} ($\alpha = 1 - I^1_{He}/I^0_{He}$, this definition is taken from Volk *et. al.* [66]). The evaporation cell temperature T_{metal} has to be rather large in order to obtain a large enough α. Typical values for gold at $T_{CH} = 5.4$ K are:

1. $\alpha = 0.25$ at $T_{Au} = 1450°C$
2. $\alpha = 0.75$ at $T_{Au} = 1560°C$
3. $\alpha = 0.90$ at $T_{Au} = 1600°C$

The nanowire structure strongly depends on α. For very large $\alpha(\approx 0.9)$ the helium droplet shrinks, which forces the wire to grow more in thickness, as the available droplet volume is only 10% of its initial value. The smaller α becomes also the larger structures are obtained. However, for very small extinction rates ($\alpha \leq 0.25\%$), the risk of multicenter aggregation increases. Optimal sizes with a very small fragmentation of the wire due to multicenter aggregation is found for $\alpha = 0.75$. However, these values should only be seen as a rule of thumb, because a detailed study of the nanowire structure versus several extinction rates would require a rather large study of TEM observations.

After choosing an extinction rate, the deposition rate $\dot{m}$ at the micro balance has to be determined. The resolution in mass deposition is limited by the apparatus accuracy of the micro balance $\Delta m_{min} = 10^{-3}\mu g/cm^2$. As a result, the smallest possible deposition rate $\dot{m}_{min}$ is between high 10^{-6} and small $10^{-5}\mu g/cm^2 s$. For large nanowires the mass deposition rate $\dot{m}$ is usually within the range of $1..10 \cdot 10^{-4}\mu g/cm^2 s$. However, smaller structures achieve a very small deposition rate of only a few $10^{-5}\mu g/cm^2 s$, close to the resolution of the micro balance. From the deposition rate on the micro balance it is possible to approximate the coverage on a TEM grid, after a deposition time $\tau_{deposition}$. TEM observations have shown, that a total deposited mass $m_{deposition}$ in the the order of a few $10^{-2}\mu g/cm^2$ is ideal, as wires are easy detectable (no large empty spaces in between the single wires), but the coverage is not so large, that an overlap of the nanowires is likely/detectable. The coverage of TEM grids is discussed in more detail within the following section(s).

A typical measurement of the deposition rate with simultaneously recording the helium signal I_{He} is drawn in Figure 4.5. The decrease in the amount of helium reaching the MC, represented via the extinction factor α, can be directly linked to an increase of the mass deposition rate $\dot{m}$. After decreasing the evaporation cell temperature again, the helium signal reaches again I^0_{He} and the deposition rate diminishes.

After the desired settings have been chosen, the micro balance is removed out of the helium beam and the TEM grid can be placed into the helium beam for a predetermined deposition time $\tau_{deposition}$ via the manipulator. During $\tau_{deposition}$ the mass deposition rate

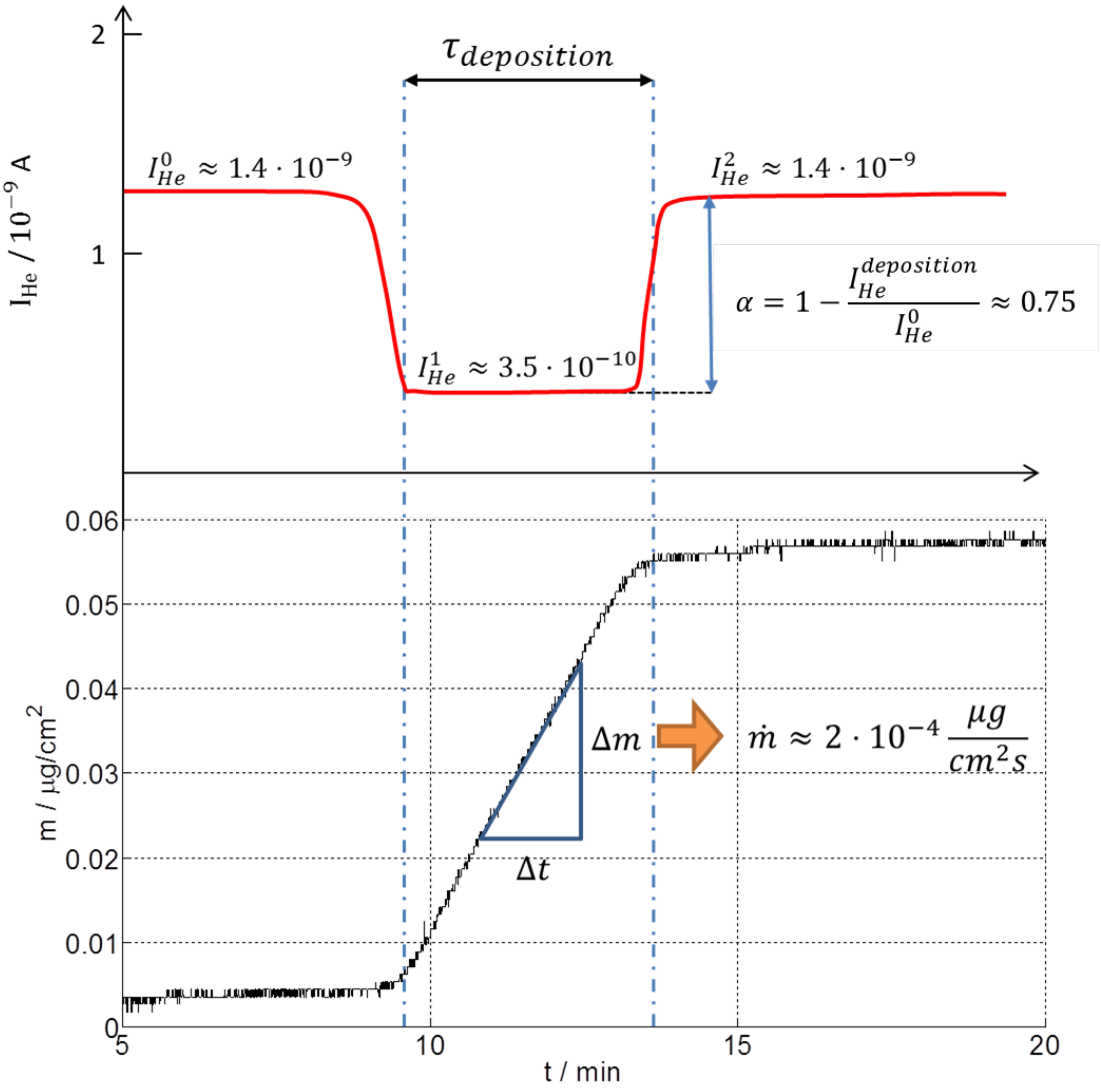

Figure 4.5: Deposition experiment of Au nanowires. The original amount of helium is recorded via the quadrupole mass spectrometer in form of a partial pressure current I_{He}^0. When increasing the evaporation cell temperature T_{Au} the helium signal decreases to I_{He}^1 as well as the mass deposition rate $\dot{m}$ increases.

$\dot{m}$ is kept constant, which is indirectly monitored via the helium partial pressure I_{He}, recorded by the quadrupole mass spectrometer, as the helium beam hits the TEM grid instead of the micro balance.

4.2.1 Deposition under Cryogenic Conditions

As already mentioned previously not all metallic nanowires are stable at room temperature (e.g. silver). The helium droplet provides an ideal ultracold environment for the synthesis of nanowires inside the helium droplet. However, when the nanowires are deposited on a substrate, they are heated up to the substrates temperature, so structures which are stable at $T_{He,liq} \approx 0.4$ K might not be detectable at the substrates/room temperature, as surface diffusion processes can begin to start at lower temperatures. In order to investigate less temperature stable elements the TEM grid has to be cooled to enable less 'hot' landing conditions.

This task is realized when cooling the TEM grids with liquid nitrogen down to substrates temperatures of $-150°C$ (due to heat losses the temperature can not reach $T_{N_2,liq}$). Liquid nitrogen is filled into a reservoir, which is connected to the manipulator. Liquid nitrogen can then fill up the interior of the manipulator down to the grid holder plate.

After deposition on the grids and venting the chamber with dry nitrogen the sample holder is removed from the grid and immediately (room temperature exposure is kept below 5 s) placed into an external dewar containing liquid nitrogen. The grids are then removed from the sample holder and are transferred to the electron microscope. A special cryo TEM holder is used, which is again cooled with liquid nitrogen to enable an *in-situ* observation of the cooled substrate. The holder is then placed into the microscope, and during the start up of the TEM, the holder is kept at $T_{N_2,liq}$. After the TEM is fully operational and points of interest on the grid are located, the liquid nitrogen of the TEM holder is no longer refilled, so the amount of liquid nitrogen inside the holder decreases. As a result the substrate heats up gently ($\approx 3-4$ h heatup time) and possible surface diffusion processes can be observed. A minor drawback to measurements with heating chips is that the temperature at a cryogenic experiment can not be kept constant, which limits the observation time of surface diffusion processes.

As this experiment needs a lot of practice/routine and several steps have to be performed, a detailed step-by-step description how to perform a cryogenic experiment with this holder is described in the appendix section 8.2.

4.3 Investigation of Surface Diffusion Processes

After the desired nanowires are deposited on a TEM substrate, the grid(s) are removed from the sample holder and transferred either in an intermediate vacuum environment of $\approx 10^{-2}$ mbar or within a dewar containing $N_{2,liq}$ mbar, if cryogenic experiments are to be performed.

The desired grid is then placed onto a TEM grid holder, suited for the desired type of observation and afterwards transferred into the microscope vacuum. It is important

to mention, that within electron microscopes the vacuum pressure is orders of magnitudes higher than inside the main chamber. This is crucial to know, because it is not possible to prohibit oxidation processes during the observation time. A detailed study how oxidation can occur during the observation process and how this affects physical phenomena and processes (e.g. alloying processes) is described within the master thesis of Maximilian Lasserus [36].

After placing the grid into the observation region within the TEM, the sample is analysed and within the observation time, the temperature is increased, either by heating up the heatable grid or watching the grid heat up from liquid nitrogen temperature. In both cases it is crucial that the temperature ramp is set to be small enough, so that the temperature does not significantly rise when scanning the sample.

The scanning time is in most cases the limiting parameter when observing large amount of surface diffusion processes. In principle the FEI Titan3 has a very high resolution of 70 pm, but when trying to observe multiple surface diffusion processes at one time, which requires a large observation area, a lower resolution has to be chosen in order to scan over the desired region in an adequate time. As a consequence, if more surface diffusion events need to be observed, the resolution has to be reduced. For a scan over one mega pixel a scanning time of approximately half a minute is required.

Not only scanning time is a limiting parameter of the resolution, but also the effect of the electron bombardment on the sample. As the electron flux per time increases, if a longer scanning time is chosen, carbohydrates are created at the observed region. The created carbohydrates can then manipulate surface migration processes if they get adsorbed by the clusters. In Figure 4.6 the effect of a beam damage is visible in the marked area which was previously scanned.

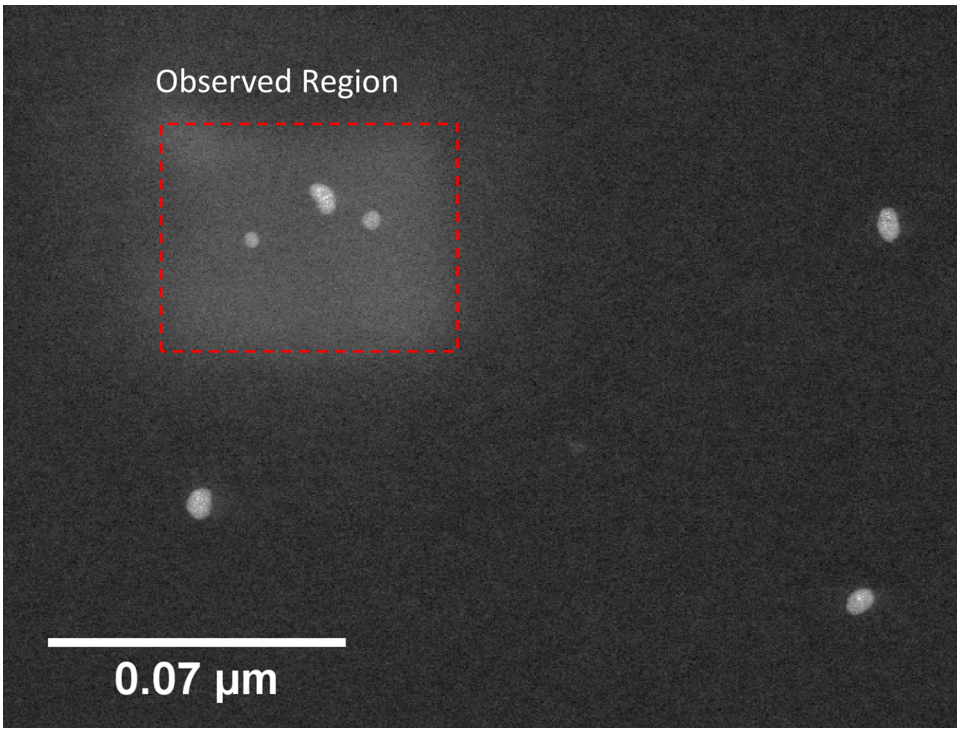

Figure 4.6: Beam damage in the observed region (see square with different level of contrast). The damage is caused by the creation of carbohydrates during the scanning time.

In summary it is important to find a good trade-off between resolution on the one hand and scanning time and possible beam damages on the other hand in order to study the very nature of surface diffusion processes.

Chapter 5

Electron Microscopy Study and Observation of Thermally Induced Surface Diffusion

In this chapter the time-resolved, high resolution electron microscopy observations of the degradation of monometallic nanowires is presented. An experimental study of thermally induced surface diffusion processes, which result in so-called Rayleigh breakups is carried out. In the next chapter the experimental efforts are then combined with a cellular automaton to simulate the observed surface diffusions.

This chapter corresponds to the experimental part of the publication:

Martin Schnedlitz, Maximilian Lasserus, Daniel Knez, Andreas W. Hauser, Ferdinand Hofer and Wolfgang E. Ernst. Thermally induced breakup of metallic nanowires: Experiment and theory. *Phys. Chem. Chem. Phys.*, 2017.

5.1 Structure and Covering Rate of Synthesized Nanowires

He_N droplets are used to create monometallic nanowires with diameters below 10 nm and lengths of several 100 nm. Very large droplets with over one billion helium atoms ($T_{CH} = 5.4$ K) are used to enable the growth of very large structures. The growth of nanowires inside the helium droplet is independent of the dopant material, due to the same attractive force exhibited by the quantized vortices of superfluid helium. However, after deposition material characteristics, such as the thermal stability or the likelihood of oxidation determine their shape and structure. Four different materials of nanowires are illustrated in Figure 5.1.

All four nanowires are synthesized at $T_{CH} = 5.4$ K, with an extinction rate $\alpha = 0.75$ and are analysed at room temperature within the TEM. The main difference is clearly visible, as silver and also copper nanowires are not stable at room temperature and surface diffusion leads to a fragmentation of the nanowires. The original nanowire structure of

silver can still be recognised as the patternized clusters are located close to other spherical clusters along curved lines and those arrays of spherical clusters are separated from other arrays. This indicates, that the original nanowires have already undergone structural changes for long enough time to fully patternize as a result of a thermally induced surface diffusion process. Highly interesting are copper nanowires, as the original form is nearly fully conserved at room temperature and only breakups at constriction points are visible. This phenomenon is due to the formation of an oxide layer, which causes a stabilizing effect and prevents further surface diffusion processes. This phenomenon and the effect of oxidization on Rayleigh breakups is studied in greater detail within the next few sections.

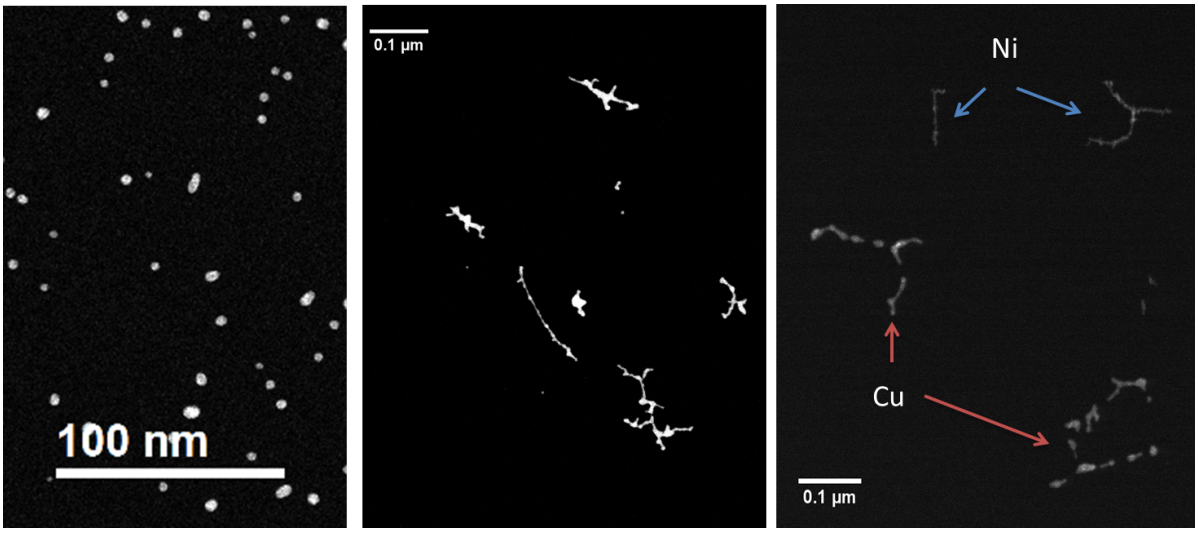

Figure 5.1: Four different nanowire materials studied at room temperature. All of them are synthesized at $T_{CH} = 5.4$ K and with $\alpha = 0.75$. In the left figure the thermally very unstable silver nanowires are already fully patternized, as a result of a very low energy barrier towards starting the surface diffusion process. In the central figure the noble metal gold is illustrated. Gold is not only stable at room temperature, but it also shows no or nearly no oxidation at its surface. As a result gold is an ideal candidate to study the unperturbed phenomenon of surface diffusion. The non-noble metals nickel and copper are presented in the right figure. Both of them are covered with an oxide layer, which effectively stabilizes the synthesized nanowires.

5.1.1 Coverage Rate

As mentioned before not only the size of the droplet limits the size of the nanowires, but also the pickup rate, regulated via T_{EC}, determines the structure and size of the nanowires. The amount of wires deposited on a grid is estimated via the mass deposition rate, measured by the micro balance. The challenge is finding a good trade-off between a high enough density of nanowires and a low chance of an overlap of single wires.

Figure 5.2: STEM-HAADF image of the covering rate of gold nanowires on an amorphous carbon grid. The nanowires are synthesized at $T_{CH} = 5.4\ K$ with three different $\alpha = \{0.75,0.25,0.1\}$. A total mass of $m = 0.8 \cdot 10^{-2}\ \frac{\mu g}{cm^2}$ is deposited on the TEM substrate, resulting in a coverage of roughly 0.8%.

A typical example for a mass deposition of gold nanowires on a carbon grid is demonstrated in Figure 5.2. The total amount of deposited mass on this substrate is $m = 0.8 \cdot 10^{-2}\ \frac{\mu g}{cm^2}$. It is important to mention at this point, that the coverage is not homogeneous. The TEM grid contains a denser centre, which corresponds to the centre of the helium beam path and a decreasing coverage rate for regions away from the beam centre. From Figure 5.2 a coverage rate of 0.84% is measured. This coverage is however not con-

stant when heating the TEM grid, as the patternization process leads to more spherical structures, which result in a smaller total coverage of the grid, i.e. for $T_{Au} = 250°C$ a coverage rate of only 0.53% is measured.

5.1.2 Extinction Rate and Size Distribution

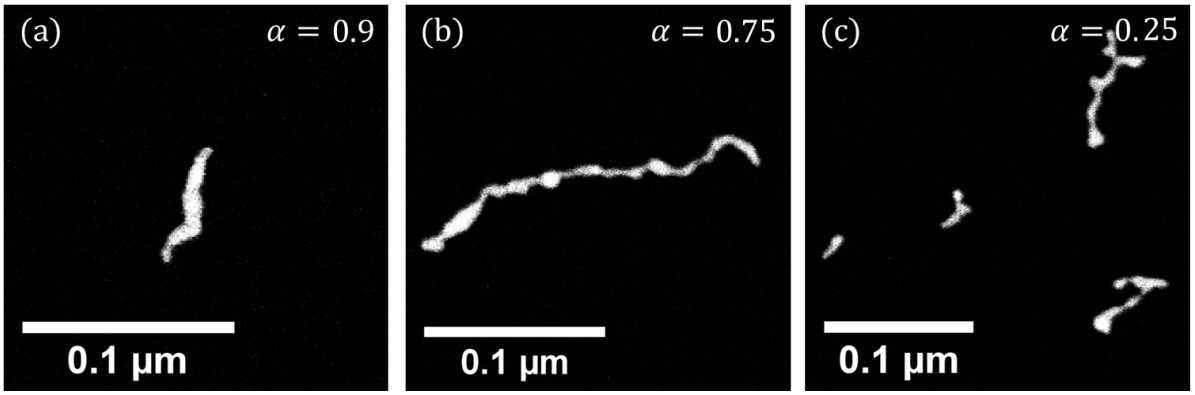

Figure 5.3: STEM-HAADF images of gold nanowires on an amorphous carbon grid, with three different extinction rates $\alpha = \{0.9, 0.75, 0.25\}$.

The extinction rate determines on the one hand side how many atoms are picked up and on the other hand how large the remaining droplet is. Hauser *et. al.* [22] described the collision time and the time to form clusters inside helium droplets via density functional theory. Within this model two input data are accounted for, the doping frequency with neutral atoms and the collisional cross section of two dopant atoms, which further decrease the size of the droplet. A more sophisticated model was developed by Thaler [55], where he described a size dependent nucleation time as a function of particles of the size n. It was found that the time required for particles of the size n to find each other can be written as [55]

$$t_{dimerization} \sim v_0\sqrt{n}. \tag{5.1}$$

In this equation v_0 represents the starting velocity and n the size of the particles. The DFT calculations from Hauser *et. al.* [22] have shown that the mass effect of larger particles lead to longer nucleation times as their velocity is smaller and therefore also the time increases to nucleate with another particle. As a result lower doping rates lead to longer nucleation times, as the droplet remains larger and in addition fewer particles can agglomerate. This may result in multiple cluster synthesis within one droplet which is illustrated in Figure 5.3 (c). The wires synthesized with smaller α tend to be shorter and more numerous than wires synthesized with higher α. However if α is very large, the droplet size becomes smaller than the maximum possible wire length, which leads to the formation of shorter, but thicker nanowires (see Figure 5.3 (a)).

The length distribution obtained from gold nanowires (data from Figure 5.1 and other

wires deposited on the same substrate) is drawn in form of a histogram below. The average length is located at around 60 nm, but also a large number of wires is limited in size, due to the formation with either too large or too small extinction rates.

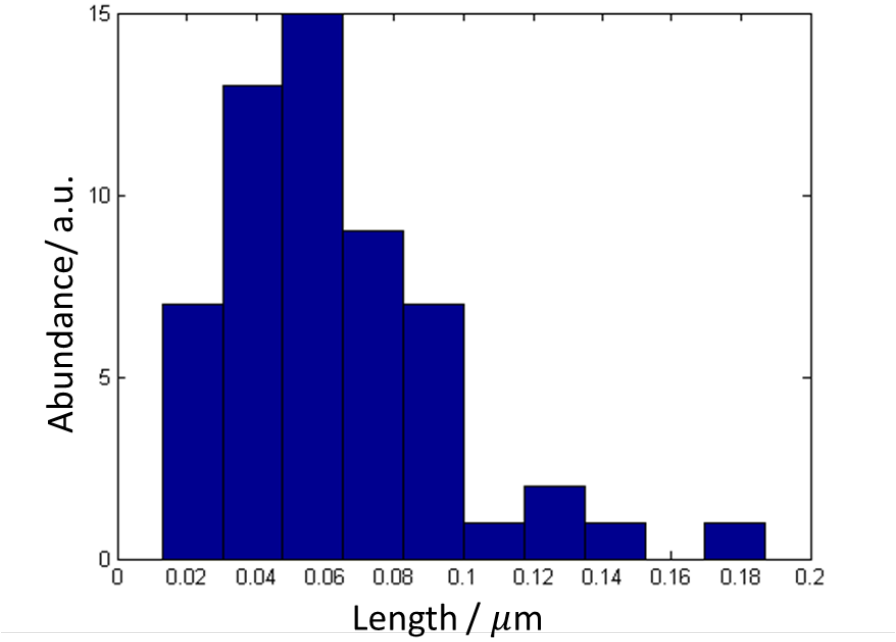

Figure 5.4: Histogram of gold nanowire length, obtained via the analysis of nanowire length from Figure 5.1 and other wires deposited on different locations of the same grid.

5.2 Thermally induced Surface Diffusion

After the nanowire preparation via the helium droplet technique, it is possible to perform *in-situ* observations of the very nature of this thermally induced breakup for wire diameters as small as 1 nm and covering a total observation area of $(3\ \mu\text{m})^2$.

Throughout all studies of thermally induced surface diffusion processes, the substrates temperature is increased gently with $dT/dt = 2\ K/\text{min}$. Using such a slow increase in temperature, it is possible to determine the breakup temperature, which is required for a specific structure. As surface diffusion is not only a matter of temperature, but also a function of time at constant temperature (see chapter 6 for more details), corresponding observations were necessary. In the following Figure 5.5, the surface diffusion process of a gold nanowire is presented and studied as a function of time and temperature. The corresponding temperature ramp is also presented in Figure 5.6. Note that the temperature is kept constant at $150°C$ for 45 min, in order to study the influence of time on the diffusion process.

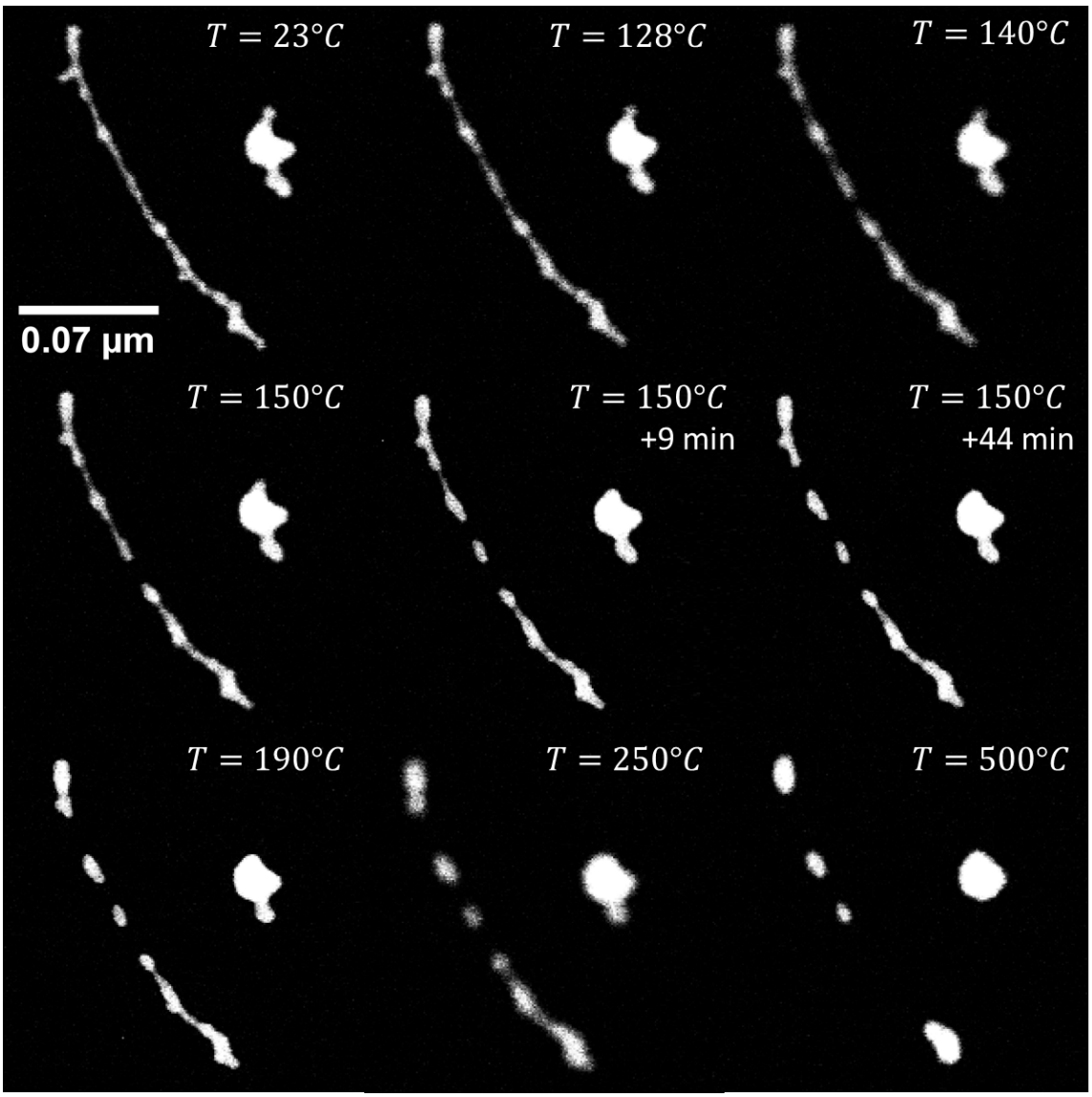

Figure 5.5: Surface diffusion process of a gold nanowire. The temperature is increased with 2 K/min and is kept constant at 150°C for 45 min. After this intermezzo the temperature is increased again with 2 K/min up to 200°C. Finally the structure is analysed at temperatures of 250°C, 300°C and 500°C (temperature ramp is illustrated in Figure 5.6). One can see, the phenomenon of smoothing during the first 100°C and a migration of material outwards of constricted points. The first breakup event occurs at 140°C and two more are visible at 150°C. There are indeed breakup events at constant temperature, however after 15 min observation time, the structure only changed marginally. For very high temperatures, the segments converge towards a spherical structure.

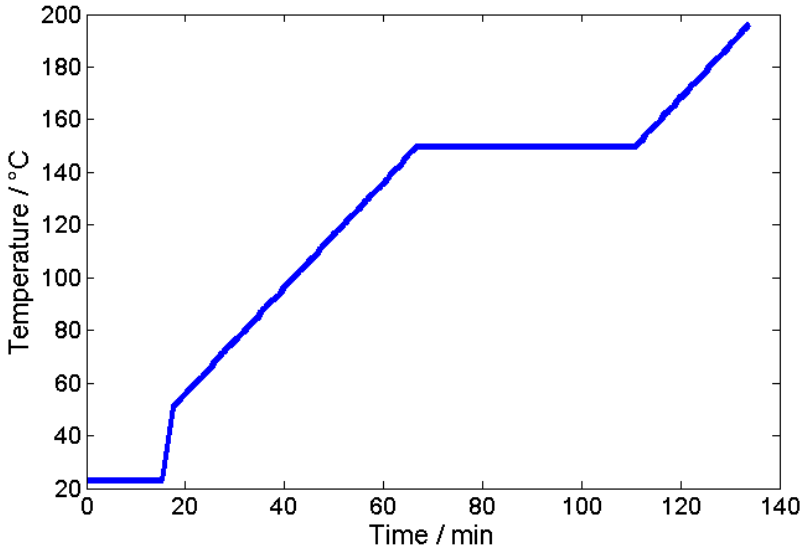

Figure 5.6: TEM Grid temperature as a function of time, for the observation of gold nanowires (see Fig5.5). The temperature is increased with a constant rate of 2 K/min and kept constant for 45 min at 150°C.

The observed surface diffusion processes, for metallic nanowires show in general the same behaviour as illustrated for the one example, represented in Figure 5.5:

1. With increasing temperature a 'smoothing' of the initial configuration sets in, in order to reduce the amount of atoms which are sitting on the surface.

2. A mass transfer process from initially constricted points starts, leading to a thinning of the wire at these spots.

3. When further increasing the temperature, the first break-up events occur. It is found, that thicker constriction points need a higher temperature to breakup.

4. After all initially constricted points are broken up, the shape of the remaining patterns converge towards a spherical structure. This situation represents a local energetic minimum, as the wire patternizes, instead of forming one sphere.

The effect of time on the surface diffusion is rather difficult to investigate, due to the small temperature window, were surface diffusion sets in. Particles need to overcome an energy barrier to detach from the rest of the wire in order to start migrating. The likelihood of detaching can be approximated via equations used in chemistry which describe the detaching rate k as a function of the energy (see chapter 6 for more details):

$$k \sim \exp(-E_{\text{barrier}}/k_B T), \tag{5.2}$$

with E_{barrier} being the energy barrier, which has to be overcome in order to detach from the rest of the wire, T the applied temperature and k the detaching rate. As a result of

this relation, a slight increase in temperature can have a large impact on the migration velocity. This is in good agreement with the rare findings of breakup events over time at constant temperature. A comparison between the observed breakup temperature as a function of the initial wire constriction points diameter d_{nw} is plotted below, to study the effect of an increasing temperature on the surface diffusion.

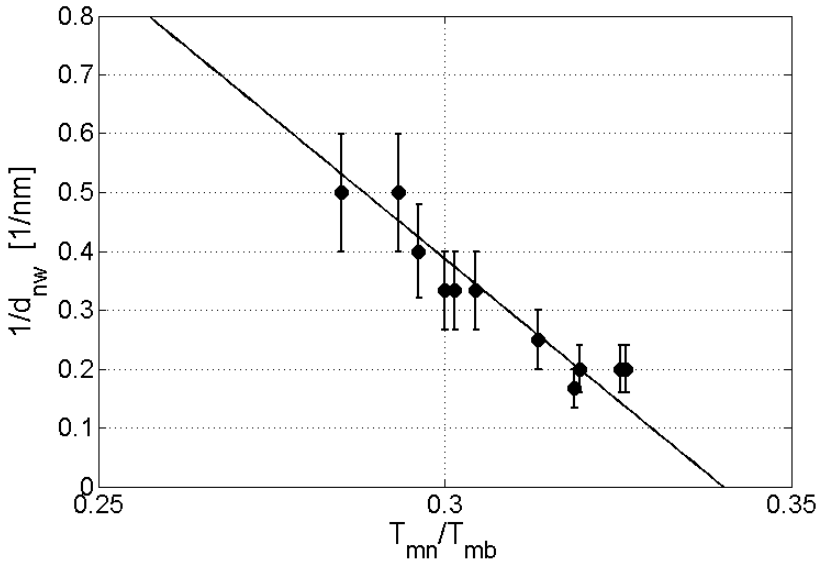

Figure 5.7: Inverse breakup diameter as a function of temperature in relation to the bulk melting temperature for gold nanowires. A linear fit is performed to guide the eye and the error bars are a result of the limited resolution of the TEM.

Particularly interesting is the finding that the breakup temperatures are far below the corresponding bulk melting temperatures, as represented in Figure 5.7. This is a direct result of the surface size effect of nano structures, which causes a reduced breakup temperature in comparison to the bulk melting temperature. This interesting behaviour motivated Volk *etal.* [65] to design a new experiment in order to investigate less temperature stable elements. This special cryo experiment showed that breakup events for silver nanowires start at temperatures as low as $\approx 258\ K$(-15 °C) [65].

5.3 Material Trends

Within this thesis, a large variety of metals are analysed with respect to different diameters of the initially stable nanowires in order to give a more general insight into the phenomenon of surface diffusion. A comparison between different materials used within this thesis is presented below in Figure 5.8. As non-noble metals and noble metals tend to oxidise, their diffusion process can be blocked by a covering oxide layer. Especially interesting are copper nanowires, as they tend to be not stable at room temperature, but the contact with oxygen inside the vaccum chamber prevents the wires from further

break ups or a complete patternization. This can be seen by the initial configuration of copper nanowires, which already show breakup points at room temperature. Further breakups occur later at higher temperatures, when the oxidized particles start to diffuse.

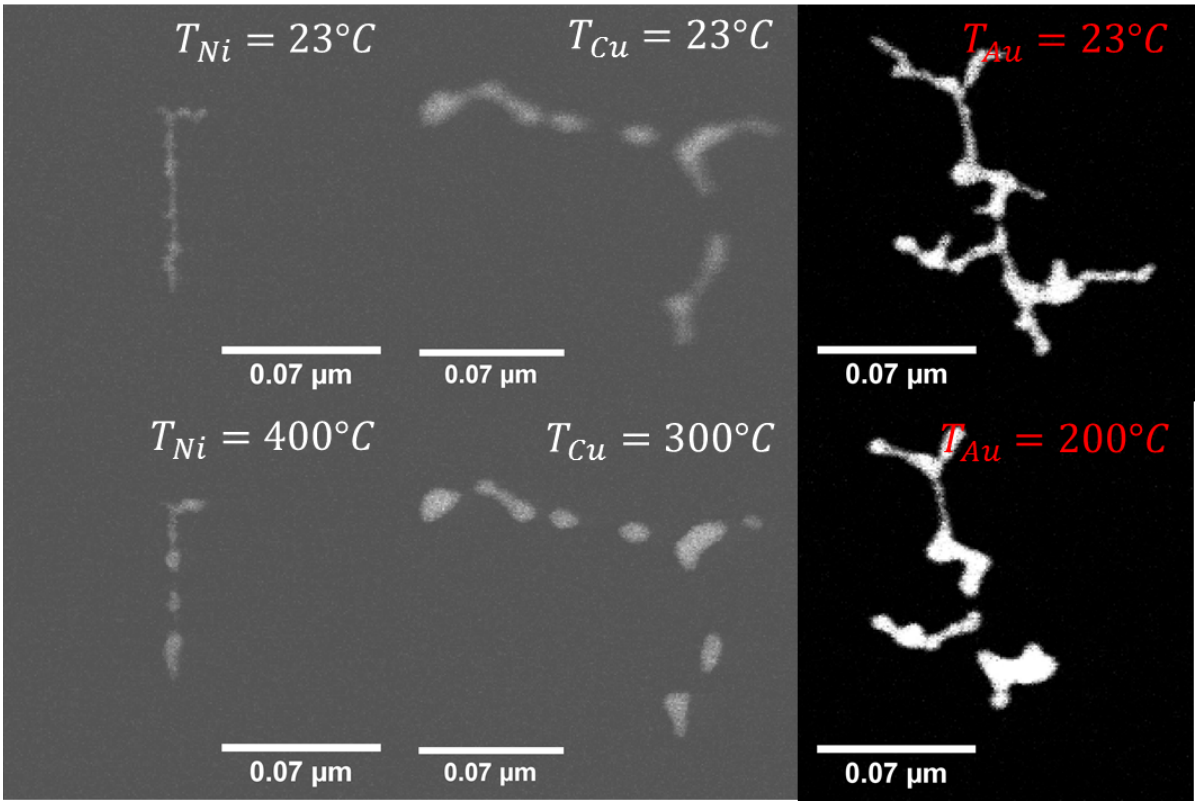

Figure 5.8: Breakup of nanowires of different materials. The two images on the left showing the nickel nanowires, which required a rather high temperature to break up. A large binding energy of nickel atoms ($E_{bond} = 428$ kJ/mol), combined with a small bond length ($d_{bond} = 0.125$ nm) and a oxidization layer increased the stability. The two central images show the extraordinary behaviour of copper, where an oxide layer stopped the initial wire from further breaking up, as copper nanowires are not stable at room temperature. On the right, the results for the noble metal gold are presented. Here not only breakup events are visible, but also a reduction of energetically not preferred 'tentacles' is visible.

The measurements confirmed the known relation between the breakup temperature of nanowires and their corresponding bulk melting temperature given by [31], which is derived, when comparing the amount of surface atoms to the total number of atoms in a cluster.

$$T_{mn} = T_{mb} \cdot \left(1 - \frac{\mathrm{C}}{d_{nw}}\right), \tag{5.3}$$

where T_{mn} is the observed breakup temperature for our nanowires, T_{mb} is the melting temperature of the corresponding bulk, d_{nw} is the diameter of the initial configuration and C is a material specific constant. By fitting the experimental data with this relation, the material trends for the breakup of nano-wires as illustrated in Figure 5.9 are obtained. The ratio T_{mn}/T_{mb} clearly shows the expected linear behaviour as a function of the inverse diameter $1/d_{nw}$. However, larger deviations from the experimental data points are evident for Cu and for Ni. This is a consequence of the specimen exposure to ambient air. Although air contact is kept short, oxidation of Cu and Ni wires cannot be fully avoided. The degree of oxidation can be visualized with EELS measurements as shown in Figure 5.10, which compares the TEM image for Cu and Ni nanowires with images from the element-wise analysis of copper, nickel and oxygen. In both cases an oxygen shell is clearly visible. For Au and Ag wires, on the other hand, no significant oxidation is observed. As a result, their behaviour is well captured by equation 5.3.

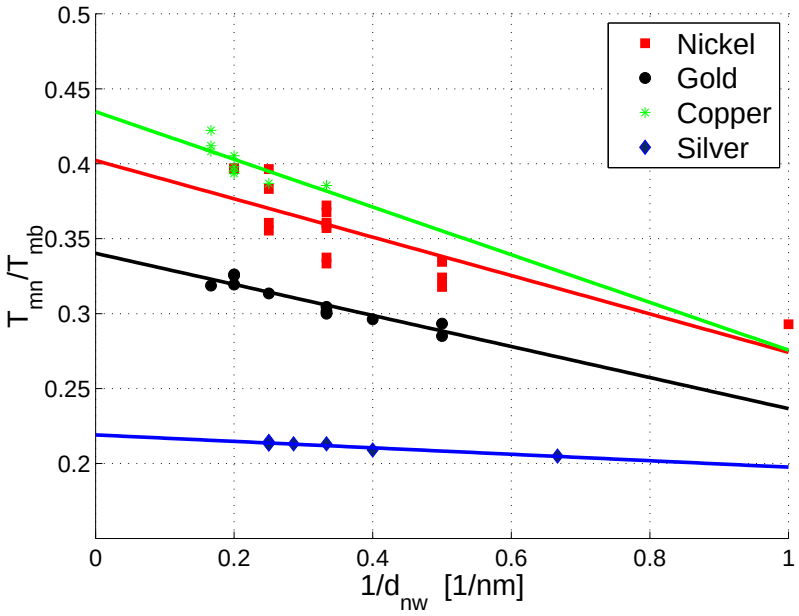

Figure 5.9: Combined results for monometalic nanowires of Nickel (red),Copper(green),Gold(black) and Silver(blue) at the break up point for different temperatures T_{mn} in relation to the corresponding bulk melting temperatures T_{mb} for different diameter d_{nw}

When heating above the breakup-temperature, a fragmentation takes place as it is predicted by the CA simulation. The resulting nanostructures show elliptical or spherical shapes. Details of this process and a comparison with a cellular automaton are given below.

5.3.1 Oxidation

To determine a material trend of the breakup of nanowires the diameter dependent breakup temperature T_{mn} is measured and fitted according to equation 5.3. Good agreement between the cellular automaton simulation and the observed surface diffusion process is obtained when dealing with noble metals like Au and Ag (see chapter 6) .

For the non-noble metals like Ni and Cu an oxide layer covering the metal cluster is observed (see Figure 5.10) which results in a higher breakup temperature as the oxide has to evaporate before the diffusion process can continue. As a result, larger deviations from the linear behaviour are observed.

The particularly interesting behaviour of copper can be fully understood, when taking a look at the EELS signal for copper and oxygen, which indicate that a covering oxygen layer prevents the material from further diffusion.

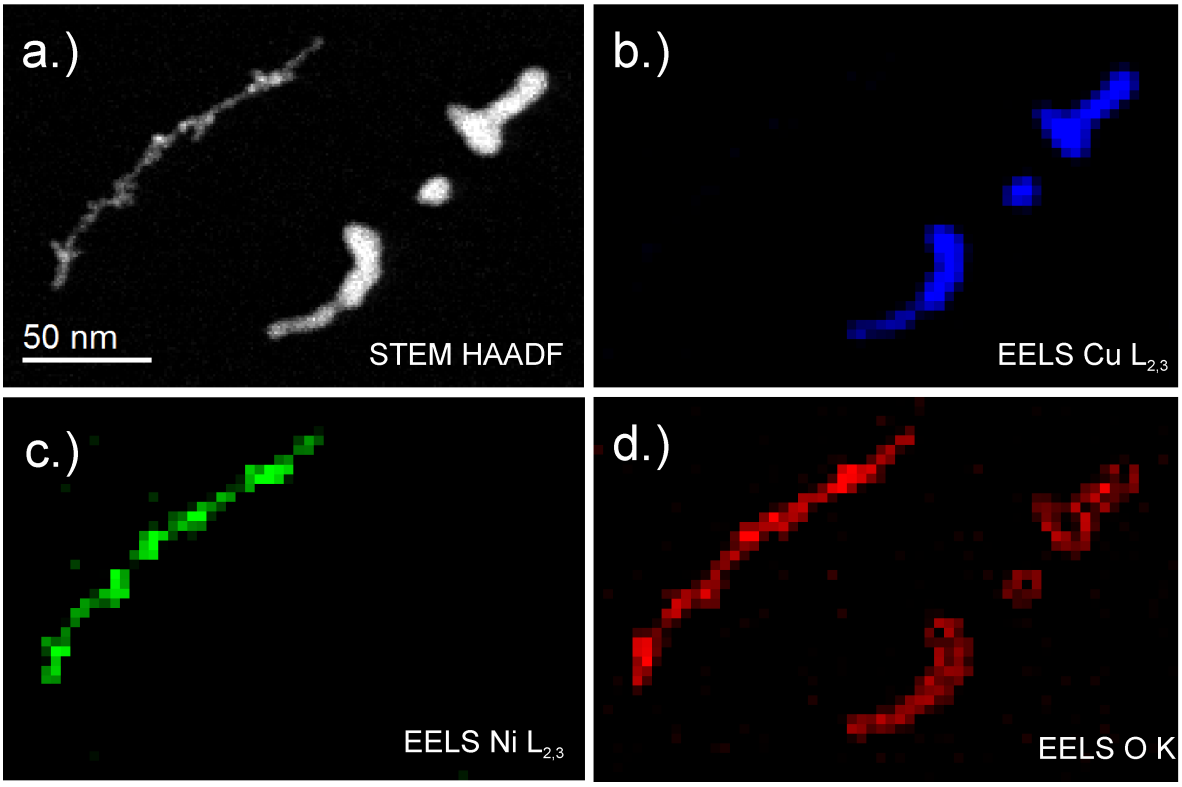

Figure 5.10: EELS elemental maps for Cu and Ni nano structures. (a) shows the STEM HAADF image. The other three pictures are EELS signals for Copper (b), Nickel (c) and for Oxygen(d). A contamination with oxygen on the surface of non noble metals is clearly visible. As a result the breakup temperature was increased since the oxide layer suppressed the surface diffusion for temperatures below the melting point of the metal oxide.

Chapter 6

Cellular Automaton Simulation

A cellular automaton is developed to combine the experimental efforts from the previous chapter with simulations based on a novel model, capable of the prediction the very nature of this thermally induced surface diffusion processes. Within this chapter the physical principles and the main algorithm behind the cellular automaton (CA) as well as comparisons with the experimental observations are presented.

This chapter corresponds in one part to the theoretical section of the publication:

Martin Schnedlitz, Maximilian Lasserus, Daniel Knez, Andreas W. Hauser, Ferdinand Hofer and Wolfgang E. Ernst. Thermally induced breakup of metallic nanowires: Experiment and theory. *Phys. Chem. Chem. Phys.*, 2017.

In another part, this chapter corresponds to the publication:

Andreas W. Hauser, Martin Schnedlitz, and Wolfgang E. Ernst. A coarse-grained Monte Carlo approach to diffusion processes in metallic nanoparticles. *EPJ*, accepted.

6.1 Introduction

In this chapter a new apporach towards the simulation of diffusion behaviour for metallic nanoparticles with diameters in the range of a few nanometers, aiming at finite many-particle systems consisting of several thousands of metal atoms is presented. Special focus will be set on wire-shaped nanostructures due to their potential applications in circuits or nanodevices[28, 54], as membranes[33], biosensors[1, 7, 69], transparent electrodes[49], waveguides [73] or antennae in photochemistry[52].

Regarding the shape and structure of metallic nanoparticles, modern imaging techniques of electron microscopy yielded significant advances in the experimental study of these transitions with particle size effects[21], and opened the possibility for the in-situ analysis of structural changes caused by chemical interactions or temperature-mediated diffusion processes[65]. A detailed understanding of the dynamic behavior in these systems requires a multi-scale approach towards material simulation which ideally covers the whole range from the macroscopic to the atomic scale, with the latter often being dominated

by less-intuitive quantum effects. Therefore, numerous methods and program packages have been developed, each of them filling a certain niche in the broad spectrum of computational materials research and design. Particularly interesting with respect to multiscale approaches is the MBN Explorer suite of programs[50] which offers the ability to group atoms into larger units in order to reduce the computational effort in molecular dynamics or Monte Carlo simulations.

The model presented is based on the concept of a cellular automaton (CA), a well-studied discrete model of computability theory with broad applications ranging from physics to economy[71]. The basic principle, originally conceived by Ulam and von Neumann[61, 68], and introduced to a broader audience by Conway in the form of a zero-player game called 'Game of Life'[15], is a discretisation of the environment in the form of cells. The status of each cell is periodically updated based only on the status of its neighbour cells. This principle has been adapted and implemented here to describe the diffusion of metal atoms on the surface of metallic nanoparticles residing on a carbon substrate. Instead of describing the motion of each atom separately, which introduces clear limitations to the number of particles involved in standard molecular dynamics simulations, a coarse-grained model is employed which handles material transfer in larger groups of atoms, defined by the grid size of the CA. This reduces, together with the intrinsic limitation to interactions with next-neighbor cells, the computational effort significantly, and allows the simulation of temperature-induced effects such as droplet formation, surface tension and Rayleigh-breakup for even nanometre-sized structures. In comparison to the comprehensive MBN package this method can be considered as a 'top-down' approach in the sense of accessing nanostructures from the macroscopic side based on microscopy image data, while the comparable stochastic Monte-Carlo based algorithms of the MBN package are starting at the atomic scale but employ a grouping of atoms into clusters in order to address larger systems.

The basic principle and implementation of our method is presented in the next section. In Section 6.3 the model is then used to study surface diffusion processes of Ni, Pd and Au nanoparticles and nanowires on amorphous carbon. The predictions are compared with recent experimental findings of our group obtained by temperature-programmed TEM imaging, which has been presented within the previous chapter 5.

Section 6.4 introduces interactions with the support and aims at a correct description of wire deformation by surface wetting effects. The latter occur after the deposition of inert wires on TEM grids of amorphous carbon. An attempt is made to reconstruct the actual shapes from two-dimensional TEM images and compare them to the model predictions.

6.2 Computational Details

Surface diffusion processes can be seen as paradigmatic cases of multi-scale dynamics. Although atomic in essence, an atomistic approximation is rarely used to describe this group of phenomena due to their macroscopic character, which only emerges for sufficiently large system sizes and longer time evolutions. Typical examples are surface wetting, the intermixing of liquids, capillarity, Ostwald ripening or Rayleigh breakup. On the large scale, these phenomena are well described by continuous models such as surface tension or Fick's law of diffusion, but a fully macroscopic view has its clear limitations. For example, in the case of solid-liquid phase transitions for metals, the concrete behaviour of an arbitrarily shaped, solid object as a function of temperature can only be captured by a spatial discretisation in combination with a set of assumptions on local diffusion based on the shape of the material at a given point in time and space.

6.2.1 Comparison with other Methods

In some cases, models of reduced dimensionality are able to deliver very accurate results, as has been shown in the case of silver cluster fractals on graphite. Experimental studies revealed that silver clusters on graphite arrange themselves in dendritic structures[5, 35]. This behavior could be well described by a two-dimensional Kinetic Monte Carlo model[10, 50] based on the diffusion limited aggregation method[53].

Another interesting attempt to reduce the complexity of the problem has been published in Ref. [58]. It is based on Mullin's equation[44], originally introduced to simulate the thermal grooving at metallic grain boundaries. It relates the flux of surface atoms to the gradient of the local surface curvature, and derives an artificial force on the respective surface element. This is achieved by a discretisation of the contourlines of the actual structure, followed by a propagation in time based on Mullin's equation. Surface diffusion is assumed to be the main form of mass transport and dominating over evaporation-condensation processes. A partial differential equation of the form

$$\frac{\delta z}{\delta t} = B\frac{\delta^2 z}{\delta s^2}, \tag{6.1}$$

can be derived, with z denoting the local transversal displacement of a contour line s. A change of the local displacement in time t is assumed proportional to the inverse curvature of the contour line, $\delta^2 z/\delta s^2$. All unknown material-specific properties are adsorbed into a constant B, which had been set to one previous work from the Ernst group for the qualitative description of the degradation of the silver structures[65]. While the discretisation in s had been determined by the resolution of the TEM images, the discretisation in time was done in arbitrary units. Very fine steps had to be chosen to avoid instabilities in the propagation, which turned out to be only one of several downsides of the original implementation. Nevertheless, this ansatz has been successfully applied to the description of silver nanostructures despite its lack of computational practicality[65]. However, for the efficient description of larger and more complex structures a different

route has to be taken, preferably also bearing the potential to capture adsorption effects on different substrates. For this reason an alternative computational concept is employed: the direct simulation of material transfer via a cellular automaton (CA). As will be shown below, this model intrinsically accounts for the locality of the diffusion process via the limitation to interactions between nearest neighbour cells, which keeps the computational effort much lower than techniques based on contour lines.

6.2.2 Transformation of TEM Intensity into a Cell Representation

At first, the actual shape of the material, in our case metallic nanowires deposited on a weakly interacting substrate, needs to be translated into a pattern of cell occupation in a discretized environment (see Figure 6.1).

The two-dimensional information about the intensity given by the TEM images, is first translated into a two-dimensional matrix $\hat{D}$. The useful cell size is limited to the resolution of the transmission microscopy (TEM) images, in this case to pixels of $(0.95\ \mathrm{nm})^2$. $\hat{D}$ is then converted into a contour plot representation, which uses discretized steps of intensity I_n to represent different levels.

Following the fundamental principle of CA models the information given by $\hat{D}$ is converted into a 0-1 three-dimensional matrix $\hat{G}$, where each cell is either thought empty (0) or completely filled (1) with metal atoms. As a consequence, an ansatz for the translation from $\hat{D} \rightarrow \hat{G}$ has to be chosen.

First a central layer is created, using an initial threshold I_0, to separate data from noise. The next layers are created mirror-symmetrically above and below the central layer using a higher threshold I_n, where every layer above the previous layer uses an increased threshold ($I_n > I_m$ for $n > m$). The lack of topographical data in two-dimensional TEM images makes it necessary to introduce additional assumptions on the wire shape due to the loss of information in the projection. Assuming the height of the particles to be identical with the width, i.e. an approximately cylindric shape for wires and a spherical shape for particles, a three-dimensional structure can be derived from the pixel positions and intensities of the TEM image.

The main challenge however, is to convert the intensity data adequately into a three-dimensional representation. LeBeau *et. al.* [38] and Jones [29] have demonstrated that HAADF imaging can be used for quantification of the number and location of all atoms in a three-dimensional specimen. They found that the intensity provided by HAADF imaging increases linearly with the specimens thickness (see Figure 6.2) and therefore an intensity threshold for the nth layer within $\hat{G}$ is chosen to be

$$I_{\pm n} = n \cdot I_{Step} + I_0. \tag{6.2}$$

Using this information, the *algorithm* for the creation of a three-dimensional repre-

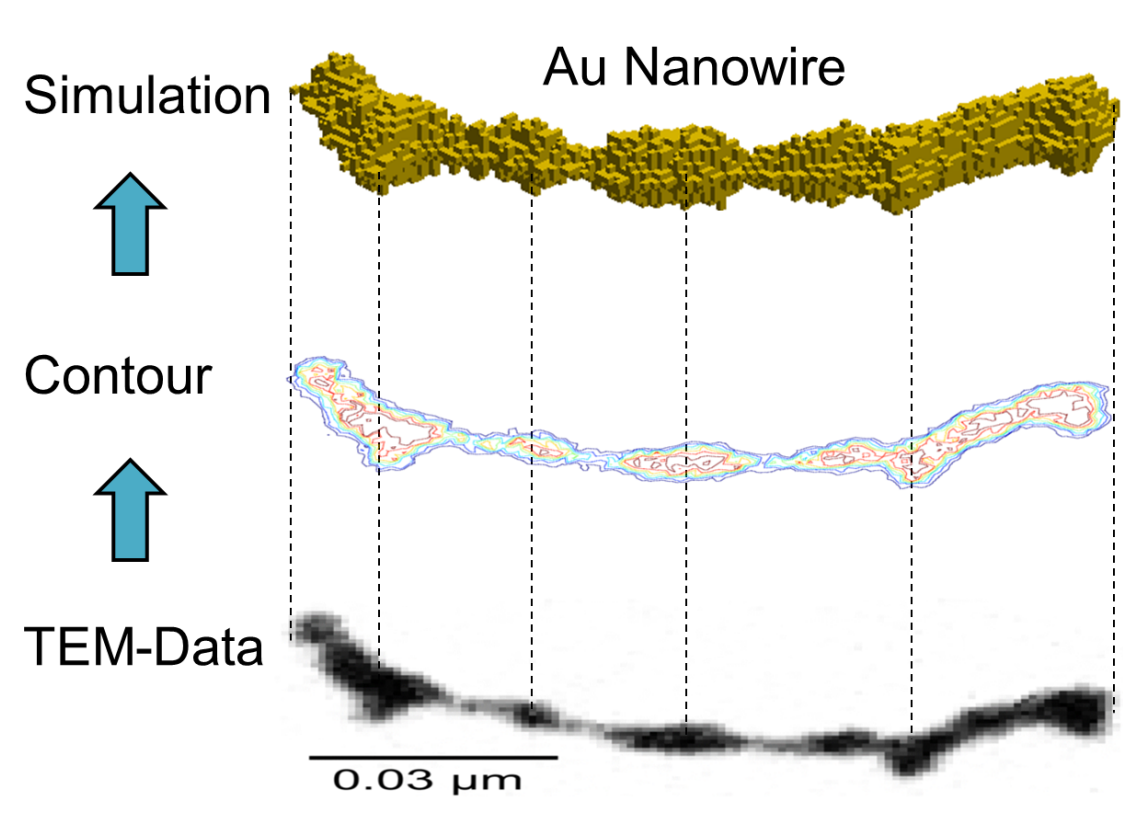

Figure 6.1: Schematic of the conversion from raw TEM data into a contour plot of the intensities, which are then used to create a three-dimensional representation of the nanowire in form of a cell occupation in a discrete environment (cell occupied = 1, cell unoccupied = 0). As TEM intensity information is provided in the form of a two-dimensional matrix, the wires are created layer by layer, starting with a lower threshold I_0 for the central layer, and counting only those pixels with intensities above I_0. For the next layers this threshold is continuously increased, which adds additional voxels above the starting layer and results in a three-dimensional reconstruction of the total structure.

sentation of the TEM data $\hat{G}$ is summarized within the listed *algorithm* 1. For simplifications the height is set to be the same size as the length and the width of the pixels, creating a voxel of $(0.95\ \text{nm})^3$, corresponding to approximately 55-85 metal atoms per cubic cell. The number of atoms per cell can be derived from the cell size and the ionic radius for a given element.

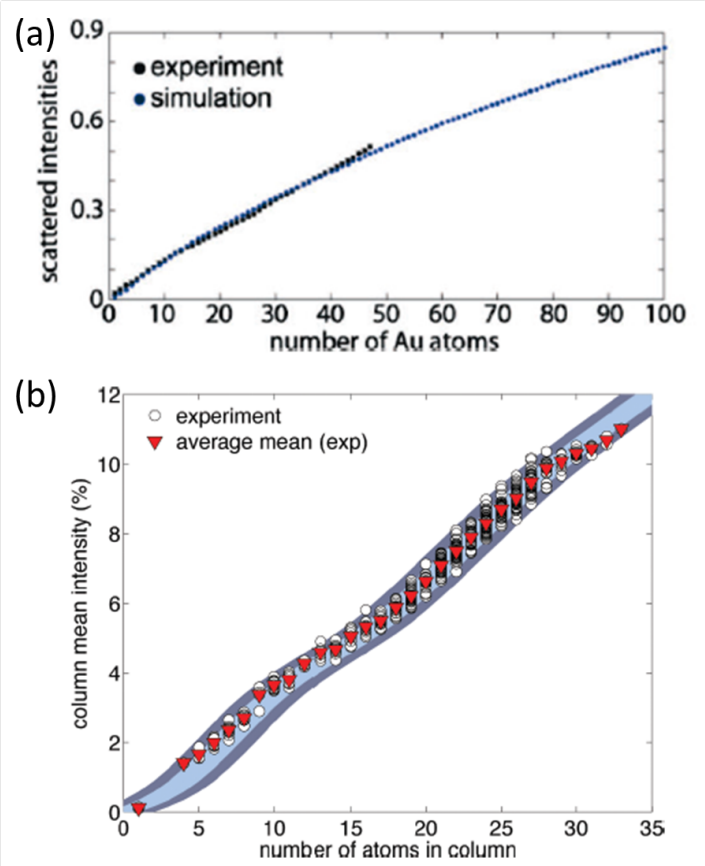

Figure 6.2: Linear dependence between the intensity measured via HAADF and the sample thickness, i.e. the number of atoms stacked above each other. (a) represents the results found by Jones [29] and (b) are the results found by LeBeau *et. al.* [38]. Both graphs are taken from [29] and [38]

.

Algorithm 1 Grid creation algorithm

1.) Read Data $\hat{D}$ ($i \times k$ matrix) from intensity profile obtained via TEM images.
2.) Set I_0 adequately (a few variations are essential)
3.) Initialize three-dimensional 0-1 matrix $\hat{G}$. The number of pixels in height is set to be approximately $2 \cdot I_{max}/I_{Step}$

for n = 1:ceil(I_{max}/I_0) **do**
  $I_{\pm n} = n \cdot I_{Step} + I_0$
  for all entries in $\hat{D}(i,j)$ **do**
    If $\hat{D}(i,j) \geq I_n$, $\hat{G}(i,j,n) = 1$
  end for
end for

6.2.3 Disadvantages of a 2D approach

It is important to mention that the reason why a three-dimensional approach, instead of a two-dimensional one, is chosen, is that the likelihood for vacancies migrating into the grid during the time evolution is much higher than for a three-dimensional grid. This is a result of the lower number of nearest neighbour cells (only 8 instead of 26 possible neighbour places) for a two dimensional grid in comparison to a three-dimensional one. The full description of the migration process of voxels is described within the next section. In Figure 6.3, a time evolution of a two-dimensional grid is depicted (to highlight the disadvantage of a two-dimensional representation).

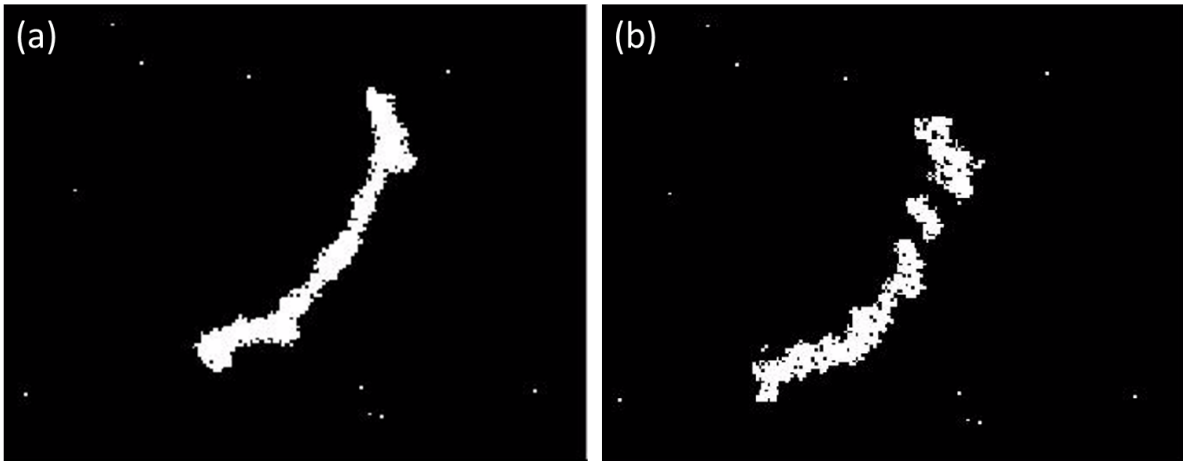

Figure 6.3: Time evolution of a 2D cellular automaton from its initial configuration (a) to (b). The major drawback of a 2D representation is clearly visible: An increase in the vacancies migrating into the cluster.

6.2.4 Migration Algorithm of the Cellular Automaton

The dynamics of the CA are defined by the choice of update rules which apply to all cells or voxels of the system. As mentioned above such a voxel is either filled with material or remains empty. These updates are executed simultaneously for all cells in each time step. A simulation of the thermally induced surface diffusion process can now be obtained by choosing update rules which describe a particle hopping on the grid. This process depends on the local environment of a voxel, but must also account for the stochastic character of a temperature-driven particle migration. This can be achieved by introducing a series of update rules to model the time evolution at a given temperature:

1. An empty cell can become filled if there is a filled neighbour cell and the corresponding hopping condition is fulfilled.

2. A filled cell can become empty if there is an empty neighbour cell available and the hopping condition is fulfilled.

3. The reaction rate k for a hopping from cell a to b is given by by employing an ansatz from reaction kinetics, the Eyring equation[13], defining jumping rates via

$$k = \frac{k_B T}{h} exp\left(\frac{-\Delta F\left(E_{\text{bond}},d_{\text{bond}},n\right)}{RT}\right). \tag{6.3}$$

With k being the probability for voxel migration andΔF is the free energy barrier to overcome. The latter depends on the atomic bond energy E_{bond} and the atomic bond distance d_{bond} of the investigated metal. The free energy barrier ΔF is a function of the binding length d_{bond} and the number of next nearest neighbours n of one voxel. For the material specific parameters E_{bond} and d_{bond} well known values tabulated in literature are used[31], which are tabulated below for all materials used within this thesis. As soon as the rates for all possible hoppings of a filled cell are evaluated, a random number is drawn between 0 and 1. The normalized hopping rates and the random number are then used to determine the actual hopping event.

Table 6.1: Material parameters used in the cellular automaton[31]

Material	E_{Bond} [kJ/mol]	d_{Bond} [nm]
Au	368	0.145
Ag	284	0.144
Ni	428	0.125
Cu	336	0.128
Pd	376	0.138
Bi	210	0.170

As k is strongly dependent on the temperature, the reaction rate will drastically increase as soon as the thermal energy is high enough to overcome the energy barrier ΔE and detach one voxel from its neighbour cells. Fig.6.4 illustrates one voxel of a nanowire which might undergo particle migration (red cell). The more neighbour cells one voxel has the less likely a jumping event will become, as $\Delta F \sim n$.

After detaching, the voxel is free to change its position within its nearest neighbourhood. The number of nearest and next nearest neighbours determine, together with the probabilities derived for possible migrations, to which position the voxel will most likely be transferred. The probability to which neighbouring position a particle might migrate is again determined via the Eyring equation 6.3. As the particle is restricted to change its position only within its nearest neighbourhood (26 possible neighbouring sites), only the number of nearest and next nearest neighbouring cells determine the jumping probabilities to possible jumping sites. To evaluate which neighbouring site has which jumping probability, the number of neighbours of this neighbour cell is evaluated (not counting the jumping voxel) and stored in form of a $(3\times3\times3)$-matrix. This matrix

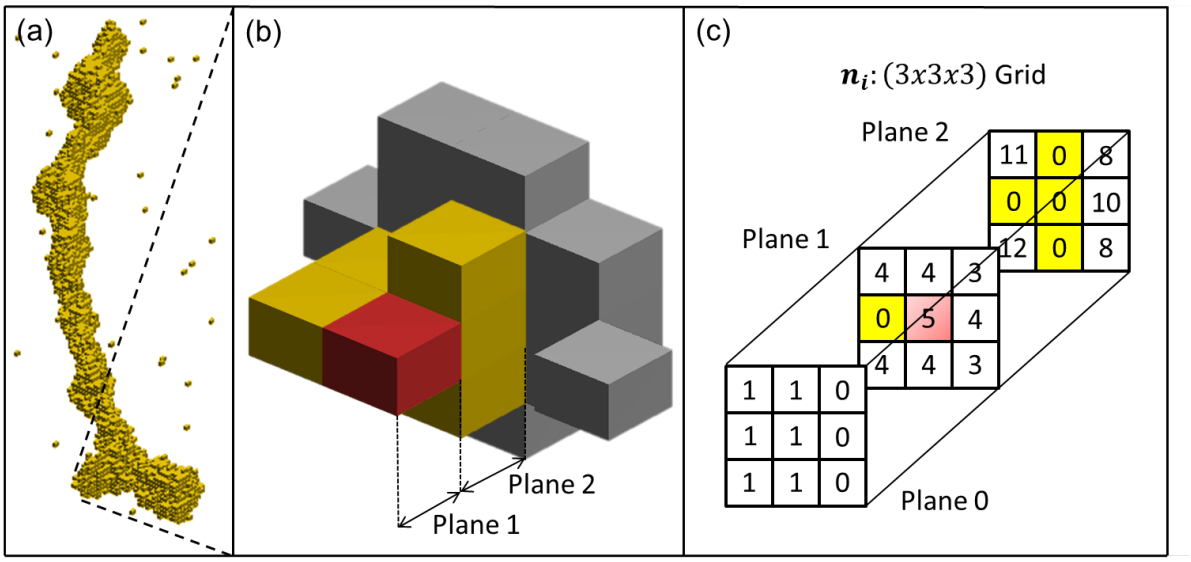

Figure 6.4: An illustration of the cellular automaton principle for a given structure. a) A three-dimensional rendering of a real nanowire in the CA grid space. b) A detail of the structure, showing the neighbourhood (gold) of a selected cell (red). Cells printed in grey lie outside the direct neighbourhood, but determine the number of neighbours' neighbours. c) A diagrammatic representation of the neighbourhood of the selected cell. The numbers in the boxes represent the number of neighbours after a jump to this cell. Note that occupied cells (gold) are set to zero by definition, which removes them from the list of possible hopping options.

n_i is represented within Figure 6.4 (c) for one specific example of a local neighbourhood (b). Note that it is forbidden to move the voxel to an already occupied position (highlighted in yellow) in order that the number of particles stay the same throughout the whole migration process. For all allowed entries of n_i the Eyring equation 6.3 is evaluated, giving different probabilities for migrating to different neighbour sites of the voxel. All probabilities are then stored in form of a temporary storage vector $\vec{v_i}$. This vector is then normalized and a random number from 0 to 1 is drawn to determine to which neighbouring position the particle will migrate. As mentioned above the transition probability is $k \sim \exp\{n\}$, the particle will most likely migrate towards a position with a high number of nearest neighbours.

This detaching and migration algorithm is repeated for each voxel, capable of detaching (a voxel can be 'trapped' when surrounded by 26 neighbours). Double occupations of a given cell must be forbidden if a constant metal density is assumed. In addition their should be no voxel, which is able to jump always as the first or last one, in order to provide the stochastic character. This is achieved by tabulating all possible jumps for a given time step, followed by a random permutation of the jumping events before the actual migration takes place, in order to eliminate any bias introduced by the serial

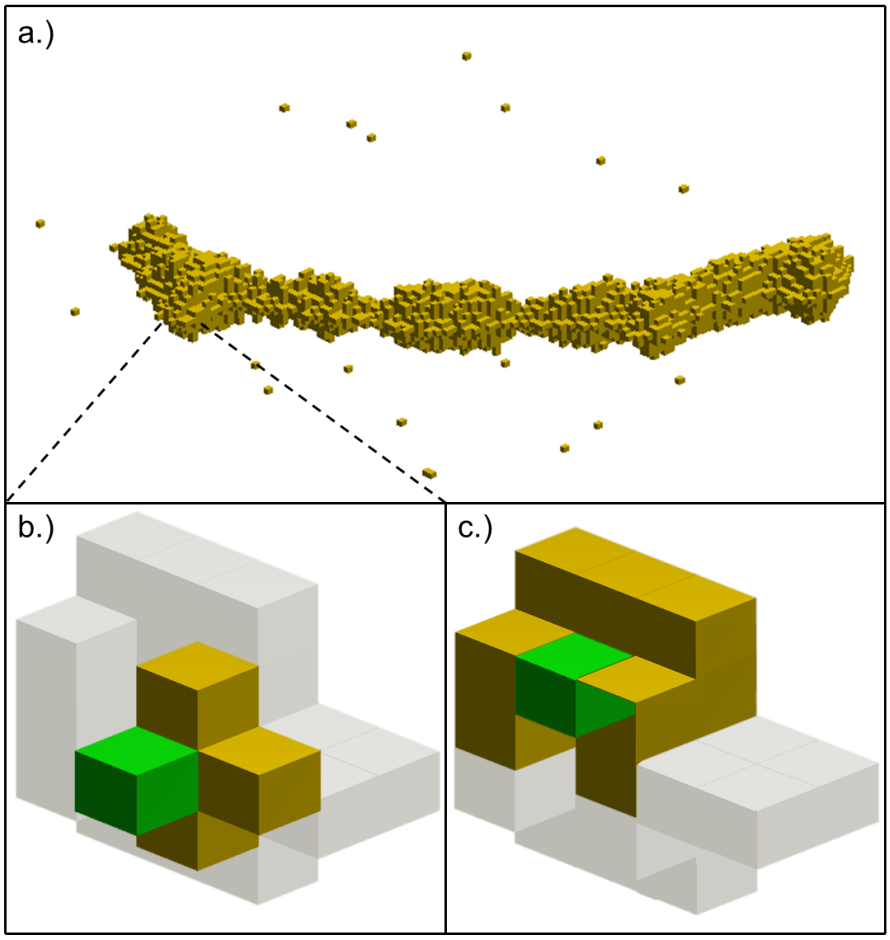

Figure 6.5: Example of a local neighbourhood of a surface voxel (green) undergoing surface diffusion. Illustration (b) depicts a segment of the complete nanowire (a) with its local neighbourhood, showing filled neighbour voxels printed in gold and filled voxels outside the direct neighbourhood in gray. Illustration (c) shows the situation after a hopping process has taken place. The number of new neighbours has increased and the total energy is therefore reduced.

processing of the cells.

With ongoing simulation time, this algorithm leads to preferably spherical structures, where the number of nearest neighbours in total reaches a maximum. Note that this model does not take any surface interaction into account due to the extremely low wetting behaviour of the chosen substrate. This is particularly obvious for the interaction of gold and carbon in comparison to the intermetallic bond energy ($E_{\mathrm{Au-C}} = 0.03$ eV/atom [16], $E_{\mathrm{Au-Au}} = 3.81$ eV/atom [31]). For a two-dimensional study of surface diffusion including the interaction with various substrates the reader should be referred to the work of Solov'yov *et al.* on Ag nanoparticles [50].

Figure 6.5 displays graphically the situation of a selected surface voxel and its initial neighbourhood. In this setup, the energy can be minimized by moving the green voxel in a way which maximizes its number of neighbour voxels. The stochastic character of the process of breaking and forming bonds enters via equation 6.3, which yields the probabilities for hopping events.

Those update rules are capable of describing the very nature of thermally induced surface diffusion processes. In the following *algorithm* 2 the complete structure is listed again, in order to give a better overview how the CA actually works.

It should also be mentioned that diffusion time is not directly linked to the *in-situ* observed diffusion process. Therefore, a fit between the observed time dependent TEM surface diffusion process at constant temperature and the stepwise iteration process is necessary for realistic predictions of the behaviour over time. The simple linear dependence of the pre-exponential factor in Equation 6.3 is derived from statistical mechanics under the assumption of a single degree of freedom being responsible for reaction barrier transmission. The fact that not every attempt in this degree of motion leads to a successful hopping is usually taken into consideration by a proportionality constant κ referred to as the transmission coefficient. Although not in the atomic picture, it is possible to follow this nomenclature for the discussion of voxel migration and adsorb all unknown scaling factors which occur in the coarse-grained model into this constant κ. With $F = E - TS$ the Equation 6.3 can be rewritten as

$$k = \frac{k_B T}{h} \exp\left(\frac{\Delta S(T)}{R}\right) \exp\left(\frac{-\Delta E\left(E_{\text{bond}}, d_{\text{bond}}, n\right)}{RT}\right) \tag{6.4}$$

The temperature dependence of the entropy can also be adsorbed into κ by writing it as a function of the temperature, leading to

$$k = \kappa(T) \exp\left(\frac{-\Delta E\left(E_{\text{bond}}, d_{\text{bond}}, n\right)}{RT}\right). \tag{6.5}$$

This expression, together with a series of TEM observations over time made at constant temperatures, allows to connect the number of update cycles in the CA simulation to the real time evolution by fits of $\kappa(T)$. The results of a time evolution are presented within the next chapter.

Algorithm 2 Cell update algorithm

Read Data $\hat{D}$ ($i \times k$ matrix) from intensity profile obtained via TEM images.

Translate $\hat{D}$ into a three-dimensional 0-1 matrix via the grid creation *algorithm* 1.

for t = 1 to length of simulation **do**

Create a vector $\vec{l_t}$ containing all voxels, which are not trapped (neighbours < 26)

Apply a random permutation of the entries of $\vec{l_t}$

for u = 1 to length of $\vec{l_t}$ **do**

if Voxel overcomes the energy barrier given by the Eyring equation **then**

Create local neighbourhood matrix n_i, containing the number of neighbours, when moving to a neighbouring site.

Exclude forbidden jumping events (sites which are already occupied are forbidden)

Create a vector, which uses all allowed entries in n_i to evaluate the jumping probabilities to these sites, using equation 6.3.

Draw a random number between 0 and 1 to determine the jumping event.

Move the voxel to this new position.

elseVoxel does not overcome the energy barrier

Voxel will remain in its original position.

end if
end for
end for

6.3 Simulation of Surface Diffusion

In this section the results of the cellular automaton algorithm, described above are presented. The first part is about the simulation of the breakup behaviour observed via TEM imaging of metallic nanowires on a heated substrate or observed within a cryo-experiment. The wires are studied separately, but using the same algorithm.

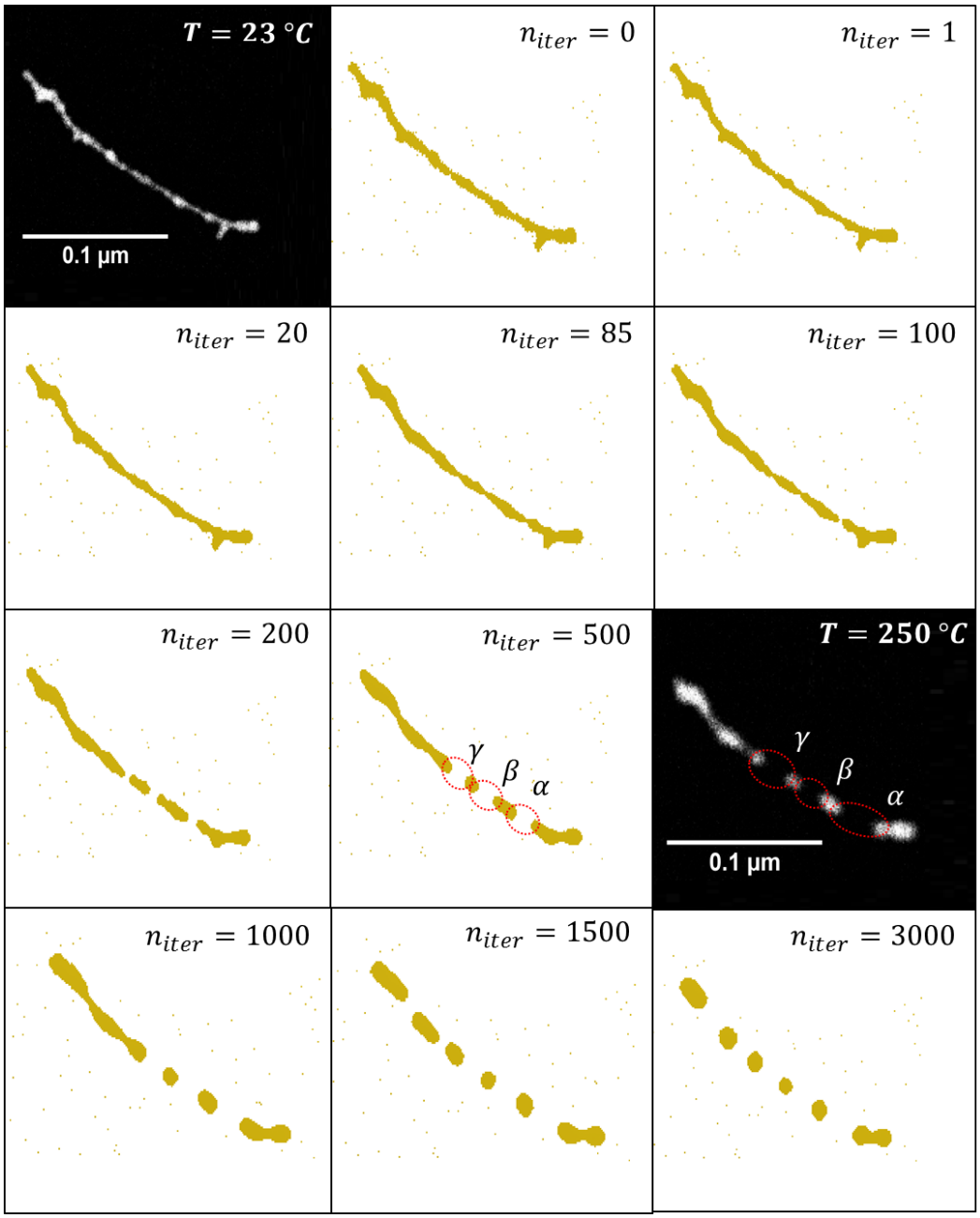

Figure 6.6: CA simulation of the surface diffusion for an Au nanowire structure derived from TEM images. For a given temperature, the propagation in time is simulated by a series of update cycles for the CA. A reshaping of the nanowire becomes evident, which leads to multiple Rayleigh breakup events, labelled with greek letters in chronological order. Eventually, qualitative changes in the structure between cycles become marginal as the remaining fragments reach their local minimum of spherical shape. Two HAADF-TEM images have been added for direct comparison.

At first, the TEM image of freshly deposited nanowires at room temperature is discretized on the grid. The obtained structure is shown in the upper left image of Figure 6.6. Note that the actual grid of the CA is three-dimensional, but only a 2D projection is shown for easier comparison to the TEM images. In the very first step a slight smoothing of the structure appears as the naturally occurring noise of the image translation is removed instantly. In the following series of cell update steps or 'cycles' in CA terminology the shape shifting effects of surface diffusion become evident. After 20 cycles a thinning of certain regions becomes apparent, which gets more and more emphasized (cycle 85) until the first breakup occurs (cycle 100), here at the lower end of the wire structure. A series of additional breakups follows (cycles 200-500). After that, the qualitative changes in the structure between cycles become marginal. After twice the simulation steps have passed (cycle 1000) the last breakup events occur and the remaining parts become more and more droplet-like (cycle 1500). For very long propagation in time (cycle 3000) all remaining fragments reach their local minimum of spherical shape, i.e. a circle in the two-dimensional projection.

As can be seen in Figure 6.6, the simulation agrees well with the experimental outcome and with the dynamics observed in the TEM study. Breakup sequences and positions are fully reproduced by the simple CA model. However, a direct comparison of different metals with respect to stability is not straightforward as material properties only enter via hopping probabilities. Therefore, the Rayleigh breakup patterns are material-independent in the sense that infinite time propagation will lead to the same results for all metals. However, the process itself will be faster in cases where metallic binding energies are higher since they enter the hopping probability in the exponent. This puts the cycles needed for a breakup in a given structure into a direct relation with the material and allows to rank different metals with respect to their stability at a given constant temperature.

The principle of surface diffusion for different materials is illustrated in the two following figures Figure 6.7 c.) and d.), where the voxels tend to leave the initially constricted points, which results in a patternization of the nanowire. The migration is initiated by the energy gain when moving into an energetically more preferable position, where the sum of the number of all nearest neighbours of all voxels is larger than in the initial configuration of the wire. Which corresponds in other words to the minimization of surface energy in the macroscopic picture.

The following features and their temperature dependence are well predicted by the simulations for all materials tested:

- Smoothing of the surface of the wires as a result of the induced surface diffusion.
- Rayleigh breakup and fragmentation of the nanowire.
- Contraction of nanostructures by minimization of the number of surface atoms

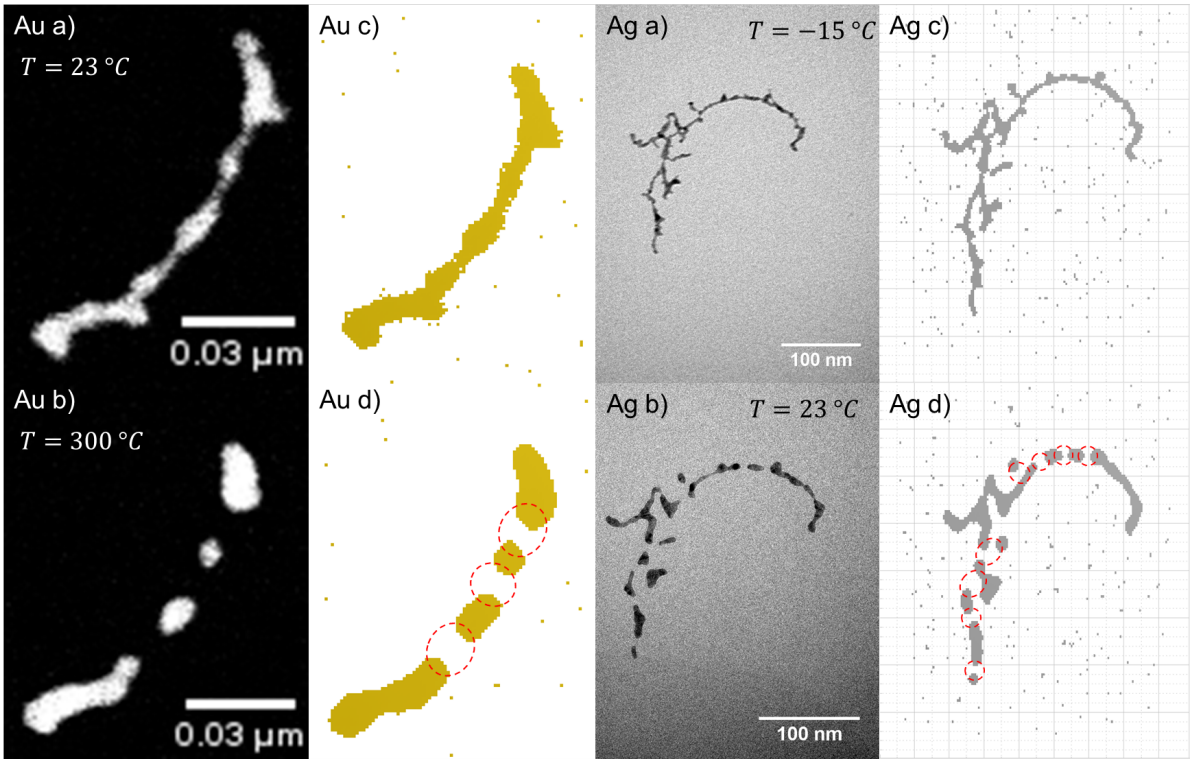

Figure 6.7: Comparison between measured surface diffusion processes and cellular automaton prediction of a Au and Ag nanowires. In a.) and c.) is is possible to see the initial structure and the converted structure used in the cellular automaton approach, respectively. Those structures evolve to the ones shown in d.), when heating is applied, in very good agreement with the final structures observed experimentally b.).

- The exact breakup points and final shape of the wires

The CA ansatz further allows the prediction of the breakup-sequence of constriction points. Note that the diffusion process is simulated in three dimensions, although measurement is limited to a "projected", two-dimensional view. The dynamics during the simulation matches the structural changes observed in the TEM nicely.

The agreement between simulation and measured structures after heating can be seen in Figure 6.7. Even for very complex forms we are able to accurately predict the exact surface diffusion process. However, a correction factor has to be introduced to the Eyring equation in the case of the more reactive metals Cu and Ni, which accounts for the formation of an oxide layer on the surface of those clusters. This oxide layer is assumed to quench particle migration, leading to an inhibited or delayed breakup.

The accelerating effect of higher temperatures is also captured by the ansatz given in Equation 6.3. However, in order to be able to predict breakup events in time, it

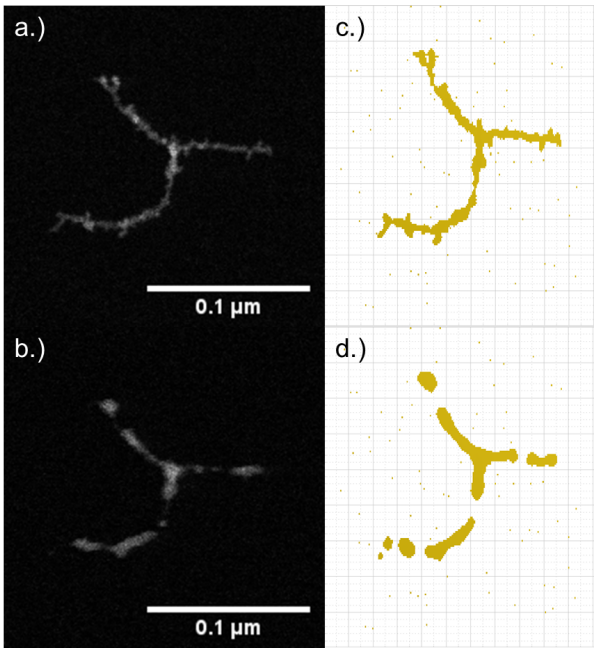

Figure 6.8: Surface diffusion for a nickel nanowire, a comparison between the experimental TEM results (a) and (c) and the predicted surface diffusion from the CA (b) and (d). Note that it is essential to insert a fitting factor into equation 6.3 in order to predict the temperature induced stabilization caused by the surface oxide layer. After using a correction factor and evolving the structure in time the CA shows good agreement with the TEM results.

becomes necessary to estimate the amount of material displaced in each cycle. For the case of gold nanowires a more detailed study of time dependence which includes a fit of the transmission coefficient $\kappa(T)$ is performed. Its structural development is observed in a series of TEM images taken at a constant substrate temperature of $150°C$. The surface diffusion of gold nanowires in real time is studied and compared to the structure evolution simulated with the CA. A selection of nanoparticles and their corresponding constriction points in time are used to perform a linear fit of the real time evolution as a function of the number of update cycles. For this particular combination of materials (Au nanowires on a non-wetting support) and the given temperature we find that 1500 real time seconds of TEM observation correspond to 100 iteration steps. One example of a Rayleigh breakup as a function of time and iteration step is presented in Figure 6.9.

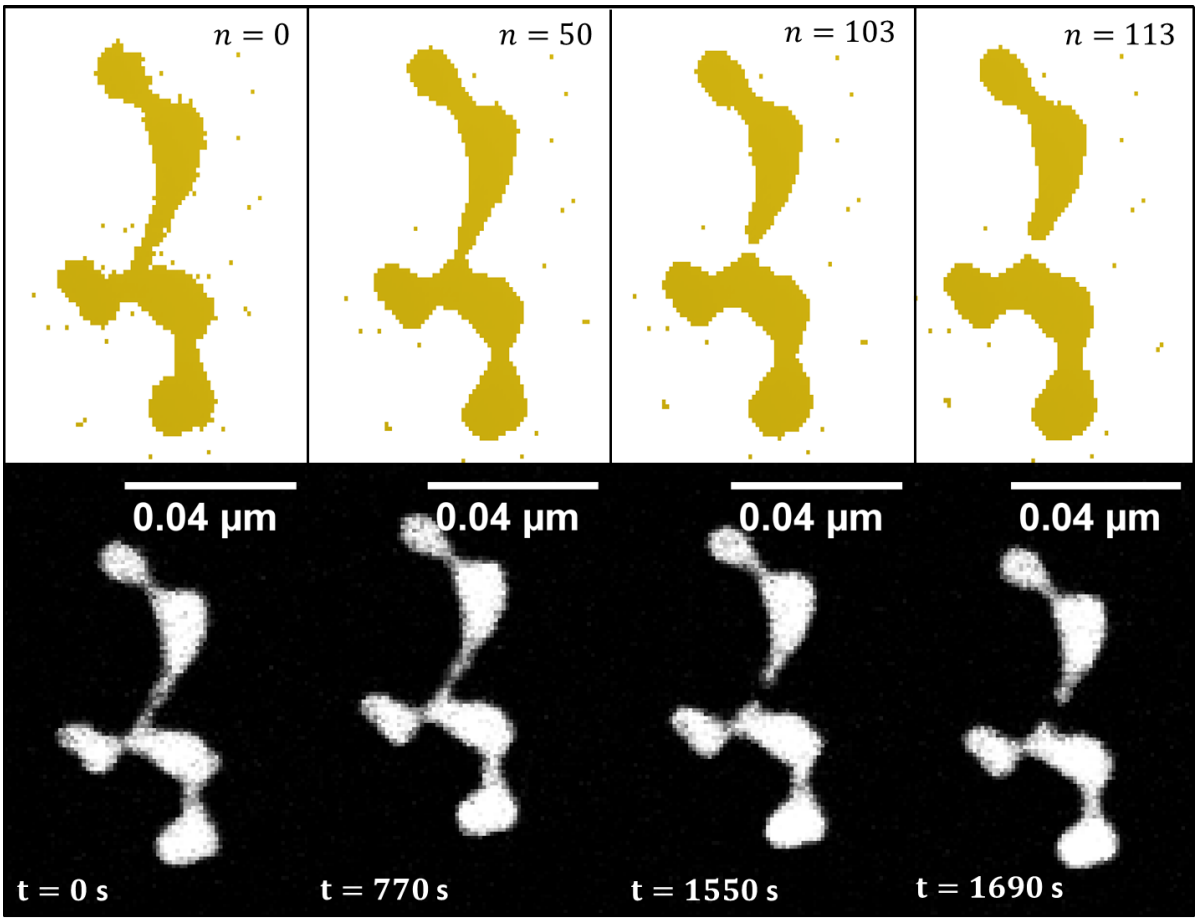

Figure 6.9: Time evolved surface diffusion process of a gold nanowire at 150°C. The observed *in-situ* breakup event is studied over a time period of nearly half an hour (lower images) and are compared to the results obtained with the CA (upper images) in order to draw a fit between iteration steps and experimental observation time.

6.4 Surface Wetting

In this section the simulations are extended by the introduction of additional parameters which characterize the support material in more detail. The wetting behaviour of a selection of metals (Ni, Pd, Au) on amorphous carbon is analysed, with the aim to reproduce the typical shapes obtained for originally spherical nanoparticles deposited on a substrate.

At first, the wetting situation for a given metallic nanoparticle is characterized based on simple geometric arguments as illustrated in Figure 6.10. Assuming an incomplete sphere as the shape of the metallic nanoparticle after adsorption onto the substrate, an angle α can be defined which determines the size of the missing spherical cap. In this simplified model, an analytical relation between α and the intensity profile $I(x)$ for such

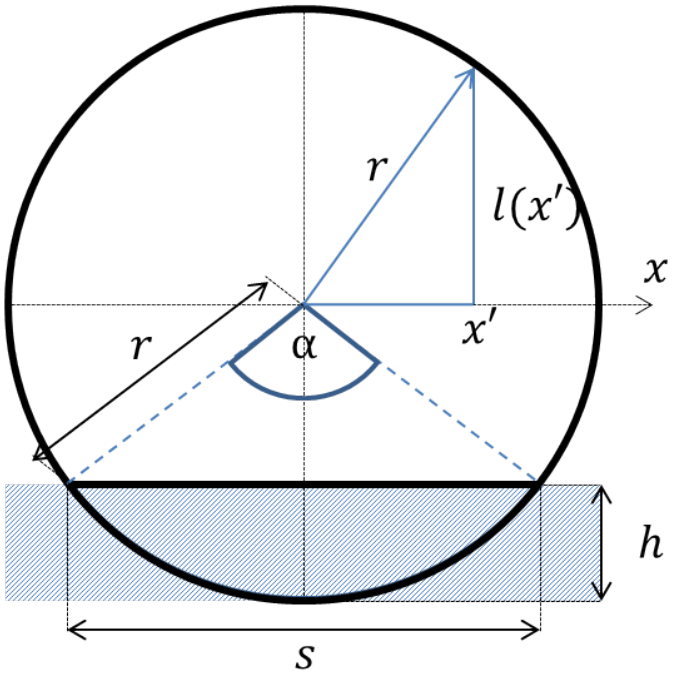

Figure 6.10: A simple geometric model for the adsorption of spherical nanoparticles onto a substrate. The volume of a spherical cap with height h is redistributed over the particle. The radius of the cap reflects the wettability of the chosen metal.

an adsorbed and deformed particle can be derived,

$$I(x) \propto l(x) + l(x) \cdot H(|x| - s/2) + (r - h)H(s/2 - |x|), \tag{6.6}$$

with the additional relations

$$h = r(1 - \cos(\alpha/2)) \text{ and } s = 2r \sin(\alpha/2), \tag{6.7}$$

where r denotes the particle radius, h the height of the cap, $l(x)$ the thickness of the unmodified upper half of the sphere, s the radius of the cap, and $H(x)$ the Heaviside step function. Equation 6.6 is based on the assumption of a linear relationship between the thickness of the particle (with thickness defined as particle width in the direction of observation) and the intensity in the two-dimensionsal scanning-TEM image. This well-known feature holds as long as no saturation effects occurs, i.e. for metallic particles with diameters of only a few nanometers, and is commonly used to obtain additional morphology and composition information in high-angle annular dark-field (HAADF) scanning transmission electron microscopy.[29, 30, 38]

A fit of this simplified model to the real TEM data for small Ni, Pd and Au nanoparticles is shown in Figure 6.11, together with the corresponding images. A very small α value

for Au (9°) is found in comparison to Pd (31°) and Ni (53°), which indicates a significantly reduced wetting in the case of gold. This is also deducible from the slightly more abrupt change of TEM contrast at the edges of the Pd and Ni particles in comparison with Au.

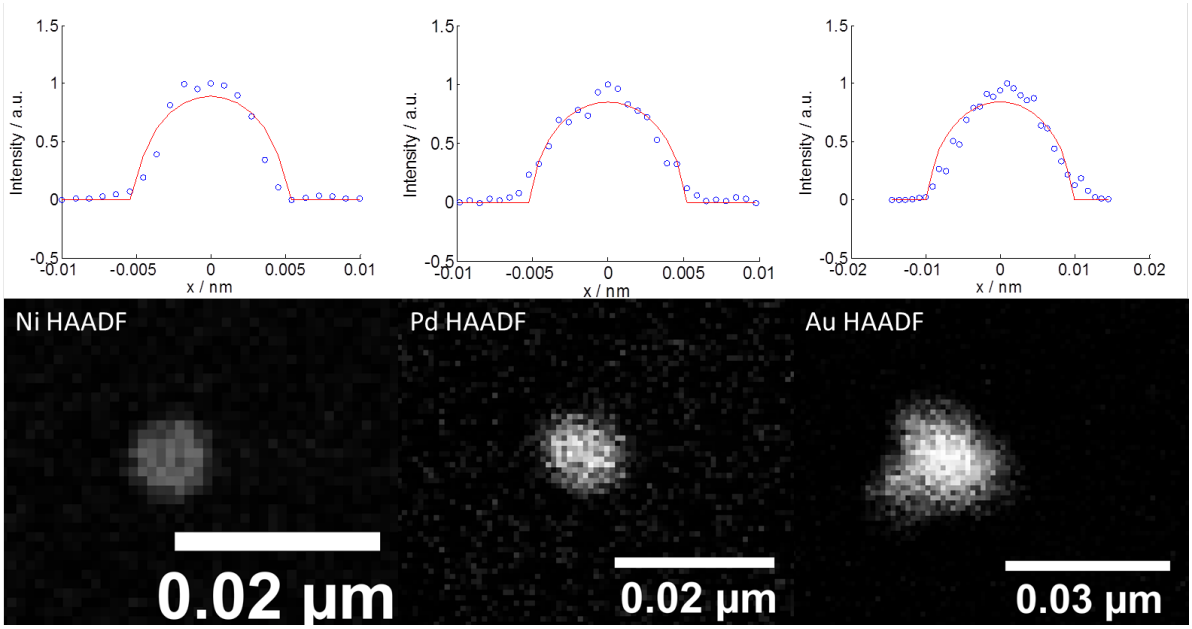

Figure 6.11: HAADF-TEM images of Ni, Pd and Au nanoparticles consisting of approx. 1000 metal atoms (lower panel) together with the corresponding intensity profiles (blue data points in the upper graphs). The red curves are obtained by fitting the analytical function given by Equation 6.6 to the experimental data with α as free parameter.

In a second step, the algorithm behind the CA approach is extended. The interaction with the substrate is included by means of added binding energies for the occupation of cells directly above the surface plane. For a particle of a given size and metal, the outcome is only determined by the ratio of the metal-metal and metal-surface interaction energies. A series of simulations with various ratios is depicted in Figure 6.12, showing the converged result of the diffusion process for cases from minimal to significant surface wetting. From this, an approximately linear relation between the angle α (53°, 31° and 9° for Ni, Pd and Au) which defines the size of the spherical cap in the geometric model and the actual ratio of metal-metal energies E_{mm} to metal-surface energies E_{ms} can be derived:

$$\alpha[\mathrm{rad}] \approx 8.8 \times E_{\mathrm{ms}}/E_{\mathrm{mm}} \tag{6.8}$$

This relation allows for a crude estimation of E_{ms} values of Ni, Pd and Au with the amorphous carbon surface based on the corresponding metal-metal interaction energies.

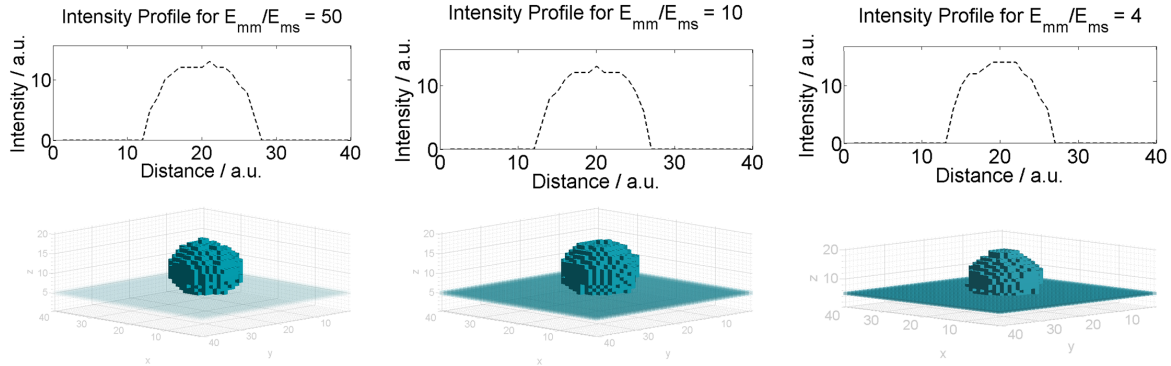

Figure 6.12: Intensity profiles (upper panel) and converged shapes obtained from CA simulations of metallic nanoparticles adsorbed onto amorphous carbon. Different ratios of $E_{\mathrm{mm}}/E_{\mathrm{ms}}$ affect the steepness of the curves near the particle edges. From a series of simulations, a linear relation between the energy ratios and the angle α defined in Figure 6.10 could be derived and used for the prediction of E_{ms} from known E_{mm} values.

Table 6.2: Comparison of E_{mm}, the metal-metal interaction energies [31] (the only input data of the CA) to derived E_{ms} values and the corresponding *ab initio* surface adsorption energies ΔE_{C} taken from Ref. [16]. Absolute energies are given in kJ/mol, ionic radii r_{i} in nm.

	E_{mm}	r_{i}	n_{v}	n_{b}	α	E_{ms}	$\bar{E}_{\mathrm{ms}}$ [a]	ΔE_{C} [b]
Ni	428	0.125	85	2.89	53°	45	1170	444
Pd	376	0.138	63	2.23	31°	23	462	296
Au	368	0.145	55	1.96	9°	7	123	111

[a] $\bar{E}_{\mathrm{ms}}$ is the energy gain by surface interaction per filled surface cell (which has 9 surface neighbor cells, i.e. $\bar{E}_{\mathrm{ms}} = 9 n_{\mathrm{b}} E_{\mathrm{ms}}$).
[b] ΔE_{C} is defined as the energy needed to remove a $(0.95\ \mathrm{nm})^2$ sheet of graphene from the bulk metal (111) surface; see text for details.

Despite its simplicity, this method produces relative surface interaction energies which are in reasonable agreement with *ab initio*-derived adsorption energies for the selected (111) metal surfaces on graphene[16]. A comparison of our experimentally determined E_{ms} and $\bar{E}_{\mathrm{ms}}$ (for amorphous carbon) with the *ab initio* value ΔE_{C} (for graphene) shows that our values follow the same relative trend. Table 6.2 contains the metal-metal interaction energies E_{mm} which are used as input parameters for the CA, and compares the derived metal-carbon interaction energies E_{ms} to surface adsorption energies from Ref. [16]. The approximate number of metal atoms per cell n_{v} as well as the average number of bonds per filled cell neighbour n_{b} can be derived from the ionic radii r_{i} listed

in the second column. From this, the energy gain can be estimated which occurs due to the interaction of the filled cell with its 9 'substrate' neighbour cells. The latter can be directly compared to the ab initio values from Ref. [16] for the interaction with graphene. An atomic density of 37 carbon atoms per $(0.95\ \mathrm{nm})^2$ has been assumed for this comparison, derived from the well known molecular structure of graphene [45] with a C-C bond length of 1.42 Å.

The largest discrepancy between our prediction and the *ab initio* value occurs for nickel, which might be related to a reduced image contrast for the lighter Ni atoms and due to more pronounced oxidation effects. Furthermore, nickel is known as a wetting electrode on graphene at higher temperatures, forming carbides at the contact surface[19, 34, 62].

6.5 Further Applications

Within this chapter the great advantages of a cellular automaton were presented. It has been shown that this computational approach is able to predict Rayleigh breakup phenomena observed for metallic nanowires with diameters of a few nanometers. It reproduced the final shape after heating treatments and correctly predicts the chronological order and the location of wire breakup events for any given shape, as could be verified by *in situ* TEM-imaging of heated samples.

The next logical step for further extension would be the implementation of a second atomic species. A prototype of a more complex and general model has already been able to describe the wetting behaviour of nanoparticles on a substrate. A more general ansatz would be to not only create a grid with occupied and unoccupied voxels, but rather with unoccupied and different possible occupation types/occupation materials. This intermixing of different species needs however, additional knowledge about the inter-metallic bonding energies E_{m_i,m_i}, as well as all varieties of bond energies of different species of atoms E_{m_i,m_j}. A preliminary approach is tested and presented in Figure 6.13, showing the start of a core-shell formation, as a result of different binding energies of the two metals.

The main challenges however, would be the implementation of possible exchanges of voxels and the implementation of an adequate intermixing term, as one voxel contributes only to one atomic species. As a result intermixing of different species would be a major challenge to deal with.

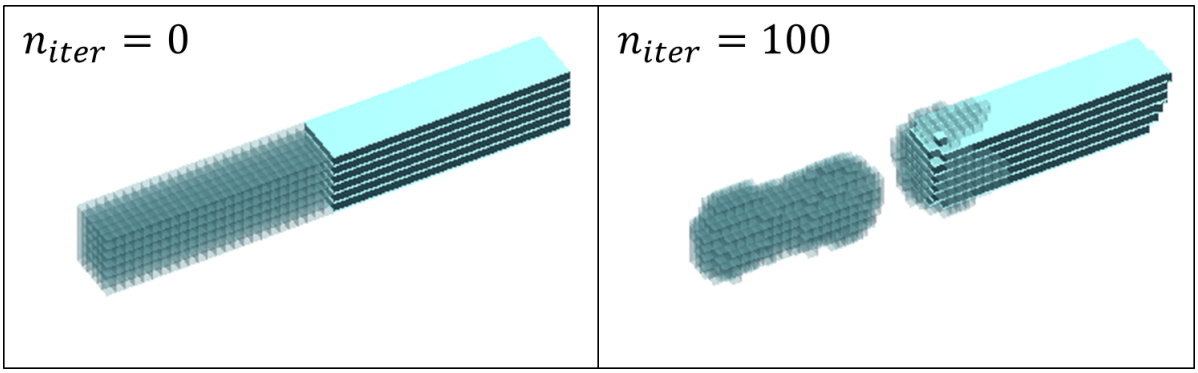

Figure 6.13: Cellular Automaton for a nanowire containing two different species of atoms (bright and dark voxels represent different species). The interaction energy of the bright voxels is set to be smaller then the interaction energy between the bright and dark voxels, resulting in a breakup and a wetting part.

Chapter 7

Summary

In this thesis the temperature-dependent break-up process of Cu, Ni, Au and Ag nanowires is analysed at 1 nm spatial resolution.

Experimental studies have shown that the breakup temperature for nanowires is significantly smaller in comparison to the corresponding bulk melting temperature. In addition, a $1/d_{nw}$ dependence for the reduced breakup temperature T_{nm}/T_{bm} is found and the effect of an oxide layer on the stability is studied. The oxide layer leads to an inhibited particle diffusion, which slows the process down continuously and eventually increases the observed breakup temperature. It is possible to simulate the temperature dependent behaviour even for complex structures.

A new method based on the cellular automaton principle has been introduced, which allows the simulation of surface diffusion processes in metallic nanoparticles. For the simulations, realistic shapes are derived from TEM images and translated into discrete 3-D models. The grid size for the model structures is determined by the resolution of the TEM image and corresponds in the studied cases to cells of $(0.95\ \mathrm{nm})^3$ or approximately 55-85 metal atoms depending on the element. A series of cell update rules is then defined in order to simulate surface diffusion by cell hopping events. Hopping probabilities are estimated based on the difference between the number of occupied neighbour cells before and after the hopping. In order to introduce an element-specific hopping probability a set of parameters from known binding energies between the elements involved have been derived. With this ansatz, even the behaviour of larger metallic structures can be correctly predicted and reproduced. The reduction to nearest-neighbour interactions, a fundamental aspect of the cellular automaton model, allows for a highly efficient computation of surface diffusion processes.

This computational approach is able to predict Rayleigh breakup phenomena observed for metallic nanowires with diameters of a few nanometers. It reproduces the final shape after heating treatments and correctly predicts the chronological order and the location of wire breakup events for any given shape, as could be verified by *in situ* TEM-imaging of heated samples. Assuming a non-wetting behaviour for all studied metals on amorphous carbon, the cellular automaton produces material distributions which are in good agreement with the particle shapes derived from the TEM images. The model was fur-

ther extended by explicitly introducing interactions with the substrate, which enabled the reproduction of the deformations observed for the Ni, Pd and Au nanostructures due to surface adsorption effects. The relative strength of metal-carbon interactions derived from the TEM-inspired CA approach agrees reasonably well with the available *ab initio* data for the binding energies of graphene on bulk (111) surfaces of the selected metals.

Chapter 8

Appendix

This chapter serves as a source for more detailed information about several topics, which are only mentioned briefly within the main part of this thesis, but are nevertheless important in order to get a deeper understanding of the discussed topics.

8.1 Statistical Mass Distribution Considerations

In this chapter the multinomial mass distribution of metal clusters is discussed in more detail. The statistical background and the program was carried out in cooperation with Pascal Heim, who brought in his expertise in the field of statistical physics.

Given a metal with k stable isotopes, in which every stable isotope has an occurrence probability p_i ($i \in \{1,...,k\}$), which forms a cluster of N atoms and having a total mass M, the probability to find a cluster with N atoms and having a total mass of M can be written via the marginalisation rule.

$$p(M,N|\vec{p}) = p(M|N,\vec{p}) \cdot p(N|\vec{p}) \tag{8.1}$$

This can be extended when introducing a vector $\vec{n}$, which lists the number of all isotopes n_i, that correspond to the total number N and total mass M of the cluster. Therefore the following two relations must be fulfilled.

$$\sum_{i=1}^{k} n_i = N \tag{8.2a}$$

$$\sum_{i=1}^{k} n_i m_i = M \tag{8.2b}$$

Equation 8.1 can be extended by using the marginalisation rule.

$$p(M,N|\vec{p}) = \sum_{\vec{n}} p(M|N,\vec{p},\vec{n}) \cdot p(N|\vec{p},\vec{n}) \cdot p(\vec{n}|\vec{p}) \tag{8.3}$$

The probability $p(M|N,\vec{p},\vec{n})$ to find a specific total mass M, given N amounts of atoms, with an isotope distribution $\vec{p}$ and $\vec{n}$ can be written as a δ function using equation 8.2b:

$$p(M|N,\vec{p},\vec{n}) = \delta\left(\sum_i n_i m_i = M\right) \tag{8.4}$$

The second probability in equation 8.3, which describes how likely a cluster with a total number of N atoms given $\vec{p}$ and $\vec{n}$ can be found, is given via the multinomial distribution under consideration that equation 8.2a is still valid.

$$p(N|\vec{p},\vec{n}) = N! \prod_i \frac{p_i^{n_i}}{n_i!} \delta\left(\sum_i n_i = N\right) \tag{8.5}$$

Given this information, and knowing that the last term in equation 8.3 can be cancelled, $p(M,N|\vec{p})$ can be written as:

$$p(M,N|\vec{p}) \sim \sum_{\vec{n}} \delta\left(\sum_i n_i m_i = M\right) N! \prod_i \frac{p_i^{n_i}}{n_i!} \delta\left(\sum_i n_i = N\right) \tag{8.6}$$

A numerical solution of this equation is very time consuming, because for every k one additional loop inside the program has to be added, which is very expensive, even if assumptions like the Stirling approximation are used.

A much cheaper approach, in terms of computational time can be achieved when using convolution integrals. From the given distribution $p(N = 1,M|\vec{p},\vec{n})$ all distributions with higher N can be created. The initial $N = 1$ distribution can be written as:

$$p(N = 1,M|\vec{p},\vec{n}) = \sum_{i=1}^{k} p_i \delta(M = m_i) \tag{8.7}$$

When splitting the total number of atoms into $N = N_1 + N_2$, equation 8.3 can be rewritten as a sum of both N_1 and N_2.

$$p(N = N_1{+}N_2,M|\vec{p},\vec{n}) = \sum_{N_1,N_2} p(N = N_1{+}N_2,M|\vec{p},\vec{n}){\cdot}p(N_1,M|\vec{p},\vec{n}){\cdot}p(N_2,M|\vec{p},\vec{n}), \tag{8.8}$$

which can be simplified using $p(N = N_1 + N_2,M|\vec{p},\vec{n}) = \delta(N = N_1 + N_2)$.

$$p(N = N_1 + N_2,M|\vec{p},\vec{n}) = \sum_{N_1} p(N_1,M|\vec{p},\vec{n}) \cdot p(N - N_1,M|\vec{p},\vec{n}) \tag{8.9}$$

As previously mentioned, the initial distribution for $N = 1$ is known and N_2 can be set to 1. Considering $N_2 = 1$ the last equation can be simplified to:

$$p(N = N_1 + N_2,M|\vec{p},\vec{n}) = \sum_{N_1} p(N_1,M|\vec{p},\vec{n}) \cdot p(1,M|\vec{p},\vec{n}) = p(N = N_1 + 1,M|\vec{p},\vec{n}) \tag{8.10}$$

With this knowledge any cluster size of N atoms with a total mass M can be constructed via $N-1$ convolutions of the initial $N=1$ distribution from equation 8.7.

$$p(N+1,M|\vec{p},\vec{n}) = \sum_{N} p(N,M|\vec{p},\vec{n}) \cdot p(1,M|\vec{p},\vec{n}) = p(N=N_1+1,M|\vec{p},\vec{n}) \tag{8.11}$$

The results of equation 8.11 are plotted for chromium clusters in Figure 8.1. For chromium there are 4 stable isotopes (Cr_{50}, Cr_{52}, Cr_{53} and Cr_{54}) contributing to its multinomial distribution. For small N the different cluster sizes are clearly separable (see Fig8.1 lower left), if the number of atoms in one cluster is increased. It is no longer possible to distinguish in the mass spectrum which N contributes to a given total mass M.

The form of the multinomial distribution $p(N=\text{const},M|\vec{p},\vec{n})$ for large N approximates a Gaussian distribution. This can be verified by the theorem, that any distribution will converge towards a Gaussian distribution, if it is infinitely often convoluted. With increasing N also the standard deviation σ_N increases, which causes an overlap of the distributions N and $N+1$. The standard deviation is obtained by fitting a Gaussian over the results obtained from $p(N=\text{const},M|\vec{p},\vec{n})$ as demonstrated in Figure 8.1. The obtained standard deviations σ_N can be predicted for large N ($N > 20 \Rightarrow \sigma_N < 5\%$) via the central limit theorem, which states, that after a sufficiently large amount of iterations the arithmetic mean of independent random variables will converge towards a Gaussian distribution. This is a good approximation for σ_N for large N.

$$\sigma_N = \sqrt{\text{Var}(N=1)N} \tag{8.12}$$

A measure of how separable two distributions N and $N+1$ are, can be achieved, when we demand that the two distributions have to be separated by $4\sigma_N$, so that a mass peak with a significance level of 95% can be assigned. As a result, the number of atoms in one cluster N_{crit} , where it is possible to separate the two multinomial distributions with 95% significance level is given as:

$$N_{crit,95\%} = \frac{\sigma_{crit}^2}{\text{Var}(N=1)} = \frac{\bar{m}^2}{16\text{Var}(N=1)} \tag{8.13}$$

This results (for i.e. Cr) into a $N_{crit,95\%}$ of 470 atoms, which is the point, at which σ_{crit} equals one quarter of the mean isotope mass $\bar{m}/4$. The results of a detailed study of different elements is listed in chapter 4.1.3 about the TOF mass spectroscopy.

8.2 Step-by-Step Description of a Cryoexperiment

Cryogenic deposition experiments of nanowires on TEM substrates are a rather challenging task in comparison to room temperature deposition. The goal of the experiment is to keep the grids as cold as possible and prevent contact with ambient air in order to

reduce the amount of ice crystals on the substrate's surface. Before performing a cryogenic deposition the optimal settings for the synthesis of the desired nanowires (regulated via T_{CH} and T_{EC}) have to be determined. This has to be done before the deposition experiment starts, as a temperature induced mass drift at the micro balance makes it impossible to determine any further mass depositions. In addition, the temperature stabilising lamp at the micro balance should be turned off, to decrease the amount of heat transferred to the manipulator. When all settings are fixed, a rather large amount of liquid nitrogen is required ($\approx$ 20 l, or more for longer deposition times), which should be easily accessible in order to quickly refill the manipulator and/or sample-carrying-dewar. After these initial preparations the following steps have to be performed.

1. Connecting of the reservoir (attached at the crane) to the manipulator.
2. Filling up of the container with $N_{2,liq}$. This process requires a large amount of $N_{2,liq}$ (typically 5 to 6 l), as the complete length of the manipulator has to be cooled.
3. After the cooling down of the sample holder (at least 10 min after the fill up), the deposition can be performed by swinging the sample holder into the helium beam.
4. Closing the vents between the source and main chamber. Afterwards starting the shut-down process of the main chamber can be performed. The shutdown process is done in the standard manner (see also appendix section in [55]), the forevacuum line is closed, and the TMPs' are turned off manually.
5. It is highly important that several refills of the reservoir are performed within the shutdown process to guarantee that the sample is kept at $T_{N_2,liq}$. An optimal approach is to perform refills in regular time intervals (5 or 10 min steps are ideal).
6. When the TMPs' are at half speed, it is possible to vent the chamber with dry nitrogen in order to minimise the exposure of the grids to water from ambient air.
7. During the venting process unscrewing the screws from the operating window can be started. At least 4 screws should be left in adequate positions to prevent venting the chamber with ambient air.
8. After clicking off the burst disc, which indicates that the chamber is above normal pressure, the last remaining screws should be removed quickly. This and the following steps require a lot of practice, as the longer the procedure takes, the more contaminated the sample becomes. It is highly recommended that the chamber should be flooded with dry nitrogen throughout the entire remaining procedure, as an overpressure inside the MC can help to reduce the amount of ambient air entering the chamber.
9. When the operating window is unscrewed, a plastic bag, containing a small slit for the operating tools, should be placed over the opened flange to minimise the possible entry of ambient air.

10. The sample holder can then be detached with the corresponding operation tools (an Allen wrench and a threaded rod with the appropriate length are used) and should then be quickly moved into a dewar containing $N_{2,liq}$. The closer this dewar can be placed to the chamber, the shorter the exposure time becomes.

11. The final step is then to unmount the grid(s) from the sample holder under $N_{2,liq}$ environment. This step can be challenging, as the used operation tools for unscrewing cool down, which makes the standard unmounting process harder to perform.

If all steps are done accurately, the TEM grid(s) are then ready for the observation. It is highly recommended to perform several simulations of this experiment in order to train and improve the single operating steps. Especially the unmounting process and the transfer to the dewar should be practised several times to minimise the exposure time, which is directly linked to the number of ice crystals on the substrate's surface. In addition, the exposure to air raises the substrate's temperature, so the unmounting time limits the lowest possible observation temperature.

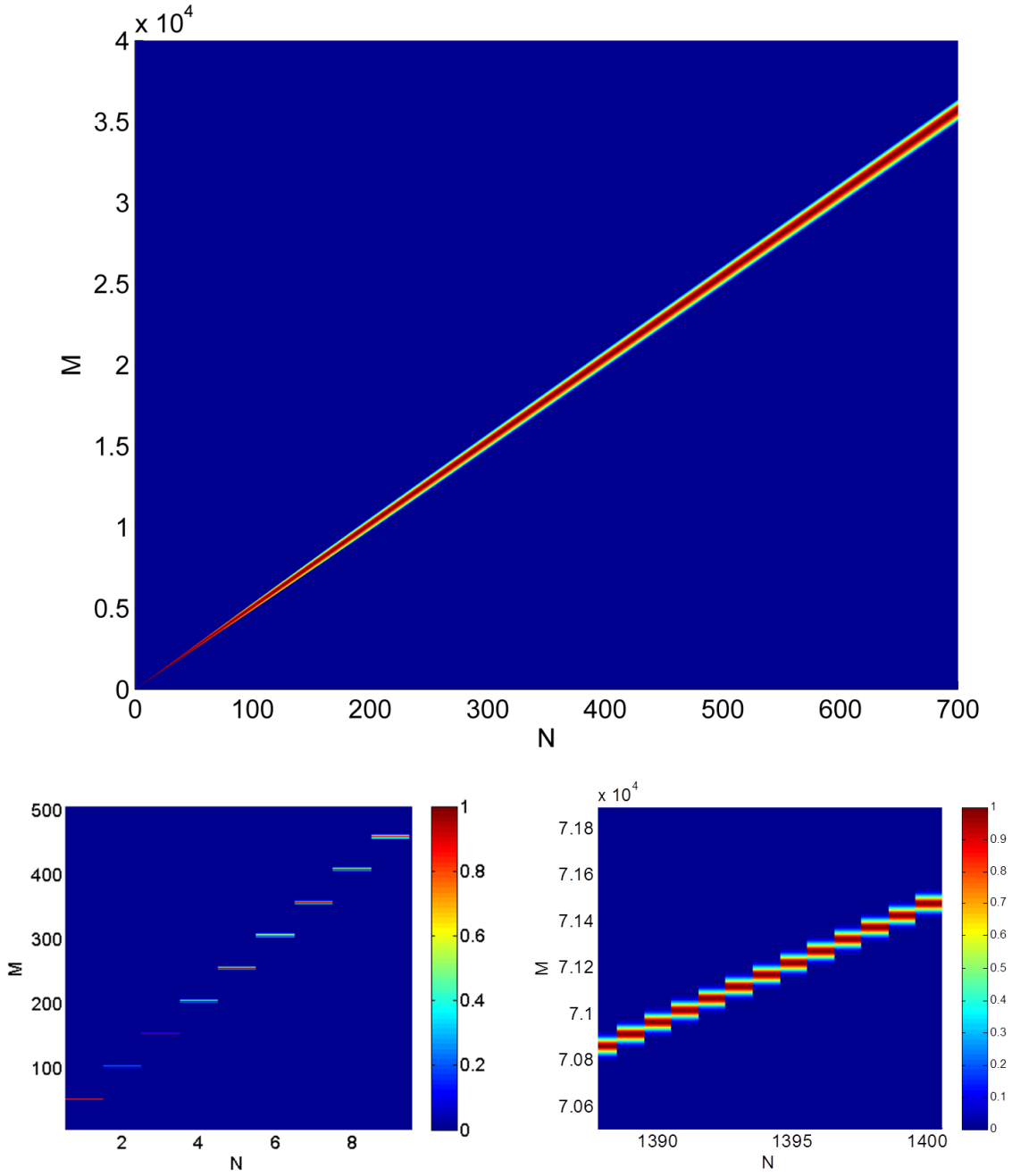

Figure 8.1: Probability $p(M,N|\vec{p},\vec{n})$ to find a cluster with k isotopes with a total mass M and a total amount of atoms N solved iteratively, when using equation 8.11. The upper graph gives an overview how increasing N leads to larger overlaps inside the mass spectrum (It can no longer be distinguished whether a mass $\tilde{M}$ is part of a cluster with $\tilde{N}$ or $\tilde{N}+1$ atoms). In the two lower images two sections of the complete plot are taken to demonstrate how an overlap evolves with increasing N.

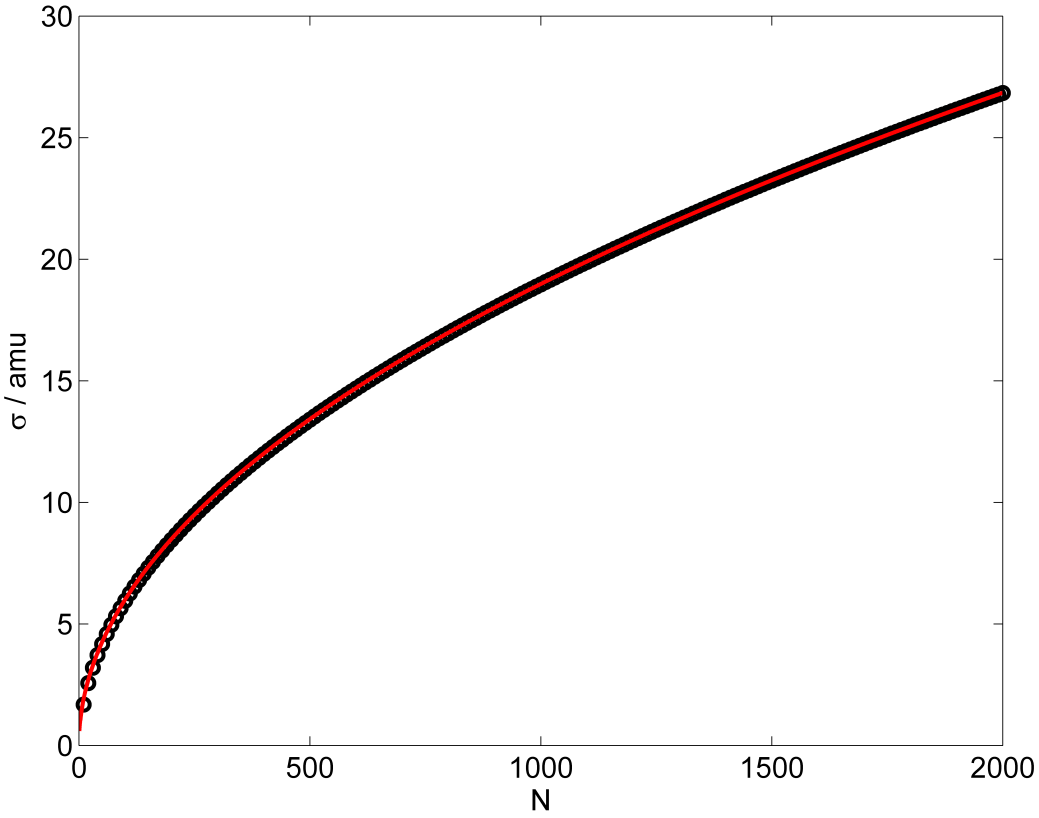

Figure 8.2: Standard deviation σ of the multinomial distribution of a Cr cluster with size N. The results are obtained when fitting a Gaussian distribution over the results obtained from $p(N+1,M|\vec{p},\vec{n})$, which are illustrated in Figure 8.1. The red line represents the prediction of the central limit theorem, which is capable of a very exact prediction for large N.

Bibliography

[1] J.-H. Ahn, S.-J. Choi, J.-W. Han, T. J. Park, S. Y. Lee, and Y.-K. Choi. Double-gate nanowire field effect transistor for a biosensor. *Nano Lett.*, 10:2934–2938, 2010.

[2] C. B. Alcock, V. P. Itkin, and M. K. Horrigan. *Canadian Metallurgical Quarterly*, 23:309, 1984.

[3] K. Yu. Arutyunov. Negative magnetoresistance of ultra-narrow superconducting nanowires in the resistive state. *Physica C*, 468:272–275, 2008.

[4] G. P. Bewley, D. P. Lathrop, and K. R. Sreenivasan. Superfluid helium: Visualization of quantized vortices. *Nature*, 441:588, 2006.

[5] C. Bréchignac, Ph. Cahuzac, F. Carlier, C. Colliex, J. Leroux, A. Masson, B. Yoon, and U. Landman. Instability driven fragmentation of nanoscale fractal islands. *Phys. Rev. Lett.*, 88:196103, 2002.

[6] C. Callegari and W. E. Ernst. Helium droplets as nanocryostats for molecular spectroscopy - from the vacuum ultraviolet to the microwave regime. In F. Merkt and M. Quack, editors, *Handbook of High Resolution Spectroscopy*. John Wiley & Sons, Chichester, 2011.

[7] J. C. Claussen, A. D. Franklin, A. ul Haque, D. M. Porterfield, and T. S. Fisher. Electrochemical biosensor of nanocube-augmented carbon nanotube networks. *ACS Nano*, 3:37–44, 2009.

[8] D. de la Iglesia et al. Nanoinformatics knowledge infrastructures: bringing efficient information management to nanomedical research. *Computational Science & Discovery*, 6, 2013.

[9] M. P. de Lara-Castells, N. F. Aguirre, H. Stoll, A. O. Mitrushchenkov, D. Mateo, and M. Pi. Communication: Unraveling the ^{4}He droplet-mediated soft-landing from *ab initio*-assisted and time-resolved density functional simulations: Au@$^4He_{300}$/TiO_2(110). *J. Chem. Phys.*, 142:131101, 2015.

[10] V. V. Dick, I. A. Solov'yov, and A. V. Solov'yov. Fragmentation pathways of nanofractal structures on surfaces. *Physical Review B*, 84(11):115408, Sept. 2011.

[11] M. Dreher, F. Pauly, J. Heurich, J. C. Cuevas, E. Scheer, and P. Nielaba. Structure and conductance histogram of atomic-sized Au contacts. *Phys. Rev. B*, 72:075435, 2005.

[12] D. M. Eisele, H. von Berlepsch, C. Böttcher, K. J. Stevenson, D. A. Vanden Bout, S. Kirstein, and J. P. Rabe. Photoinitiated growth of sub-7 nm silver nanowires within a chemically active organic nanotubular template. *J. Am. Chem. Soc.*, 132:2104–2105, 2010.

[13] H. Eyring. The activated complex in chemical reactions. *Journal of Chemical Physics*, 3, 1934.

[14] R. P. Feynman. Application of quantum mechanics to liquid helium. In C. J. Gorter, editor, *Progress in Low Temperature Physics*, pages 17–53. North-Holland, Amsterdam, 1955.

[15] M. Gardner. Mathematical Games – The fantastic combinations of John Conway's new solitaire game 'life'. *Scientific American*, 223:120–123, Oct. 1970.

[16] G. Giovannetti, P. A. Khomyakov, G. Brocks, V. M. Karpan, J. van den Brink, and P. J. Kelly. Doping Graphene with Metal Contacts. *Physical Review Letters*, 101(2):026803, July 2008.

[17] L. F. Gomez, E. Loginov, R. Sliter, and A. F. Vilesov. Sizes of large He droplets. *J. Chem. Phys.*, 135(15):154201–1–154201–9, 2011.

[18] L. F. Gomez, E. Loginov, and A. F. Vilesov. Traces of vortices in superfluid helium droplets. *Phys. Rev. Lett.*, 108(15):155302–1–155302–5, Apr. 2012.

[19] C. Gong, S. McDonnell, X. Qin, A. Azcatl, H. Dong, Y. J. Chabal, K. Cho, and R. M. Wallace. Realistic metal–graphene contact structures. *ACS Nano*, 8(1):642–649, 2014. PMID: 24261695.

[20] E. Gordon, A. Karabulin, V. Matyushenko, V. Sizov, and I. Khodos. Structure of metallic nanowires and nanoclusters formed in superfluid helium. *J. Exp. Theor. Phys.*, 112(6):1061–1070, 2011.

[21] G. Haberfehlner, P. Thaler, D. Knez, A. Volk, F. Hofer, W. E. Ernst, and G. Kothleitner. Formation of bimetallic clusters in superfluid helium nanodroplets analysed by atomic resolution electron tomography. *Nature Communications*, 6:8779, Oct. 2015.

[22] A. W. Hauser, A. Volk, P. Thaler, and W. E. Ernst. Atomic collisions in suprafluid helium-nanodroplets: timescales for metal-cluster formation derived from He-density functional theory. *Phys. Chem. Chem. Phys.*, 17(16):10805–10812, 2015.

[23] U. Henne and J. P. Toennies. Electron capture by large helium droplets. *J. Chem. Phys.*, 108(22):9327–9338, 1998.

[24] W. M. Heynes, editor. *Handbook of Chemistry and Physics*. CRC press, 2015-2016.

[25] B. H. Hong, S. C. Bae, C.-W. Lee, S. Jeong, and K. S. Kim. Ultrathin single-crystalline silver nanowire arrays formed in an ambient solution phase. *Science*, 294:348–351, 2001.

[26] https://cemas.osu.edu/fei-image-corrected-titan3tm-g2 60-300-stem. Fei website for the description of the fei image corrected titan3, 2017.

[27] http://www.denssolutions.com/products/nano chip/. Nano-chip support film range, 2017.

[28] Y. Huang, X. Duan, Y. Cui, and C. M. Lieber. Gallium nitride nanowire nanodevices. *Nano Lett.*, 2:101–104, 2002.

[29] L. Jones. Quantitative adf stem: acquisition, analysis and interpretation. *IOP Conference Series: Materials Science and Engineering*, 109(1):012008, 2016.

[30] L. Jones, K. E. MacArthur, V. T. Fauske, A. T. van Helvoort, and P. D. Nellist. Rapid estimation of catalyst nanoparticle morphology and atomic-coordination by high-resolution Z-contrast electron microscopy. *Nano Lett.*, 14(11):6336–6341, 2014.

[31] C. Kittel. *Introduction to Solid State Physics, 8 Rev ed.* John Wiley and Sons Ltd, 2004.

[32] E. L. Knuth and U. Henne. Average size and size distribution of large droplets produced in a free-jet expansion of a liquid. *J. Chem. Phys.*, 110(5):2664–2668, Feb. 1999.

[33] P. Kohli, C. C. Harrell, Z. Cao, R. Gasparac, W. Tan, and C. R. Martin. DNA-functionalized nanotube membranes with single-base mismatch selectivity. *Science*, 305:984–986, 2004.

[34] J. Lahiri and M. Batzill. Graphene destruction by metal-carbide formation: An approach for patterning of metal-supported graphene. *Applied Physics Letters*, 97(2):023102, 2010.

[35] A. Lando, N. Kébaïli, Ph. Cahuzac, A. Masson, and C. Bréchignac. Coarsening and pearling instabilities in silver nanofractal aggregates. *Phys. Rev. Lett.*, 97:133402, 2006.

[36] M. Lasserus. Metall alloying on the nanoscale. Master's thesis, TU Graz, 2017.

[37] E. Latimer, D. Spence, C. Feng, A. Boatwright, A. M. Ellis, and S. Yang. Preparation of ultrathin nanowires using superfluid helium droplets. *Nano Lett.*, 14(5):2902–2906, 2014.

[38] J. M. LeBeau, S. D. Findlay, L. J. Allen, and S. Stemmer. Standardless atom counting in scanning transmission electron microscopy. *Nano Letters*, 10(11):4405–4408, 2010. PMID: 20945926.

[39] C. M. Lieber. Nanoscale science and technology: building a big future from small things. *MRS Bulletin*, 28(07):486–491, 2003.

[40] E. Loginov, L. F. Gomez, and A. F. Vilesov. Surface deposition and imaging of large Ag clusters formed in He droplets. *J. Phys. Chem. A*, 115:7199–7204, 2011.

[41] M. Malisauskas, R. Meskys, and L. A. Morozova-Roche. Ultrathin silver nanowires produced by amyloid biotemplating. *Biotechnol. Progr.*, 24:1166–1170, 2008.

[42] R. Messner, A. Schiffman, M. Lasserus, M. Schnedlitz, and F. Lackner. Investigation of gold and silver surface plasmons on amorphous carbon and silicon nitride grids. Not published results, work in progress.

[43] V. Mozhayskiy, M. N. Slipchenko, V. K. Adamchuk, and A. F. Vilesov. Use of helium nanodroplets for assembly, transport, and surface deposition of large molecular and atomic clusters. *J. Chem. Phys.*, 127(9):094701–1–094701–6, 2007.

[44] W. W. Mullins. Theory of thermal grooving. *J. Appl. Phys.*, 28:333–339, 1957.

[45] A. H. C. Neto, F. Guinea, N. M. R. Peres, K. S. Novoselov, and A. K. Geim. The electronic properties of graphene. *Reviews of Modern Physics*, 81(1):109–162, Jan. 2009.

[46] H. B.-E. K. Northby J., J.P. Toennies and C. Winkler. Mass spectra and time of flight distributions of helium cluster beams. *Chemical Physics*, 92:6875, 1990.

[47] L. Onsager. Introductory talk. In *Proc. Int. Conf. Theor. Phys.*, pages 877–880. Science Council of Japan, Tokyo, 1953.

[48] M. Schnedlitz. Characterization of a cr evaporation cell for the generation of au-cr core-shell clusters in liquid he droplets. Master's thesis, TU Graz, 2015.

[49] B. Sciacca, J. van de Groep, A. Polman, and E. C. Garnett. Solution-grown silver nanowire ordered arrays as transparent electrodes. *Advanced Materials*, 28(5):905–909, 2016.

[50] I. A. Solov'yov, A. V. Yakubovich, P. V. Nikolaev, I. Volkovets, and A. V. Solov'yov. MesoBioNano explorer—A universal program for multiscale computer simulations of complex molecular structure and dynamics. *Journal of Computational Chemistry*, 33(30):2412–2439, Nov. 2012.

[51] J. Steurer. Helium droplet mediated fabrication and analysis of noble metal nanoparticles. Master's thesis, TU Graz, 2014.

[52] Y. Su, C. Liu, S. Brittman, J. Tang, A. Fu, N. Kornienko, Q. Kong, and P. Yang. Single-nanowire photoelectrochemistry. *Nat Nano*, 11(7):609–612, 07 2016.

[53] J. T A Witten and L. M. Sander. Diffusion-Limited Aggregation, a Kinetic Critical Phenomenon. *Physical Review Letters*, 47(19):1400–1403, Nov. 1981.

[54] Z. K. Tang, L. Zhang, N. Wang, X. X. Zhang, G. H. Wen, G. D. Li, J. N. Wang, C. T. Chan, and P. Sheng. Superconductivity in 4 angstrom single-walled carbon nanotubes. *Science*, 292:2462–2465, 2001.

[55] P. Thaler. *Buildup and Characterization of an Apparatus for the Synthesis of Metallic Nanoparticles Inside Helium Droplets.* PhD thesis, TU Graz, 2015.

[56] P. Thaler, A. Volk, F. Lackner, J. Steurer, D. Knez, W. Grogger, F. Hofer, and W. E. Ernst. Formation of bimetallic core-shell nanowires along vortices in superfluid He nanodroplets. *Phys. Rev. B*, 90:155442, 2014.

[57] P. Thaler, A. Volk, M. Ratschek, M. Koch, and W. E. Ernst. Molecular dynamics simulation of the deposition process of cold Ag-clusters under different landing conditions. *J. Chem. Phys.*, 140:044326, 2014.

[58] R. Thouy, N. Olivi-Tran, and R. Jullien. Fragmentation of two-dimensional mass fractals by surface-diffusion sintering. *Phys. Rev. B*, 56:5321–5327, 1997.

[59] J. Tiggesbäumker and F. Stienkemeier. Formation and properties of metal clusters isolated in helium droplets. *Phys. Chem. Chem. Phys.*, 9:4748–4770, 2007.

[60] J. P. Toennies and A. F. Vilesov. Superfluid helium droplets: a uniquely cold nanomatrix for molecules and molecular complexes. *Angew. Chem. Int. Ed.*, 43:2622–2648, 2004.

[61] S. Ulam and J. von Neumann. On combination of deterministic and stochastic processes. In *The Summer Meeting in New Haven*, volume 53, pages 1120+, Nov. 1947.

[62] A. Venugopal, L. Colombo, and E. M. Vogel. Contact resistance in few and multilayer graphene devices. *Applied Physics Letters*, 96(1):013512, 2010.

[63] M. V.M. Is quartz crystal microbalance really a mass sensor. *ScienceDirect*, 2004.

[64] A. Volk. *Nanocluster and Nanowire Growth in Superfluid Helium Nanodroplets.* PhD thesis, TU-Graz, 2016.

[65] A. Volk, D. Knez, P. Thaler, A. W. Hauser, W. Grogger, F. Hofer, and W. E. Ernst. Thermal instabilities and Rayleigh breakup of ultrathin silver nanowires grown in helium nanodroplets. *Physical Chemistry Chemical Physics*, 17(38):24570–24575, Sept. 2015.

[66] A. Volk, P. Thaler, D. Knez, A. W. Hauser, J. Steurer, W. Grogger, F. Hofer, and W. E. Ernst. Correction: The impact of doping rates on the morphologies of silver and gold nanowires grown in helium nanodroplets. *Phys. Chem. Chem. Phys.*, 18:1451–1459 and 3359, 2016.

[67] A. Volk, P. Thaler, M. Koch, E. Fisslthaler, W. Grogger, and W. E. Ernst. High resolution electron microscopy of Ag-clusters in crystalline and non-crystalline morphologies grown inside superfluid helium nanodroplets. *J. Chem. Phys.*, 138:214312, 2013.

[68] J. von Neumann. The general and logical theory of automata. In L. A. Jeffress, editor, *Cerebral mechanisms in behavior; the Hixon Symposium*. Wiley, Oxford, England, 1951.

[69] Q. Wang, F. Min, and J. Zhu. Preparation of gold nanowires and its application in glucose biosensing. *Mater. Lett.*, 91:9–11, 2013.

[70] G. A. Williams and R. E. Packard. Photographs of quantized vortex lines in rotating He II. *Phys. Rev. Lett.*, 33:280–283, 1974.

[71] S. Wolfram. Statistical mechanics of cellular automata. *Rev. Mod. Phys.*, 55:601–644, Jul 1983.

[72] E. J. Yarmchuk, M. J. V. Gordon, and R. E. Packard. Observation of stationary vortex arrays in rotating superfluid helium. *Phys. Rev. Lett.*, 43:214–217, 1979.

[73] Y. Yin, Y. Sun, M. Yu, X. Liu, T. Jiang, B. Yang, D. Liu, S. Liu, and W. Cao. ZnO nanorod array grown on Ag layer: A highly efficient fluorescence enhancement platform. *Sci. Rep.*, 5:8152, 2015.

[74] G. Zhu, S. Zhang, Z. Xu, J. Ma, and X. Shen. Ultrathin ZnS single crystal nanowires: Controlled synthesis and room-temperature ferromagnetism properties. *J. Am. Chem. Soc.*, 133:15605–15612, 2011.

Danksagung

An dieser Stelle möchte ich die Gelegenheit nutzen um mich in erster Linie bei meinem Betreuer, Professor Wolfgang E. Ernst zu bedanken, der es mir im Zuge des letzten Jahres ermöglicht hat, die ersten Schritte im physikalischen Forschungsbetrieb zu setzen. Ihm gilt nicht nur der Dank für seine Betreuung, sondern auch für die Ermöglichung der Mitarbeit in einem kompetitiven aber nichts desto trotz sehr liebenswürdigen Forschungsteam. Bei dem genannten Team möchte ich mich insbesondere sehr herzlich bedanken.

Angefangen bei meinen Vorgängern, Alexander Volk und Philip Thaler, welche besonders während des ersten halben Jahres sich immer Zeit nahmen, um mir mit Rat und Tat beiseite zu stehen.

Des Weiteren gilt es dem engeren Team im Clusterlabor, alias den Helenisten, Florian Lackner, Roman Messner, Alexander Schiffmann und meinem Mitstreiter und langjährigen Freund Maximilian I. Lasserus zu danken. Mit Aufopferungsbereitschaft, Humor und der ein oder anderen guten Idee ist es schlussendlich doch immer gelungen, anstehende Probleme zu lösen.

Insbesondere gilt es auch, den anderen Kollegen zu danken: allen voran Andreas Hauser, welcher nicht ganz unschuldig war, welchen Verlauf diese Arbeit genommen hat und der, als Büronachbar immer für einen Scherz zu haben war. Ein großer Dank geht auch an Daniel Knez, welcher der Hauptleidtragende war, wenn wir wieder eine Messung am Titan durchführen wollten. Ihm und der unendlichen Weisheit von Dr. Axel Stoll ist es zu verdanken, dass eine derart große Studie an TEM Untersuchungen möglich war.

Den restlichen Kollegen, wie den Femtoguys oder den Helium Streuern möchte ich auch ein herzliches Dankeschön für ihre tolle Zusammenarbeit und das tolle Arbeitsklima während dieses Jahres aussprechen.

Nicht zu vergessen sind noch meine Studienkollegen und guten Freunde, Krissi, Kathi (danke für das Kochen an Sonntagen), Roman, Pascal, Max, Philip und Andi welche mir diese Studienzeit erst so richtig verschönt haben. Auch und gerade weil ich vermutlich meine Eigenheiten habe und sie mich nichtsdestotrotz schätzen, möchte ich mich hier bei ihnen sehr herzlich bedanken.

Und am Schluss wären da noch meine Eltern, welche mich immer unterstützt haben und ohne die ich es, mit an Sicherheit grenzender Wahrscheinlichkeit, nie soweit geschafft hätte.